

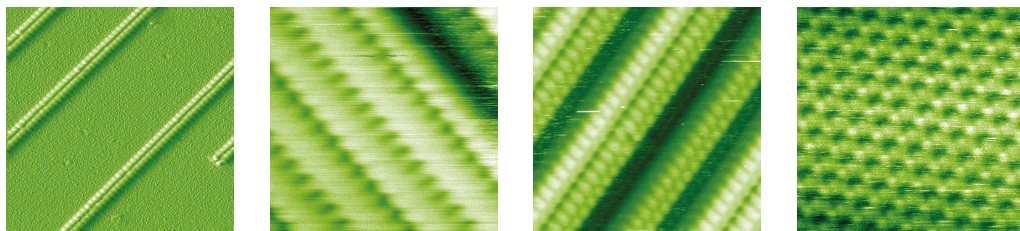
The Influence of Functional Groups on the Molecular Self-Assembly on Calcite

Dissertation
zur Erlangung des Grades
„Doktor der Naturwissenschaften“
im Promotionsfach Physikalische Chemie

am Fachbereich Chemie, Pharmazie und Geowissenschaften
der Johannes Gutenberg-Universität Mainz

Julia Luise Neff

geboren in Heidelberg



Mainz, den 30. Juli 2014

This dissertation was supervised by [Personal data removed] and was carried out at the Johannes Gutenberg-Universität Mainz from April 2012 to July 2014.

D77 (Dissertation Johannes Gutenberg-Universität Mainz)

Dean of the faculty [Personal data removed]

1st report [Personal data removed]

Johannes Gutenberg-Universität Mainz

2nd report [Personal data removed]

Max Planck Institute for Polymer Research Mainz

Submitted: 31. July 2014

Oral examination: 15. September 2014

Contents

1	Introduction	1
2	Methods	5
2.1	Introduction	6
2.2	Non-Contact Atomic Force Microscopy	7
2.3	Kelvin Probe Force Microscopy	14
2.4	Experimental Setup	28
3	Molecular Self-Assembly on Insulators	33
3.1	Basic Principles	34
3.2	Bulk Growth and Dewetting	35
3.3	Anchoring Strategies	37
3.4	Tuning the Self-Assembly	43
4	Calcite and Benzoic Acids	45
4.1	The Insulating Substrate: Calcite	46
4.2	The Molecular Building Block: Dihydroxybenzoic Acid	50
5	Decisive Influence of Substitution Positions	53
5.1	Introduction	54
5.2	Results	56
5.3	Discussion	61
5.4	Conclusions	64
6	Long-Range Influence of a Hydroxyl Group	67
6.1	Introduction	68
6.2	Observation: Stripe-like Assembly	71
6.3	Discussion	86
6.4	Conclusions	94
7	Influence of Different Hydrogen Bond Donors	95
7.1	Introduction	96
7.2	Amino vs. Hydroxyl Groups	98

7.3	Amide vs. Carboxyl Groups	103
7.4	Conclusions	118
8	Long-Range KPFM Contrast on Monopole and Dipole Assemblies	119
8.1	Introduction	120
8.2	Experimental Details	122
8.3	Slices: Lateral and Vertical Signal Extension	126
8.4	Long-Range Curves: Shape of the Distance Dependence	134
8.5	Conclusions	145
9	Summary	147
	Bibliography	151
A	Overview of Self-Assembled Structures	171
B	Trends of KPFM contrasts	177
	Acknowledgements	179
	Publications and Presentations	181

1 Introduction

The spontaneous formation of ordered structures is omnipresent in nature [1]. From weather patterns to atomic crystals, building blocks arrange into ordered patterns. Highly functional arrangements composed of molecular building blocks are found in biological systems. For instance, lipid molecules assemble into polar bilayers, which act as cell membranes and nucleic acids assemble into DNA, which stores large amounts of information. Interestingly, these ordered, functional arrangements in biology are governed by reversible interactions between molecules rather than external stimuli [2].

The potential of weak intermolecular interactions to create functional ensembles has been widely recognized in supramolecular chemistry in solution [3]. Donald J. Cram, Jean-Marie Lehn and Charles J. Pedersen have been rewarded with the Nobel prize 'for their development and use of molecules with structure-specific interactions of high selectivity' in 1987. In his Nobel prize speech, Jean-Marie Lehn envisioned deliberately designed molecules to assemble into supermolecules and molecular devices, which act as sensors by processing information on the molecular scale [4].

On surfaces, molecular self-assembly presents an appealing strategy for technical applications as it allows to create functional structures composed of nanoscale building blocks without the need to produce them with nanoscale devices. Possible applications are manifold, as surfaces play an important role as chemically active layer, as template or as support for (opto)electronic devices. On metal surfaces, molecular self-assembly has been

studied extensively, so that now a large variety of surface structures is available ranging from one-dimensional wire-like assemblies over two-dimensional islands of different geometry to porous networks [5].

Since many technical relevant substrates are not metallic, understanding the self-assembly on insulating substrates opens new perspectives. Even more, molecular electronic devices require an insulating support to function, as they need to be electronically decoupled from their support. However, versatile structure formation on insulating substrates is hampered by the generally weak molecule-substrate interaction. Only recently, several strategies have been established how to anchor molecules to insulators by specifically enhancing the molecule-substrate interaction [6]. In this context, the natural cleavage plane of calcite has been found to constitute a suitable insulating substrate on which carboxylic acids form substrate-templated patterns at room temperature [7]. Hydrogen-bonded networks can develop with the surface oxygens as hydrogen bond acceptors and the carboxylic acids as hydrogen bond donors. Furthermore, carboxylic acids provide reliable intermolecular interaction due to their combined donor and acceptor character [8].

In this thesis, I put the focus on the influence of the functional groups on hydrogen-bonded networks on calcite. With dihydroxybenzoic acid as starting molecule, I systematically study the influence of small variations at the molecule on the assembly.

To start, I investigate the influence of the positions of the substituted functional groups on the structure formation in Chap. 5. Afterward, I consider the influence of the number of identical functional groups in Chap. 6. The influence of the hydrogen bonding characteristics on the assembly is studied in Chap. 7 by stepwise substituting hydroxyl groups by amino groups. Finally, Chap. 8 discusses the difference in the electrostatic forces present above molecular islands of different charge state and above the substrate.

The results of this thesis, reveal the manifold influences of slight adjustments at the molecular building block on the structure formation on an insulating substrate. A comparatively simple

molecule-substrate system is presented, which, nevertheless, allows to tune the molecular self-assembly from mobile or metastable arrangements over stable two-dimensional patterns to wire-like structures with and without mesoscopic order.

2 Methods

Contents

2.1 Introduction	6
2.2 Non-Contact Atomic Force Microscopy .	7
Relevant Interactions	7
Frequency Modulation AFM	10
Contrast Formation	12
2.3 Kelvin Probe Force Microscopy	14
Macroscopic Work Function Measurements .	14
Principle of KPFM	16
Contrast Formation	20
2.4 Experimental Setup	28
UHV Chamber	28
Sample Preparation	29
Data Analysis	32

Scanning probe microscopy allows to probe surface properties in real space with a sensitivity to single molecules and atoms, *i.e.*, it is the ideal tool to study the molecular self-assembly on a surface.

This chapter gives a brief introduction into non-contact atomic force microscopy (nc-AFM) and Kelvin Probe Force Microscopy (KPFM), the methods used within this thesis. The contrast mechanism, the principle of the frequency modulation method and the experimental setup are addressed, including an assessment of the benefits and drawbacks.

2.1 Introduction

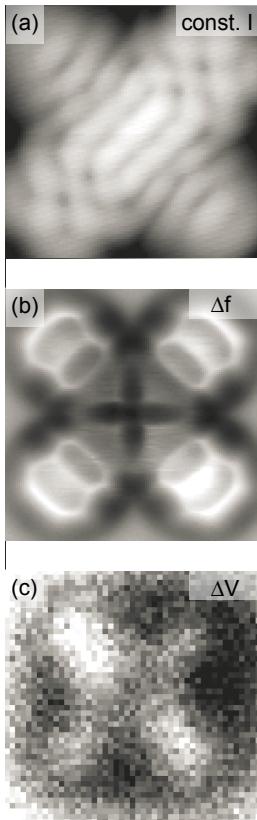


Figure 2.2: A single naphthalocyanine molecule on a bilayer of NaCl on Cu(111), measured using a CO-terminated tip at 5 K with (a) constant-current STM, (b) AFM and (c) KPFM. Adapted from [13].

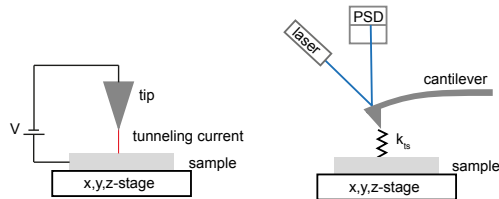


Figure 2.1: Principle of STM and AFM.

Scanning probe microscopy [9] allows to ‘see’ at the atomic scale in real space. A probe tip is scanned over a sample surface at a distance below one nanometer, while a strongly distance-dependent property is recorded (Fig. 2.1). In a scanning tunneling microscope (STM) [10] the tunneling current reveals information about the electronic structure at the Fermi level. In an atomic force microscope (AFM) [11], the intermolecular forces acting between the probe and the sample are recorded. The resulting signal represents the topography and can visualize single bonds. In Kelvin probe force microscopy (KPFM) [12] electrostatic forces are measured and information about the charge distribution is gained.

An example for the complementary information gained by different scanning probe techniques is shown in Fig. 2.2 for a naphthalocyanine molecule imaged with a CO-terminated tip, showing (a) its electronic structure at the lowest unoccupied molecular orbital, (b) the chemical bonds and (c) the charge distribution.

On insulating substrates, as used in this thesis, AFM and KPFM are applicable. In the first part of this chapter, I briefly describe non-contact AFM (nc-AFM) (more details, *e.g.*, in [14]), including essential tip-sample interactions, the frequency modulation technique and relevant imaging artifacts. The second part discusses the measurement principle of KPFM and its contrast mechanism for different modifications of a plate capacitor. In the last part of the chapter, I present the experimental setup.

2.2 Non-Contact Atomic Force Microscopy

The surfaces of bodies are the field of very powerful forces of whose action we know but little.
Lord Raleigh

Relevant Interactions

Different forces contribute to the interaction between a tip and a sample, which are separated by only a few nanometer [15, 16]. These forces act over a wide range, show different magnitudes and can be attractive or repulsive.

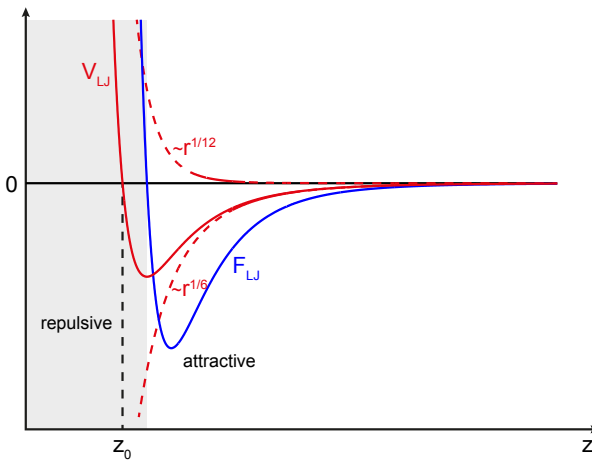


Figure 2.3: Lennard-Jones potential V_{LJ} and corresponding force F_{LJ} composed of repulsive short range interaction proportional to $z^{1/12}$ and attractive long-range interaction proportional to $z^{1/6}$, which model Pauli repulsion and van-der-Waals interaction of two atoms.

The empirical Lennard-Jones potential V_{LJ} [17] describes the interaction of two atoms as a function of their distance z by a superposition of repulsive short-range interactions and attractive long-range interactions, with the empirical parameters ϵ and σ :

$$V_{LJ}(z) = 4\epsilon \left(\left(\frac{\sigma}{z} \right)^{12} - \left(\frac{\sigma}{z} \right)^6 \right) \quad (2.1)$$

The corresponding force looks like:

$$F_{LJ}(z) = 4\epsilon \left(12 \frac{\sigma^{12}}{z^{13}} - 6 \frac{\sigma^6}{z^7} \right) \quad (2.2)$$

Repulsive, short range forces are described by a term proportional $z^{1/13}$, modeling the Pauli repulsion. This repulsion occurs, as due to the Pauli exclusion principle no two identical fermions can occupy the same quantum state. Likewise, attractive short range forces exist, if overlapping orbitals allow for covalent binding. Both have a decay length of below 1 nm [15] and are in most cases responsible for atomic resolution in AFM [14]. However, high resolution is hampered by long-range forces, which average over a large surface area. In the Lennard-Jones potential, attractive long-range forces are modeled by a term proportional $z^{1/7}$, which is the typical behavior of the van-der-Waals force between two atoms. The decay behavior of long-range forces is more complex for a tip-sample geometry, as discussed in the following.

Van-der-Waals Forces

Van-der-Waals forces combine three types of interactions with the same distance dependence: dipole-dipole interactions (Keesom interaction [18]), interactions between a dipole and an induced dipole (Debye interaction [19]) and interactions between two induced dipoles (London dispersion interaction [20]). The first two are easily understood from classical electrostatics. London forces are explained by quantum fluctuations and occur even between nonpolar atoms and, thus, are always present. For two atoms, the van-der-Waals potential follows an inverse power law $\propto z^{1/6}$ like in the Lennard-Jones potential.

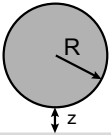


Figure 2.4: Sphere in front of flat surface with $R \gg z$.

In an AFM setup, not only two atoms are interacting but a macroscopic tip interacts with a surface. Assuming the interaction being nonretarded and additive, the van-der-Waals force between two macroscopic objects can be estimated by integration over the volumes V_i using the materials densities ρ_i and the coefficient c for the atom-atom pair-potential [21]:

$$F_{vdW} = \rho_1 \rho_2 \int_{V_1} \int_{V_2} -\nabla \left(-\frac{c}{z^6} \right) \frac{1}{\pi^2} dV_2 dV_1 \quad (2.3)$$

In the case of a spherical tip of radius R at a distance z from a flat surface this reduces to [15]:

$$F_{vdW} = -\frac{HR}{6z^2}, \quad (2.4)$$

with the Hamaker constant $H = \pi^2 c \rho_1 \rho_2$. Thus, for macroscopic objects, the distance dependence is drastically altered. The slow decay of the force implies that a large part of tip and sample interact resulting in an interaction which is not site-specific. Consequently, van-der-Waals forces mostly lead to a constant offset to the AFM measurements, while only in rare cases atomic resolution is achieved solely by van-der-Waals forces [22, 23]. With a typical value of $1 \cdot 10^{-19} \text{ J}$ of the Hamaker constant (silicon nitrate: $1.7 \cdot 10^{-19} \text{ J}$, CaF_2 : $0.7 \cdot 10^{-19} \text{ J}$ [15]) and a tip radius of 50 nm, the strength of the van-der-Waals forces at a distance z of 0.5 nm amounts to about 3 nN. On calcite (10.4), van-der-Waals contributions of 0.4 nN are measured at the force minimum, while the site-specific short range forces only amount to 0.1 nN [24].

Electrostatic Forces

The Coulomb interaction for two point charges is:

$$F_C(z) = \frac{1}{4\pi\epsilon_0} \frac{q_1 \cdot q_2}{z^2} \quad (2.5)$$

Accordingly, a force of about 6 nN acts on two elementary charges with a distance of 0.5 nm. In an ionic crystal the electrostatic interactions sum up to zero far away but can lead to atomically resolved AFM images in the vicinity of the surface [25, 26]. For a spherical tip at a truncated cone in front of a sample (both conducting, $z \ll R$) the electrostatic force is approximately given by [27]:

$$F_{el}(z) = -\pi\epsilon_0 \left(\frac{R^2}{z(z+R)} \right) V^2 \quad (2.6)$$

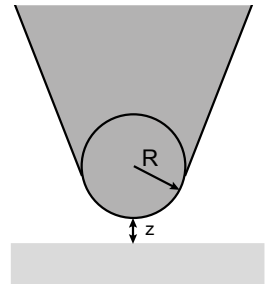


Figure 2.5: Sphere at truncated cone in front of flat surface with $R \gg z$.

Using the same parameters as in the example of van-der-Waals interactions ($z = 0.5$ nm, $R = 50$ nm) and assuming an electrostatic potential difference of $V = 1$ V, results in $F_{el} \approx 3$ nN, comparable to the van-der-Waals contribution.

The electrostatic forces can be compensated by applying a voltage between tip and sample. Furthermore, KPFM provides a possibility to separate the force contributions, as discussed in section 2.3.

Frequency Modulation AFM

Forces like the gravitational force can be measured by the extension of a spring according to Hooke's law:

$$F = -kz \quad (2.7)$$

Forces between a microscopic tip and a sample can similarly be characterized by a spring constant k_{ts} . A freely and harmonically oscillating cantilever has an eigenfrequency f_0 of

$$f_0 = \frac{1}{2\pi} \sqrt{\frac{k_0}{m^*}}, \quad (2.8)$$

with k_0 being the spring constant of the cantilever and m^* the effective mass. If the cantilever feels an interaction with the surface, the spring constant changes ($k = k_0 + k_{ts}$) and the eigenfrequency shifts. Atomic resolution on a large variety of surfaces in UHV is achieved using the frequency modulation AFM mode [28], referred to as FM-AFM. In the FM mode, the cantilever is always driven at its current eigenfrequency and additionally the amplitude is kept constant. The shift of the eigenfrequency (detuning, Δf) is employed as imaging signal. For small amplitudes ($\ll 3$ Å), the image of a weakly perturbed harmonic oscillator holds, and

$$\Delta f \propto \frac{\partial F}{\partial z} \quad (2.9)$$

In general, the frequency shift is related to the force by a weighted average [16, 29]:

$$\Delta f(z) = -\frac{f_0}{\pi k A^2} \int_{-A}^A F_{ts}(z - q') \frac{q'}{\sqrt{A^2 - q'^2}} dq', \quad (2.10)$$

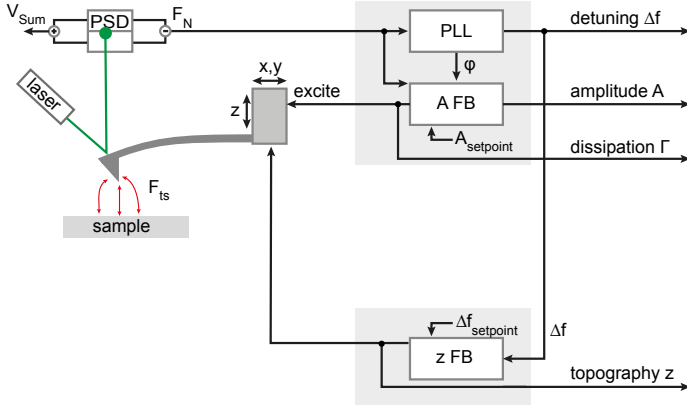


Figure 2.6: FM-AFM setup used within this thesis. The left side shows sample and cantilever with excitation piezo, light source and photosensitive detector (PSD). On the right side, the electronics are depicted with phase-locked loop (PLL), amplitude feedback (A FB) and distance feedback (Z FB).

where $q'(t) = A \cos(2\pi f_0 t)$ is the unperturbed motion of the cantilever with the eigenfrequency f_0 and z the lower turning point of the cantilever.

The principle of an FM-AFM set-up is drawn in Fig. 2.6. On the left side, the tip-sample system and the detection equipment are depicted. The movement of the cantilever is detected by a position sensitive photo diode (PSD).¹ The difference signal between upper and lower half yields the deflection signal caused by the cantilever motion along the surface normal, often referred to as F_N . On the right side of Fig. 2.6, the three feedback loops of FM-AFM are shown. F_N is fed into the phase-locked loop (PLL) and the amplitude feedback loop. The PLL determines the absolute phase of the oscillation and thereby the current frequency f , which is used to excite the cantilever. By comparing f to the eigenfrequency of the freely oscillating cantilever f_0 , the primary imaging signal is generated according to $\Delta f = f - f_0$. Additionally, the amplitude feedback compares the amplitude of F_N with the amplitude setpoint $A_{setpoint}$ and generates the amplitude of the excitation signal accordingly. This voltage required to keep the oscillation corresponds to the dissipated energy and is referred to as dissipation (Γ). If the measurement is carried out at the eigenfrequency, the frequency shift is caused by con-

¹For simplicity only two segments are drawn. In the experiments a four quadrant photo diode was used, which works according to the same principle. Further detection principles like self-sensing sensors or interferometry etc. can also be used.

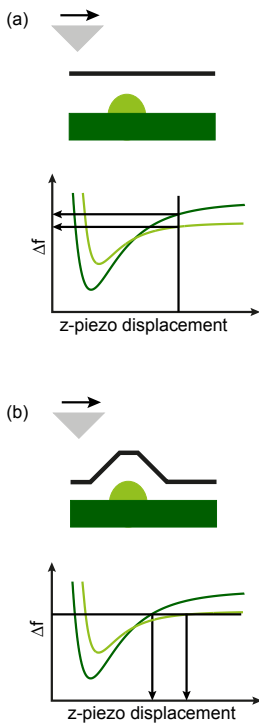


Figure 2.7: Different feedback modes. (a) In constant height mode, the tip is scanned over the surface at a constant z -position. The measurement signal reflects the different Δf values of $\Delta f(z)$. (b) In constant Δf mode, the feedback keeps Δf constant by adjusting the z -position. The resulting data does not necessarily reflect the real topography of the sample.

servative forces, while the dissipation is due to non-conservative forces, *i.e.*, conservative and dissipative forces are detected separately. For measurements in constant Δf mode (see below), a distance feedback is used, which controls the z -position by keeping Δf constant at the setpoint $\Delta f_{setpoint}$.

Contrast Formation

The measurements can be conducted in constant height or in constant Δf mode. In the constant height mode (Fig. 2.7 (a)), the tip is scanned over the surface at a constant height, while the interaction is recorded. This mode allows for directly recording the frequency shift without artifacts that can occur from the distance feedback loop. However, at steep substrate features or due to z -drift, tip crashes can occur easily. For long-lasting (spectroscopy) measurements it can be useful to compensate for the z -drift by using an atomic tracking system [30].

Most measurements in this thesis were recorded using the z -feedback either in quasi-constant height, in which the feedback is only used as tilt correction, or in constant Δf mode (Fig. 2.7 (b)). Care has to be taken as z -data resulting from constant Δf measurements do not necessarily reflect the real topography of the sample. Only for steps edges between different terraces of the same material, the $\Delta f(z)$ curves are equal, so that the real topography is measured. In all other cases, the measured height depends on the Δf setpoint and is, consequently, referred to as apparent height. If $\Delta f(z)$ curves cross, contrast inversion occurs as is frequently observed in AFM [31, 32].

Any AFM image is a convolution of tip and sample. Consequently, surface features are broadened and reflect the shape of the tip (Fig. 2.8 (a) and (b)). In the case of a tip with a side feature, all substrate features appear with a side feature at the opposite side of the tip feature independent of the scan direction. Artifacts can also occur due to a slow feedback loop. These features, however, depend on the scan direction, *i.e.*, a shade always occurs after the feature (Fig. 2.8). An analysis of different imaging channels and directions helps to identify scan artifacts.

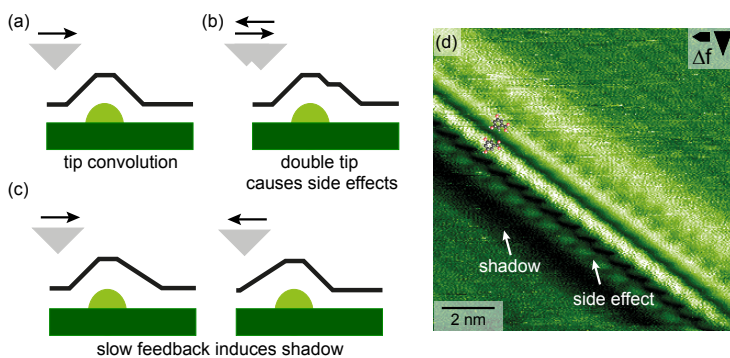
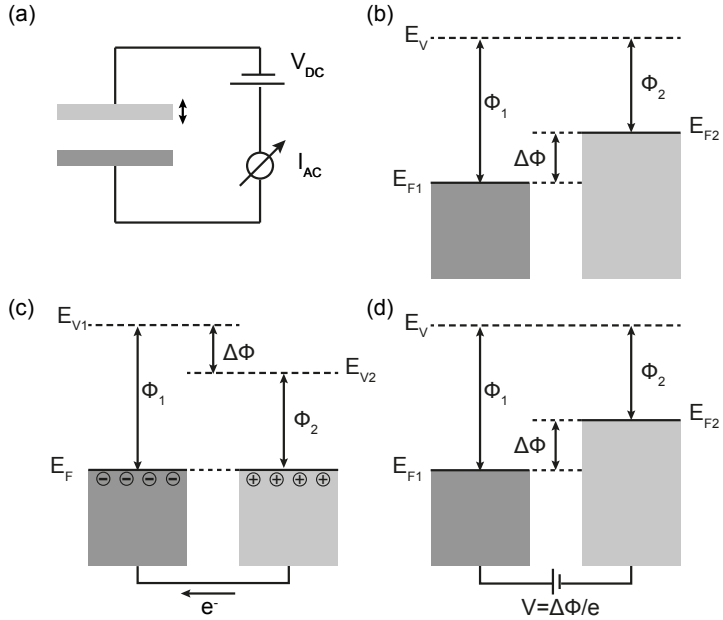


Figure 2.8: Scan artifacts due to (a) and (b) tip shape and (c) feedback. (d) Frequency shift image of a molecular double row on calcite (10.4) showing both, tip features and feedback artifacts.

In summary, nc-AFM allows to image individual species on any kind of (flat) substrate. By the acquired images, information about periodicity, distributions, positions and distances is gained. For instance, it is possible to count individual molecules. However, nc-AFM does typically not allow for conclusions about the chemical identity, the height or the lateral dimension of the observed structure.

Figure 2.9: Kelvin method. Principle (a) and shift of the energy levels of two metals with different work function without contact (b), in contact (c) and with external voltage V (d).



2.3 Kelvin Probe Force Microscopy

Macroscopic Work Function Measurements

The work function Φ of a material, or rather a surface, is the minimum energy required to remove an electron from the interior of the solid to the vacuum nearby [33]. For metals, Φ ranges from about 2 eV to 5 eV.

Kelvin Method

Already in 1898, Lord Kelvin developed a method to measure the work function difference between two metals [34] and realized that the result does not only depend on the work function of the metal itself but also on its chemical history, for example on surface oxidation. Two metals with work functions Φ_1 and Φ_2

are brought in parallel position to form a plate capacitor (Fig. 2.9 (a)). Due to their difference in work function $\Delta\Phi = \Phi_1 - \Phi_2$, their Fermi levels E_{Fi} are not aligned, while they share a common vacuum level E_V (Fig. 2.9 (b)). When the metals are connected, the Fermi levels align and a current flows until the voltage difference is compensated (Fig. 2.9 (c)). If the distance d between the metals is changed, the capacity $C = Q/V$ changes according to $C = \epsilon_0 \cdot A/d$, with the permittivity ϵ_0 and the surface of the plates A . Accordingly, the charge in the capacitor is modulated when d is modulated, resulting in an AC current $I_{AC} = dQ/dt$. The current can be nullified when applying a DC voltage V_{DC} , which compensates for the difference in the work functions (Fig. 2.9 (d)), *i.e.*, $V_{DC} = \frac{\Phi_1 - \Phi_2}{e}$. Due to the contact between the metals this voltage is often referred to as contact potential difference V_{CPD} .

Spectroscopic Methods

Not only the work function, but additional electronic properties of conducting surfaces can be retrieved by means of spectroscopy [35]. Photoelectron spectroscopy probes the occupied states of a sample and can determine work functions quantitatively. Additionally, organic/metal interface properties are probed such as the vacuum level shifts relative to the substrate Fermi level (dipole formation) or the ionization potential. Inverse photoelectron spectroscopy can determine unoccupied states and is used to measure electron affinities or the lowest unoccupied molecular orbital. For materials with low conductivity effects like charging of the surface occur due to the impinging electrons and radiation damage is possible.

All of these methods average over a certain surface area. To understand the local electronic surface structure, scanning probe methods are applied. While STM measures the local electronic states at the Fermi level on conducting samples, KPFM [12, 36] gives insight into the charge distribution on any kind of sample.

Principle of KPFM

Between metal tip and metal sample an electrostatic force acts (derivation in the next paragraph):

$$F_{el}(z) = -\frac{1}{2} \frac{\partial C(z)}{\partial z} (V_{DC} - V_{CPD})^2 \quad (2.11)$$

The most simple way to gain information about the local work function is sweeping the voltage while detecting Δf . As $\Delta f \propto \partial F / \partial z$ (at least for small amplitudes), a parabolic behavior is expected for a metal tip and a metal sample with the vertex of the parabola showing V_{CPD} . If the electrostatic forces are the same on the whole surface, they can easily be compensated by applying V_{CPD} . If different surface regions show different electrostatic forces, the parabolas are shifted for the different regions. By recording a $\Delta f(V)$ curve in each pixel and plotting V_{CPD} , Mohn *et al.* [13] mapped the charge distribution within a single molecule.

A faster way to acquire a surface map of V_{CPD} is KPFM, which can be done parallel to the AFM imaging. Based on the macroscopic Kelvin method, Nonnenmacher *et al.* [12] implemented the method into the AFM setup. A modulation voltage $V_{AC}(t) = V_{mod} \cos(2\pi f_{mod} t)$ is applied to the tip, so that the force changes according to:

$$F_{el}(z) = -\frac{1}{2} \frac{\partial C(z)}{\partial z} (V_{DC} - V_{CPD} + V_{AC})^2 \quad (2.12)$$

Expansion of the product with $V_{CPD} = \Delta\Phi/e$ results in three spectral components $F_{el}(z) = F_{DC}(z) + F_{f_{mod}}(z) + F_{2f_{mod}}(z)$:

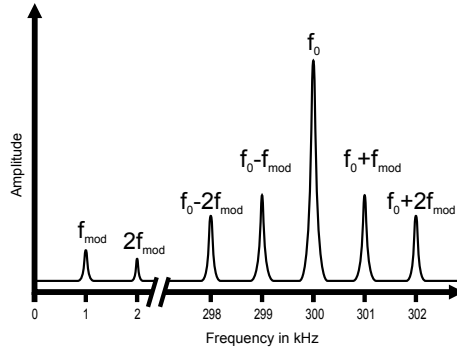
$$F_{el}(z) = -\frac{1}{2} \frac{\partial C}{\partial z} \left((V_{DC} - \Delta\Phi/e)^2 + \frac{1}{2} V_{mod}^2 \right) \quad (2.13)$$

$$-\frac{\partial C}{\partial z} (V_{DC} - \Delta\Phi/e) V_{mod} \cos(2\pi f_{mod} t) \quad (2.14)$$

$$-\frac{1}{4} \frac{\partial C}{\partial z} V_{mod}^2 \cos(2\pi 2f_{mod} t) \quad (2.15)$$

Due to the modulation voltage, the static part of F_{el} (Eq. 2.13) has the additional component $1/4 \partial C / \partial z V_{mod}^2$, which causes a shift

Figure 2.10: Response of the cantilever to a modulation voltage $V_{mod} \cos(2\pi f_{mod} t)$. The amplitudes are not drawn to scale. Adapted from [37].



of the cantilever's equilibrium position. Using a lock-in amplifier, the frequency dependent components can be separated. The component $F_{f_{mod}}$ (Eq. 2.14) vanishes for $V_{DC} = V_{CPD}$ and is used to measure V_{CPD} . Obviously, this condition also minimizes the total force F_{el} . The third component $F_{2f_{mod}}$ (Eq. 2.15) can be exploited to gain information about the capacity as the capacity gradient is the only unknown in this expression.

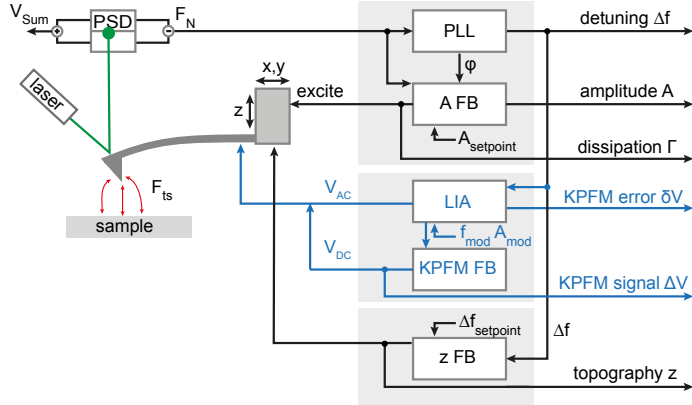
Frequency Modulation KPFM

The response of the cantilever due to the modulation voltage is sketched in Fig. 2.10 for a modulation frequency $f_{mod} = 1$ kHz. Peaks are visible at the fundamental eigenfrequency of the cantilever f_0 , at the modulation frequency f_{mod} and at $2 \cdot f_{mod}$. Additional peaks occur at $f_0 \pm f_{mod}$ and at $f_0 \pm 2 \cdot f_{mod}$ due to a frequency modulation of the fundamental resonance. In frequency-modulation KPFM (FM-KPFM) [38] this modulation of Δf is detected.²

A principle circuit diagram is shown in Fig. 2.11. The additional feedback compared to the AFM setup in Fig. 2.6 is highlighted in blue. A lock-in amplifier (LIA) applies an AC voltage V_{AC} to the cantilever. The Δf output of the PLL is fed into the lock-in amplifier, which determines phase and amplitude of $\Delta f_{f_{mod}}$. The amplitude is then used by an additional feedback loop (KPFM

²Using an additional lock-in amplifier the modulation with $2f_{mod}$ can be detected, if $2f_{mod}$ also lies within the bandwidth of the PLL.

Figure 2.11: FM-KPFM setup used within this thesis. The additional components compared to the FM-AFM setup in Fig. 2.6 are depicted in blue. The demodulated Δf signal is fed into a lock-in amplifier (LIA), which also provides the modulation voltage V_{AC} . An additional feedback loop (KPFM FB) is used to minimize Δf_{mod} by applying the appropriate V_{DC} .



FB) to minimize $F_{f_{mod}}$ by applying the appropriate V_{DC} to the tip.

For such a measurement the modulation frequency has to be chosen appropriately. The lower limit is determined by increasing cross talk with the topography signal, while the upper limit is given by the bandwidth of the PLL. According to Glatzel *et al.* [39], frequencies lower than 1 kHz influence the topography signal. As the applied PLL has a maximum bandwidth of 1.3 kHz, modulation frequencies around 1 kHz were used in this thesis. For more elaborate KPFM studies, an exchange of the PLL might be advantageous to gain a larger margin for the choice of the modulation frequency.

Amplitude Modulation KPFM

KPFM can also be measured by minimizing the amplitude of the directly excited motion as in amplitude modulation KPFM (AM-KPFM) [12, 40]. To benefit from resonance enhancement, most setups use the second eigenresonance $f_1 \approx 6.3f_0$ as modulation frequency [41, 42]. As f_1 also shifts due to tip-sample interactions, it is advisable to track f_1 , or to be sure that the quality factor is low enough in order not to compromise the work function measurement.

KPFM condition

In both cases, the modulated component of a signal X is recorded using a lock-in amplifier and is minimized, *i.e.*, $\frac{\partial X}{\partial V} = 0$. In the case of AM-KPFM, the force is measured, so that the KPFM condition reads:

$$\frac{\partial F}{\partial V} = 0 \quad (2.16)$$

In the case of FM-KPFM³, the frequency shift is measured, so that the condition is:

$$\frac{\partial \Delta f}{\partial V} = 0 \quad (2.17)$$

According to Eqn. 2.10, Δf and the force are related by a complex integral [43]. In the case of small amplitudes, the frequency shift can be approximated by the force gradient (Eqn. 2.9) and the KPFM condition is:

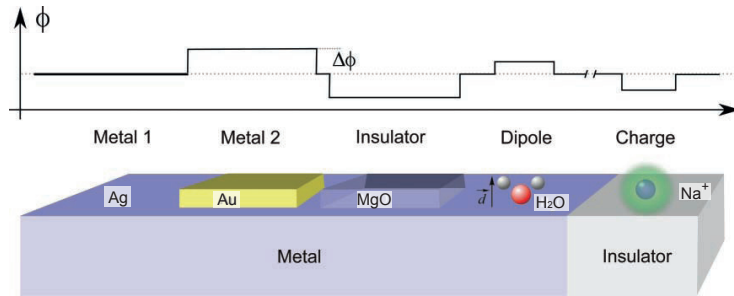
$$\frac{\partial^2 F}{\partial V \partial z} = 0 \quad (2.18)$$

In my measurements amplitudes of around 10 nm were used and this approximation does not apply, but Δf is situated between F , $\partial F/\partial z$ and the potential [31]. For simplicity, I will consider Eqn. 2.16 as the relevant condition for KPFM contrast throughout this thesis. For a quantitative description, the integration in Eqn. 2.10 needs to be carried out. One should keep in mind that the values measured by AM-KPFM and FM-KPFM are not expected to correspond to the same effective z -distance due to the necessary integration in FM-KPFM. Therefore, care has to be taken when comparing results obtained by FM-KPFM and AM-KPFM, especially if the z -dependence is considered. In this thesis, exclusively FM-KPFM measurements are shown.

³These considerations also apply in the static case for the acquisition of $\Delta f(V)$ curves.

Contrast Formation

Figure 2.12: Objects of different chemical compositions exhibit differences in the local work function on the surface (metal) or in the electrostatic surface potential (insulators). Adapted from [44].



An overview of some effects visible in KPFM measurements [36, 44, 45] is given in Fig. 2.12. On metals, information about the work function is gained. This work function can vary locally [46], due to different grain orientations [47] and adlayers like MgO [48] or NaCl [49]. Furthermore, adsorbed molecules [50, 51] can influence the measured KPFM signal. On insulators, different contrast is obtained above local charges [52, 53] and above dipoles for instance originating from molecular islands [54–58]. An introduction to the contrast mechanism of the total, measured KPFM signal, in this thesis denoted by ΔV , is given in the following for a step-wise modified plate capacitor. The calculation for the plate capacitor with and without dielectric material are taken from a draft [59] by P. Rahe.

Two metal plates: plate capacitor

The most simple way to model the electrostatic behavior of a metal tip in front of a metal sample, is using the model of a parallel-plate capacitor.⁴ In this case, no charges are localized between the plates, so that the electrostatic potential ϕ can be derived from the Laplace equation $\Delta\phi = 0$. When a voltage V_{DC} is applied between the plates separated by d and $\phi = 0$ at the

⁴Effects due to the modulation V_{AC} are not considered, but only the static contrast mechanism is discussed here.

lower plate, the electrostatic potential ϕ is:⁵

$$\phi_{cap}(z) = \frac{z}{d} V_{DC} \quad (2.19)$$

If the two plates consist of different metals, the work function difference $V_{CPD} = \Delta\Phi/e$ has to be taken into account and the electrostatic potential can be described by:

$$\phi_{cap}(z) = \frac{z}{d} (V_{DC} - \Delta\Phi/e) \quad (2.20)$$

Using $\vec{E} = -\nabla\phi$, the electric field between the plates is:

$$\vec{E}_{cap}(z) = -\frac{V_{DC} - \Delta\Phi/e}{d} \vec{e}_z \quad (2.21)$$

The capacitance $C = Q/V$ of a plate capacitor is known to be $C = \frac{\epsilon_0 A}{d}$ and the electrostatic energy is $W = \int_0^Q V dq = \frac{1}{2} \frac{Q^2}{C} = \frac{1}{2} C V^2$ [60]. From this we can calculate the force acting between the plates from the derivative of W with respect to the plate distance d :

$$\begin{aligned} \vec{F}_{cap} &= -\frac{\partial W}{\partial d} \vec{e}_d \\ &= -\frac{1}{2} \frac{\partial C}{\partial d} (V_{DC} - \Delta\Phi/e)^2 \vec{e}_z \end{aligned} \quad (2.22)$$

$$= \frac{\epsilon_0 A}{2d^2} (V_{DC} - \Delta\Phi/e)^2 \vec{e}_z \quad (2.23)$$

Using Eqn. 2.16, the KPFM signal follows from

$$\begin{aligned} \frac{\partial F_{cap}}{\partial V_{DC}} &= 0 \\ \frac{\epsilon_0 A}{d^2} (V_{DC} - \Delta\phi/e) &= 0 \\ \Delta V &= \Delta\phi/e \end{aligned} \quad (2.24)$$

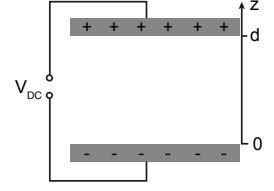


Figure 2.13: Parallel plate capacitor. If the two plates consist of different metals, a homogenous electric field builds up, which can be compensated by applying the appropriate bias V_{DC} .

⁵In this simple picture, the separation of the plates d corresponds to the tip-sample distance.

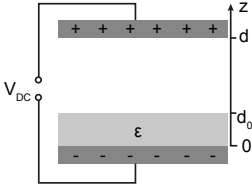


Figure 2.14: Parallel plate capacitor partially filled with a dielectric material with permittivity ϵ . Although the magnitude of the electric field differs from the empty capacitor, the same bias V_{DC} is required for compensation.

Thus, the Kelvin contrast ΔV in an experiment with metal tip and metal surface shows the differences in the contact potential. A realistic tip-sample geometry influences the capacitance (for a sphere in front of a plane see [27, 61]). However, as the KPFM condition is unaltered by a change in capacitance, this condition holds also for realistic tip-sample geometries.

Plate capacitor with dielectric

A dielectric layer changes the capacitance of the plate capacitor according to its relative permittivity ϵ_r . The total capacitance can be calculated by a series of capacitors.⁶

$$\begin{aligned}
 C_{cap+\epsilon_r} &= \frac{1}{\frac{1}{C_{dielectric}} + \frac{1}{C_{gap}}} \\
 &= \frac{1}{\frac{d_0}{\epsilon_0 \epsilon_r A} + \frac{d-d_0}{\epsilon_0 A}} \\
 &= \frac{\epsilon_0 A}{d - d_0 + d_0/\epsilon_r}
 \end{aligned} \tag{2.25}$$

Analogous to the capacitance, the potential drop across the capacitors is determined. The potential drop across the two capacitors is $\phi_{dielectric} = Q_{dielectric}/C_{dielectric}$ and $\phi_{gap} = Q_{gap}/C_{gap}$ with $\phi_{dielectric} + \phi_{gap} = V_{DC} + \Delta\Phi/e$. Further using $Q_{gap} = Q_{dielectric}$ yields for the potential drop across the dielectric

$$\phi_{dielectric} = \frac{d_0}{\epsilon_r(d - d_0 + d_0/\epsilon_r)}(V_{DC} - \Delta\Phi/e) \tag{2.26}$$

and the potential drop across the gap

$$\phi_{gap} = \frac{(d - d_0)}{d - d_0 + d_0/\epsilon_r}(V_{DC} - \Delta\Phi/e). \tag{2.27}$$

⁶This assumes a constant potential on the surface of the dielectric, which might not be true for more realistic tip-sample geometries like for instance a sphere in front of a plane.

If the potential at the lower plate is set to zero, the electrostatic potential is given by:

$$\phi_{cap+\epsilon_r} = \begin{cases} \frac{z}{d_0}\phi_{dielectric}, & 0 \leq z \leq d_0 \\ \phi_{dielectric} + \frac{z-d_0}{d-d_0}\phi_{gap}, & d_0 < z \leq d \end{cases} \quad (2.28)$$

Using $W = 1/2CV^2$, the force acting between the plates is again given by $\vec{F} = -\partial W/\partial d \vec{e}_d$:

$$\begin{aligned} \vec{F}_{cap+\epsilon_r} &= -\frac{1}{2} \frac{\partial C}{\partial d} (V_{DC} - \Delta\Phi/e)^2 \vec{e}_d \\ &= \frac{\epsilon_0 A}{2(d-d_0+d_0/\epsilon_r)^2} (V_{DC} - \Delta\Phi/e)^2 \vec{e}_d \end{aligned} \quad (2.29)$$

Then the KPFM signal follows accordingly:

$$\begin{aligned} \frac{\partial F_{cap+\epsilon_r}}{\partial V_{DC}} &= 0 \\ \frac{\epsilon_0 A}{(d-d_0+d_0/\epsilon_r)^2} (V_{DC} - \Delta\Phi/e) &= 0 \end{aligned} \quad (2.30)$$

$$\Delta V = \Delta\Phi/e \quad (2.31)$$

The dielectric material does, therefore, not influence the minimal force condition with respect to the voltage, *i.e.*, the electrostatic potential between tip and backelectrode is measured ($\Delta V = V_{CPD}$). Thus, in the case of a nonpolar dielectric material, in the absence of charges and of corrugations on the scale of the tip size, ΔV is independent of the tip-sample distance, like in the case without dielectric material. In the case of a more realistic geometry, the system cannot be described by a series of capacitors as the potential at the dielectric-vacuum interface is not constant. Still, an analytic approach based on an infinite series of image charges shows that for the case of a metallic sphere in front of an infinite dielectric half-space [62], the KPFM signal is not influenced by the geometry. More complex cases need to be calculated numerically [63].

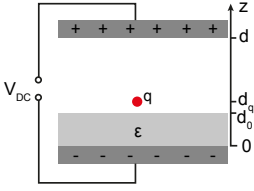


Figure 2.15: Parallel plate capacitor partially filled with a dielectric material and with a point charge located in the vacuum gap.

Capacitor with local charges

On ultrathin insulating layers, ΔV typically differs from the KPFM signal of the bare substrate. Measurements on one or two monolayer KCl on Ag(111) show a shift of ΔV in quantitative agreement with UPS measurements [64], indicating that not only the capacitance changes, but also the zero-force condition. Similar observations occur for organic molecules on metals [65], where additionally an influence of the orientation of the adsorbed molecules is observed [66]. Such effects are attributed to the formation of interface dipoles [50]. In this case, the electrostatic energy is not solely described by the capacitive interaction, but local charges need to be considered.

Introducing local charges into a capacitor influences the potential on the metal surfaces. If the potential on the metal surfaces is kept constant, the energy consumed by a battery to adjust the charge distribution to fulfill this condition needs to be considered [67]. Kantorovich *et al.* [67, 68] proposed the following expression for the effective energy in a capacitor with local charges, which includes the battery that maintains the potential on the metals:

$$W_{eff} = -\frac{1}{2}CV^2 + \sum_i q_i \phi^0(\vec{r}_i) + \frac{1}{2} \sum_{i,j} q_i q_j \phi_{ind}(\vec{r}_i, \vec{r}_j) + W_{coul} \quad (2.32)$$

This effective energy consists of four terms. The first term describes the capacitive interaction due to the surface charges on the metals. The second term is a sum over the interactions of a local charge q_i with the potential of the capacitor without charges ϕ_0 at the position of the local charge. The third term is a sum over the interaction of charge q_i with the image potential created by charge q_j , denoted by $q_j \phi_{ind}(\vec{r}_i, \vec{r}_j)$. Finally, the Coulomb interaction between the local charges is included.

In the case of the plate capacitor with dielectric and one local charge q at d_q with $d_0 < d_q < d$ (see Fig. 2.15), the effective energy is given by (see also supplementary information of [61]):⁷

⁷Eqn. 2.32 was derived with the assumption of finite metal conductors. I as-

$$W = -\frac{1}{2}C_{cap+\epsilon_r}(V_{DC} - \Delta\Phi/e)^2 + q\phi_{cap+\epsilon_r}(d_q) + \frac{1}{2}q\phi_{ind} \quad (2.33)$$

For the KPFM contrast only those components are relevant which remain after solving the condition:

$$\frac{\partial}{\partial V_{DC}} \frac{\partial}{\partial d} W = 0 \quad (2.34)$$

I assume Eqn. 2.33 is twice differentiable and continuous in the second derivatives,⁸ then Schwarz' theorem applies and the derivatives are commutative:

$$\frac{\partial}{\partial d} \frac{\partial}{\partial V_{DC}} W = 0 \quad (2.35)$$

Accordingly, I only need to consider those terms further, which depend on V_{DC} . In agreement with [61, 69], I assume the Coulomb interaction (which would be inserted for multiple charges) and the image potentials do not depend on V_{DC} but only the coupling of charges with the capacitor is relevant. Consequently, in any case in which the given assumptions apply, only the potential of the geometry without any local charges needs to be determined. The relevant terms read:

$$\frac{\partial}{\partial d} \left[\frac{\partial}{\partial V_{DC}} \left(\frac{1}{2}C_{cap+\epsilon_r}(V_{DC} - \Delta\Phi/e)^2 \right) + \frac{\partial}{\partial V_{DC}} (q\phi_{cap+\epsilon_r}(d_q)) \right] = 0 \quad (2.36)$$

According to Eqn. 2.28 the potential of the plate capacitor with dielectric at the position of the local charge is given as:

$$\phi_{cap+\epsilon_r}(d_q) = \frac{\frac{d_0}{\epsilon_r} + d_q - d_0}{d - d_0 + \frac{d_0}{\epsilon_r}} (V_{DC} - \frac{\Delta\Phi}{e}) \quad (2.37)$$

sume, the expression to be an approximation in the center of a plate capacitor with finite area A . Barth *et al.* state in the supplementary information to [61] the approximation of a sphere in front of a plate (which is infinite) is a good approximation compared to the correct potential if the additional local charge is placed on the symmetry axis. Still, I will only use the expression to qualitatively show that charges have an effect on the KPFM signal. For a quantitative description a realistic tip-sample geometry needs to be considered.

⁸This holds at least for the first two terms for $d > d_0$.

The relevant terms of the derivative of W with respect to V_{DC} then read:

$$\frac{\partial W}{\partial V_{DC}} = C_{cap+\epsilon_r}(V_{DC} - \Delta\Phi/e) + q \frac{\frac{d_0}{\epsilon_r} + d_q - d_0}{d - d_0 + \frac{d_0}{\epsilon_r}} \quad (2.38)$$

Solving the KPFM condition results in (The capacitive term is equivalent to Eqn. 2.31):

$$\begin{aligned} 0 &= -\frac{\partial^2 W}{\partial d \partial V} \\ 0 &= \frac{\partial}{\partial d} \left[\frac{\epsilon_0 A}{(d - d_0 + d_0/\epsilon_r)} (V_{DC} - \frac{\Delta\phi}{e}) + q \frac{\frac{d_0}{\epsilon_r} + d_q - d_0}{d - d_0 + \frac{d_0}{\epsilon_r}} \right] \\ 0 &= \frac{\epsilon_0 A}{(d - d_0 + d_0/\epsilon_r)^2} (V_{DC} - \frac{\Delta\phi}{e}) + q \frac{d_0/\epsilon_r + d_q - d_0}{(d - d_0 + d_0/\epsilon_r)^2} \\ 0 &= \epsilon_0 A (V_{DC} - \frac{\Delta\phi}{e}) + q (d_0/\epsilon_r + d_q - d_0) \\ \Delta V &= q \frac{-d_0/\epsilon_r - d_q + d_0}{\epsilon_0 A} + \Delta\phi/e \end{aligned} \quad (2.39)$$

Thus, in the presence of local charges, the KPFM signal shows an additional contribution, which is additive to the contact potential difference. Using $d_0=1$ nm, $d_q=1.1$ nm, $\epsilon_r=9$, one electron on an area of 10 nm \times 10 nm causes a shift of about 35 mV in the KPFM signal, on an area of 1 nm \times 1 nm a shift of 3.5 V, which seems to be reasonable. According to this calculation charges lead to KPFM contrast also on insulating substrates. Thus, the comparison of different surface regions gives information about the relative charge state of, *e.g.*, chemically different molecular structures [57].

In the simple case of a parallel-plate capacitor, the additive term ΔV_q does not depend on the tip-sample distance d (due to the homogenous electric field). For the more complex geometry of a sphere in front of a plane, the term was determined to be [61, 69]:

$$\Delta V = -\frac{q d_q}{2\pi R^2} (1 + R/d) - \Delta\Phi/e \quad (2.40)$$

with R the radius of the sphere, d the distance between sphere and plane and d_q the distance of the charge to the plane. For this more realistic geometry, a distance dependence occurs.

For a quantitative description of the KPFM signal only the potential ϕ^0 and the capacity C of the system without local charges are required [61, 67, 68]. ϕ^0 and C are only known analytically for a few rather simple, symmetric systems, like the case of a sphere above a plane. For a quantitative description of a realistic tip-sample geometry, numerical calculations, e.g., by finite elements methods like shown in [63] are needed.

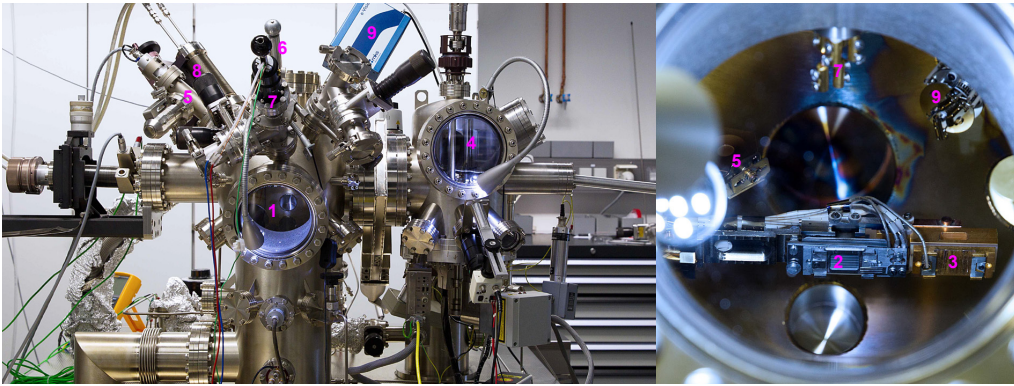


Figure 2.16: UHV chamber composed of preparation chamber (1) and AFM chamber (4), equipped with a manipulator with heating (2) and cooling (3) stage, a sputter gun (5), a sample cleaver (6), a molecule sublimator (7), a quartz microbalance (8) and a quadrupole mass spectrometer (9).

2.4 Experimental Setup

UHV Chamber

All measurements were carried out using a commercial VT AFM 25 from Omircon NanoTechnology (Taunusstein, Germany). Sample preparation and measurements were performed inside the ultra-high vacuum (UHV) system, which exhibits a base pressure below 1×10^{-10} mbar. The UHV system consists of three chambers:

- The preparation chamber (marked in Fig. 2.16 with 1) with the manipulator (Vacuum Generators Ltd., Hastings, United Kingdom) for heating (2) and cooling (3).
- The AFM chamber (4), where the AFM is situated and where tips and samples can be stored in a carousel.
- The load-lock on the back side for transferring cantilevers and samples from atmosphere to UHV without breaking the vacuum.

The preparation chamber is additionally equipped with a sputter gun ISE10 from Omicron for tip preparation (5), a home-built crystal cleaver for *in-situ* sample cleavage (6), two home-built molecule sublimators (one mounted at 7), a quartz microbalance

from Inficon (Bad Ragaz, Switzerland) to measure deposition rates (8) and a quadrupole mass spectrometer e-Vision+ (MKS Instruments, Crewe, United Kingdom) for residual gas analysis (9).

The AFM setup was optimized by R. Bechstein [70] by introducing a new light source, a home-built preamplifier and a PLL (easyPLL, Nanosurf AG, Liestal, Switzerland) for signal demodulation, resulting in a noise background of $(328 \pm 2) \text{ fm}/\sqrt{\text{Hz}}$ of the modified system. As scan controller, the Matrix electronics from Omicron are employed with software version Matrix V3.0 or Matrix V3.1 in the frequency modulation nc-AFM mode. A digital lock-in amplifier HF2LI (Zurich Instruments AG, Zurich, Switzerland) serves as lock-in and feedback loop for FM-KPFM measurements. In this setup, all voltages are applied to the tip, while the sample is at ground.

Sample Preparation

Cantilever

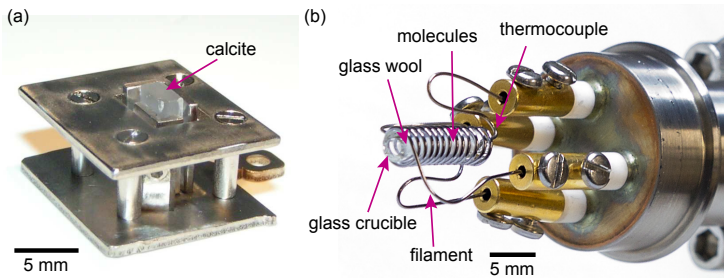
N-doped silicon cantilevers of the type PPP-NCH from NanoWorld (Neuchâtel, Switzerland) with eigenfrequencies about 300 kHz, Q-factors around 20000 and specified tip radius below 10 nm are used. The AFM measurements are carried out using an oscillation amplitude of about 10 nm. To remove oxide layer and surface contaminations, the cantilevers are Ar^+ sputtered at 2 keV for 5 min *prior* to use.

Substrate

All measurements are performed on calcite (10.4). Optical quality calcite crystals are supplied by Korth GmbH (Altenholz, Germany). After cutting, the crystal is clamped into a home-built samples holder [71, 72], displayed in Fig. 2.17 (a). After transfer into the UHV system, the crystal is outgassed by annealing at 720 K for at least two hours. Using a scalpel blade mounted at a

2 Methods

Figure 2.17: (a) Sample holder with calcite crystal for *in situ* cleavage. Adapted from [71]. (b) Home-built Knudsen cell mounted at home-built molecule sublimator.



wobblestick [72], the crystal is cleaved *in situ*. To remove surface charges, which occur due to the cleavage process, the crystal is annealed for a second time to 640 K for about one hour.

Samples are heated using a pyrolytic boron nitride heater attached below the heating stage of the manipulator (2 in Fig. 2.16). A thermocouple is mounted about 25 mm away from the sample. The temperatures at the sample plate given in this thesis are obtained by a calibration curve supplied by Omicron for this manipulator (see Tab. 2.1). As the real temperature at the sample surface depends on the specific sample holder in use, the thermal conductivity of the sample and the length of the sample, the given temperatures are only a rough estimate.

Voltage / V	5.0	6.0	7.0	7.5	8.0	9.0	12.5	15.5
T / K	400	440	490	510	520	550	640	720

Table 2.1: Temperatures at the sample plate for specific voltages determined using the calibration curve provided by Omicron, which correlates the temperature of the thermocouple with the temperature at the sample plate.

Molecules

Molecules are deposited onto the calcite (10.4) surface with reproducible deposition rates using a home-built molecule sublimator consisting of a Knudsen cell at a linear translator [71]. The sublimator is mounted at a T-piece of the chamber, which

Molecule	Purity	$p_{\text{vapor}} / \text{Torr}$ [73]	$T_{\text{sub}} / \text{K}$	$r_{\text{dep}} / \text{ML/min}$
Pholoroglucinol	97%	$8.3 \cdot 10^{-5}$	337	0.05
2-HBA	99%	$4.5 \cdot 10^{-5}$	RT	0.3
3-HBA	99%	$2.2 \cdot 10^{-5}$	320	0.005
4-HBA	99%	$4.5 \cdot 10^{-5}$	314	0.06
3-ABA	98%	$1.4 \cdot 10^{-5}$	326	0.02
4-ABA	99%	$4.5 \cdot 10^{-5}$	311	unknown
2,3-DHBA	99%	$6.9 \cdot 10^{-6}$	RT	unknown
2,4-DHBA	97%	$1.3 \cdot 10^{-7}$	338	0.04
2,5-DHBA	99%	$2.4 \cdot 10^{-7}$	342	0.08
2,6-DHBA	98%	$2.3 \cdot 10^{-5}$	RT - 320	unknown
3,4-DHBA	97%	$1.8 \cdot 10^{-7}$	347	0.01
3,5-DHBA	97%	$1.7 \cdot 10^{-7}$	344	0.003
3-HBAmide	not specified	$2.0 \cdot 10^{-4}$	338 (347)	0.01 (0.05)
3,5-DHBAmide	97%	$8.4 \cdot 10^{-9}$	378	<0.01

Table 2.2: Specified purities and predicted vapor pressures [73] for the molecules employed in this thesis as well as the corresponding sublimation temperatures and deposition rates in monolayer (ML) per minute.

allows to change molecules without breaking the vacuum. With the translator, the crucible is moved into the chamber to a position about 90 mm apart from the sample surface.

To manufacture the Knudsen cell (Fig. 2.17 (b)), two thermocouple wires are spot welded and melted into a glass crucible. A tungsten wire is coiled around the crucible as filament. The crucible is filled with the molecules and capped with glass wool to allow for the upside-down position of the mounted sublimator. For each type of molecule, a new crucible is fabricated to avoid contamination.

All molecules used in this thesis are purchased from Sigma-Aldrich (Munich, Germany) or Alfa Aesar (Karlsruhe, Germany). Specified purities, predicted vapor pressures, employed sublima-

tion temperatures $T_{\text{sublimation}}$ and deposition rates $r_{\text{deposition}}$ are given in Table 2.2. A quartz microbalance installed at a test chamber was used to find the sublimation temperatures. As most of the molecules sublime at quite low temperatures in UHV, the rates given here are estimated by the resulting molecular coverage on the surface.

Data Analysis

The images were analyzed and processed using Gwyddion [74]. Depending on the feedback conditions either topography (z) or Δf images are presented. In the upper right corner, image type and fast and slow scan directions are depicted. For Δf images the colorscale is inverted, such that for z and Δf images bright contrast corresponds to large attractive interaction, dark contrast to small attractive or even repulsive interaction. Except for the inversion of the colorscale, Δf images show raw data. The topography images were plane-subtracted. For large-scale images (width ≥ 200 nm) a polynomial background was subtracted if necessary. If not stated otherwise, no further image treatment was applied. For KPFM measurements raw data is shown if not stated otherwise.

For quantitative analysis of lateral distances, the images were calibrated ($f_x = 0.83, f_y = 0.91$) and distortions due to linear drift were carefully corrected by an established routine [75].

3 Molecular Self-Assembly on Insulators

Contents

3.1 Basic Principles	34
3.2 Bulk Growth and Dewetting	35
3.3 Anchoring Strategies	37
Surface Energy	37
Specific Molecule-Substrate Interactions . . .	38
3.4 Tuning the Self-Assembly	43

Molecular self-assembly is the spontaneous association of molecules under equilibrium conditions into stable, structurally well-defined aggregates joined by noncovalent bonds.

Whitesides *et al.* in [2]

In this chapter, I briefly review the basic principles of molecular self-assembly, which are mainly known from studies on metal surfaces. The comparatively weak molecule-substrate interaction on insulating substrates, in contrast, can lead to the growth of bulk crystals and also to complex transient structures through dewetting. The limitations associated with the weak interaction can be overcome by anchoring the molecules towards the substrate through the choice of appropriate molecule-substrate systems. An overview of possible interaction mechanisms of organic molecules with insulating substrates reasons why a specific molecule-substrate system is chosen within this thesis, which allows to tune the self-assembled patterns.

Self-assembly is a nondissipative structural order on a macroscopic level, because of collective interactions between multiple (usually microscopic) components that do not change their character upon integration into the self-assembled structure. This process is spontaneous because the energy of the unassembled components is higher than the self-assembled structure, which is in static equilibrium, persisting without the need for energy input.

Definition by Halley and Winkler in [76].

Self-organization is a dissipative nonequilibrium order at macroscopic levels, because of collective, nonlinear interactions between multiple microscopic components. This order is induced by interplay between intrinsic and extrinsic factors, and decays upon removal of the energy source. In this context, microscopic and macroscopic are relative.

Definition by Halley and Winkler in [76].

3.1 Basic Principles

For molecules to arrange spontaneously into a stable, equilibrium pattern on a surface, the energies of the molecules with respect to the surface have to fulfill several conditions [77]. First of all, the molecules need to adsorb on the surface, which is only possible if the kinetic energy of the molecules E_{kin} ¹ is smaller than the binding energy E_{MS} to the surface. On the surface, the molecules can only diffuse and thereby find their minimum energy position when their thermal energy is sufficient to overcome the diffusion barrier E_d . Homogeneous structures with only a small number of defects form, if the molecule-molecule interaction E_{MM} is in a similar range as E_{kin} . Such a structure is stable, if E_{MM} is slightly larger than E_{kin} . In summary, stable substrate-templated patterns can form if [77]:

$$E_{MS} > E_{MM} \gtrsim E_{kin} > E_d . \quad (3.1)$$

These conditions are illustrated in Fig. 3.1 by a sketch depicting possible arrangements of the molecules depending on the energies and by a diagram showing the relative magnitude of the energies. In the case of the formation of the thermodynamic equilibrium structure being kinetically hindered, *i.e.*, $E_{kin} < E_d$, formation of ordered structures is referred to as self-organization [76, 78].

Further barriers not included in this simple expression can also be relevant, *e.g.*, barriers for the nucleation and dissociation of molecular islands. Besides, this expression ignores any entropic effects, which might be relevant, as an ordered structure is formed from previously unordered components.

While on metals many different molecules have been observed to form self-assembled structures and the mechanisms have been widely studied [5, 77, 78], the self-assembly on insulators is hampered because of the comparatively weak molecule-substrate interaction, which is often smaller than the molecule-molecule interaction.

¹This thermal energy of the molecule denotes an energy the molecule can overcome at a reasonable rate.

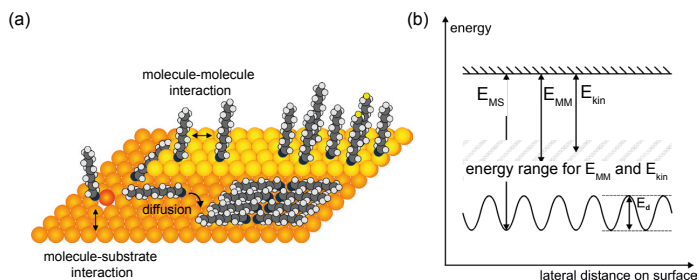


Figure 3.1: (a) Model illustrating molecules arranged on a surface according to different interactions. (b) For molecular self-assembly to occur, the energies involved should obey the energy condition $E_{MS} > E_{MM} \gtrsim E_{kin} > E_d$. Adapted from [77].

3.2 Bulk Growth and Dewetting

On insulating substrates E_{MS} is generally quite weak, which commonly results in two phenomena: dewetting and bulk growth.

If the molecule-substrate interaction is smaller than the molecule-molecule interaction ($E_{MS} < E_{MM}$), it is more advantageous for the molecules to grow on top of a molecular island than on the bare substrate, resulting in molecular crystals confined at substrate step edges or defects, as shown for PTCDA on KBr(001) [79] in Fig. 3.2. In such a case, the structure formation does not depend on the substrate eliminating the possibility to tune the arrangement and achieve a greater variety of structures.

The equilibrium structure is often not reached directly after deposition, but the molecules initially arrange into layers on the surface, *i.e.*, they wet the surface. Upon time, the thermodynamically more stable bulk structure forms by the molecules piling up to multilayers, *i.e.*, they dewet from the surface. Two cases have been identified for this so-called dewetting to occur [80]. The first is the structure grown upon deposition is not the thermodynamically most stable. The second occurs when the thin film grown upon deposition is not the favorable structure for a thicker film. Because intermolecular and molecule-substrate interaction are in a similar range, dewetting is commonly observed on insulating substrates. As the transition from the initial structure to the thermodynamically stable structure can require a considerable rearrangement, complex transient structures can result, which, depending on the energy barriers, can be stable

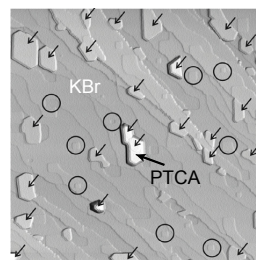
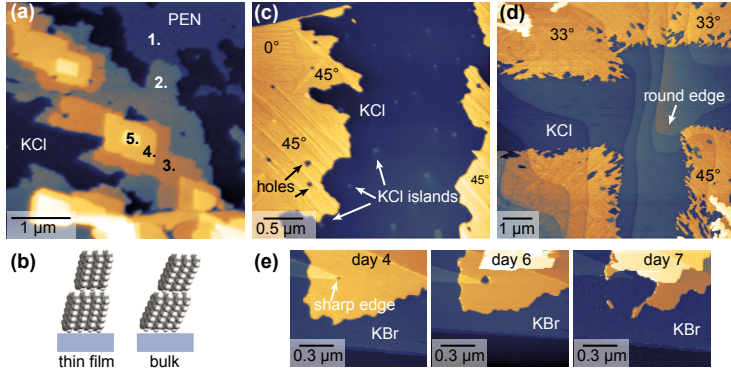


Figure 3.2: Bulk growth of PTCDA on KBr(001). PTCDA molecules do not form wetting layers or islands, but molecular crystals form on the surface. Adapted from [79].

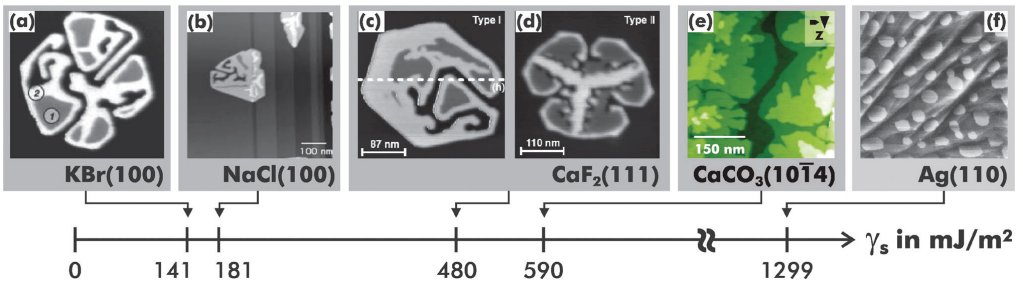
Figure 3.3: Dewetting of pentacene on KBr(001) and KCl(001). Three effects occur over time: (a) Monolayers pile up to multilayers. (c) - (e) A substructure forms on the monolayer islands and holes appear inside the islands, which transform into a fractal-like geometry. Adapted from [84]. (b) Sketch representing a thin film phase and a slightly more tilted bulk phase.



for significant time.

A widely-studied because technologically relevant example is the reconstruction of pentacene thin films [81, 82] for which the geometrical structure has been found to correlate with the charge transport properties of the thin film [83]. Depending subtly on film thickness and preparation conditions, different thin film phases or bulk phases grow, giving a wide opportunity for reconstruction. The post-deposition dewetting of a submonolayer of pentacene on alkali halides, for instance, shows three visible effects [84]: First of all, multilayers build at the expense of monolayers (Fig. 3.3 (a)), which might indicate the transition from a thin film phase to a bulk phase. Secondly, the substructure visible on the monolayer islands gets more pronounced (Fig. 3.3 (c) and (d)), hinting at a different registry with the substrate. Finally, holes appear inside the islands, which result in a fractal-like geometry (Fig. 3.3 (c)-(e)).

In summary, dewetting can result in a great variety of self-assembled or self-organized structures with complex geometry, as the competing energies are in similar range. These structures might represent a fragile equilibrium, which depends crucially on the temperature or other external influences.



3.3 Anchoring Strategies

To achieve a variety of stable self-assembled molecular structures on insulators, the substrate needs to play a more significant role, such that it templates the molecular structures. Two strategies have been proposed how to increase the molecule-substrate interaction on insulators by anchoring the organic molecules to the insulating substrate [6]. First of all, the surface energy can provide an indication for the strength of the molecule-substrate interaction. Secondly, specific molecule-substrate systems can be chosen deliberately to gain a desired molecule-substrate interaction.

Surface Energy

Despite being a macroscopic property, the surface energy provides a general trend for the contribution of the surface to E_{MS} [6, 80]. A descriptive example illustrating the applicability of this approach compares the self-assembly of C_{60} on different substrates [85]. On alkali halides with their low surface energy of about 150 mJ/m^2 , C_{60} forms complex dewetted patterns as shown in Fig. 3.4 (a) and (b). A similar behavior is found on CaF_2 with a surface energy of 480 mJ/m^2 (Fig. 3.4 (c) and (d)). On calcite (10.4), however, with a surface energy of 590 mJ/m^2 wetting islands form (Fig. 3.4 (e)). Still, the molecules form multilayers before the monolayer is complete. Only on metals, where the surface energy exceeds 1000 mJ/m^2 , layer-by-layer growth is observed.

Figure 3.4: The structure formation of C_{60} on various substrates ordered according to their surface energy. On insulators with surface energies up to 480 mJ/m^2 complex dewetted patterns occur. Wetted islands form on calcite with a surface energy of 590 mJ/m^2 and on metals with surface energies exceeding 1000 mJ/m^2 . Adapted from [85].

Bond type	Typical strength	Typical range	Bond characteristics
van-der-Waals	$\approx 0.02\text{-}0.1$ eV	<1 nm	unspecific
electrostatic	$\approx 0.1\text{-}2.5$ eV	long-range	unspecific
hydrogen bonds	$\approx 0.1\text{-}0.6$ eV	≈ 0.25 nm	specific + directional

Table 3.1: Interaction types with typical interaction energy and typical bond length.

Consequently, the surface energy provides a criterion to predict the general trend of how easily molecules form monolayer patterns on a specific substrate.

Specific Molecule-Substrate Interactions

The group of bulk insulating substrates is rather heterogeneous.² Accordingly, the trend given by the surface energies might not be correct for specific molecules as they might provide additional contributions to the molecule-substrate interaction. Most prominent are contributions by van-der-Waals, electrostatic and hydrogen bonding interactions with their main characteristics summarized in Tab. 3.1. Adapting the molecule-substrate system intentionally by deliberately exploiting a specific interaction can lead to substrate-templated patterns even on surfaces with low surface energies. In the following, I discuss how to take advantage of different molecule-substrate interactions.

Role of van-der-Waals Interactions

Van-der-Waals interactions are always present and, thus, contribute to the molecular self-assembly [86]. Due to their long-range and additive character, van-der-Waals interactions are not

²On metals, in contrast the interaction is more homogeneous as mostly carbohydrates are studied, for which the orbitals of the molecules interact via hybridization with the orbitals of the metals.

site-specific (see also Chap. 2.2). Therefore, van-der-Waals interactions do not increase the templating effect and stable wetting islands based on such interactions are difficult to achieve.

Role of Electrostatic Interactions

By deliberate design of polar molecules, anchoring of organic molecules towards ionic substrates has been achieved. Molecular building blocks have been substituted with polar end groups such that the expected assembly matches the substrate periodicity. Using this strategy, substrate-templated monolayer islands [56, 87, 88] and stable multilayer islands oriented along substrate directions [89, 90] have been gained on KBr(001).

The influence of the molecule-substrate matching has been investigated by comparing the assembly of a zwitterionic molecule on several alkali halide surfaces [88]. Despite the different substrate unit cells, the molecules form monolayer islands with the same molecular repeat unit. However, they exhibit different moiré patterns suggesting that the overall molecule-substrate interaction is increased but no highly specific substrate-templating dominates the arrangement. In contrast, the pattern is determined by intermolecular interactions. Similarly, moiré patterns have been found for islands of deprotonated carboxylic acids adsorbed on calcite (10.4) [91, 92]. For a molecular backbone with rigidly bound polar groups but flexible nonpolar groups, no moiré is observed [93]. The molecules are assumed to arrange at the electrostatically most favorable positions with the nonpolar anchors being flexible enough to nevertheless enable intermolecular interaction.

A stronger polarity of the end groups has been found to increase the binding energy of the single molecules, while the stability of the self-assembled structure is only increased if the pattern formed matches the substrate periodicity [58]. A further increase of the binding energy by increasing the number of the polar endgroups is as well only possible for both functional groups matching the substrate periodicity.

In summary, the success of anchoring molecules electrostatically to the substrate depends crucially on the balance of molecule-substrate matching and intermolecular interaction. Furthermore, KPFM measurements, indeed, evidence the presence of

Dimer	Energy (eV)	d_0 (Å)	Ref	Classification
$[\text{F}-\text{H}-\text{F}]^-$	1.69	2.3	[94]	
$[\text{H}_2\text{O}-\text{H}-\text{OH}_2]^+$	1.43	2.4	[95]	strong
$[\text{H}_3\text{N}-\text{H}-\text{NH}_3]^+$	1.04	2.7	[95]	
$\text{O}=\text{C}-\text{OH}\cdots\text{O}=\text{C}-\text{OH}$	0.32	2.8	[96]	moderate
$\text{HOH}\cdots\text{Bz}$	0.14	3.6	[97]	weak
$\text{C}=\text{CH}_2\cdots\text{C}=\text{C}$	0.02	-	[98]	

Table 3.2: Calculated energies of hydrogen bonds. Bz=benzyl. For more information see [99]. Strong hydrogen bonds are strongly covalent and exhibit a strong directionality. Moderate hydrogen bonds are of mostly electrostatic origin and show a moderate directionality. Weak hydrogen bonds are of electrostatic and dispersive nature with a weak directionality.

electrostatic forces for organic molecules supported on insulating substrates [56–58, 84]. To further understand the character of these electrostatic interactions, distance dependent KPFM measurements are explored in Chap. 8.

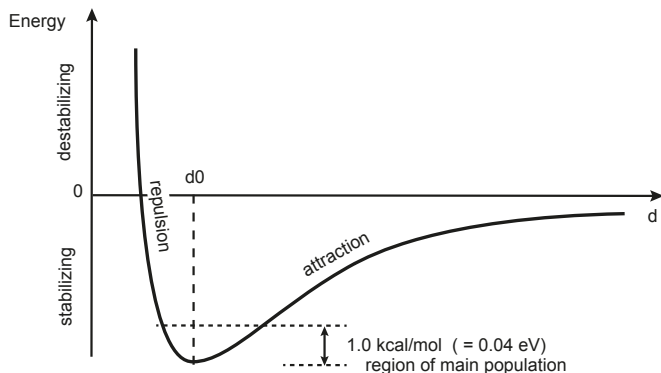
Role of Hydrogen Bonds

An opportunity for a highly selective assembly is to exploit hydrogen bonding.

The hydrogen bond is an attractive interaction between a hydrogen atom from a molecule or a molecular fragment X–H in which X is more electronegative than H, and an atom or a group of atoms in the same or a different molecule, in which there is evidence of bond formation.

Definition proposed to the IUPAC in 2011 [100].

The hydrogen bond is an attractive, directional interaction which results from a combination of electrostatic, covalent and dispersion contributions [99–102]. Depending on the composition



of this interaction between a hydrogen bond donor $X-H$ and an acceptor $Y-Z$, the interaction energy of the hydrogen bond $X-H \cdots Y-Z$ can range from 0.02 - 1.70 eV (see Table 3.2). Strong hydrogen bonds are strongly covalent, moderate hydrogen bonds are mostly electrostatic and weak hydrogen bonds are of electrostatic and dispersive nature. Since a hydrogen bond is not easy to identify, the above given definition was recommended to the IUPAC in 2011 together with a list of criteria, which should help to identify the formation of a hydrogen bond [100]. Here, I recall those characteristics of a hydrogen bond, which might be relevant for the molecular self-assembly on insulators.

The energy of the hydrogen bond is related to the *bond length* as shown in Fig. 3.5, with the long-range interaction being determined by electrostatics. Therefore an elongation of a hydrogen bond from optimal geometry increases the electrostatic contribution to the hydrogen bond [99]. Real hydrogen bonds do typically not exist with a distance d_0 corresponding to the minimum energy but with a distance in a range corresponding to an energy range within 0.04 eV (1.0 kcal/mol) from the optimum energy [103].

Not only the length of the hydrogen bond correlates with its strength, but also its *directionality*. Usually a hydrogen bond is linear. The degree of the directionality of the bond depends on the polarity of the proton donor [104]. While an $R-O-H \cdots O=C$ bond is strongly directional, a wider range of angles occurs for less polar bonds (Fig. 3.6). At the acceptor side, the direction-

Figure 3.5: Schematic representation of a typical potential of a hydrogen bond. Most hydrogen bonds in crystal structures do not exhibit the optimal bond length, but a bond length that slightly deviates from d_0 . Graph according to [99].

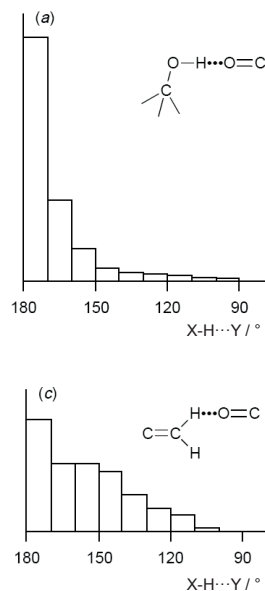


Figure 3.6: Histograms with the angular frequencies of $X-H \cdots O=C$ contacts indicating that the degree of directionality of the hydrogen bonds depend on the polarity of the proton donor. The distributions are weighted by $1/\sin\Theta$ and scaled in such a way that they cover the same area. Adapted from [104].

ality depends on the strength of the bond and thereby on the composition of the hydrogen bond. For strong hydrogen bonds, the geometry corresponds to the covalent bond formed by a hypothetical proton-transfer reaction. For moderate and weak hydrogen bonds the directionality is softer only depending on the orientation of the electron lone pairs. In the case of a carbonyl group, the oxygen lone pair lobes are in the $R_2C=O$ plane and form angles of about 120° with the $C=O$ bond. An exception are hydroxyl and water acceptors: no separation into two modes occurs and the entire acceptor lone pair region is accessible for hydrogen bonding [99, 103].

The correlation of the bond energy with bond length and bond directionality and the need for a particular bond partner results in a rather specific interaction, thereby creating a high selectivity, which makes hydrogen bonds ideal candidates for molecular self-assembly. On metals, extended hydrogen-bonded networks are found due to intermolecular hydrogen bonds, which guide the geometry of the supramolecular arrangement [5].

Additional opportunities arise when molecule-substrate hydrogen bonds are possible, as this allows for a highly selective templating effect. In this respect, oxide surfaces are promising candidates, as the surface oxygens can act as hydrogen bond acceptors [105, 106]. A few examples of substrate-templated islands already exist, for which such surfaces are combined with hydrogen bond donating molecules, *e.g.*, carboxylic acids on calcite [7, 107], proving the feasibility of this approach. The next question would be how to manipulate these systems in order to create a large variety of self-assembled structures intentionally.

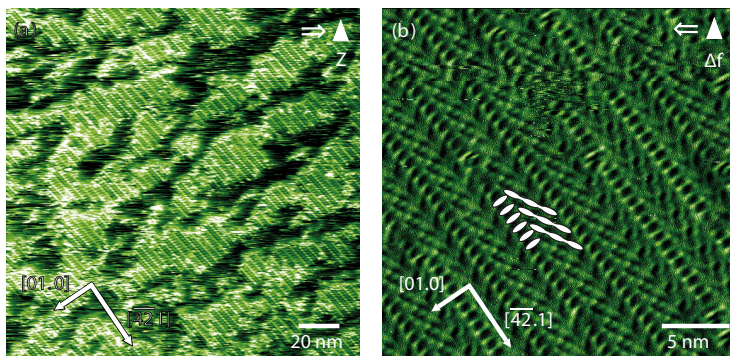


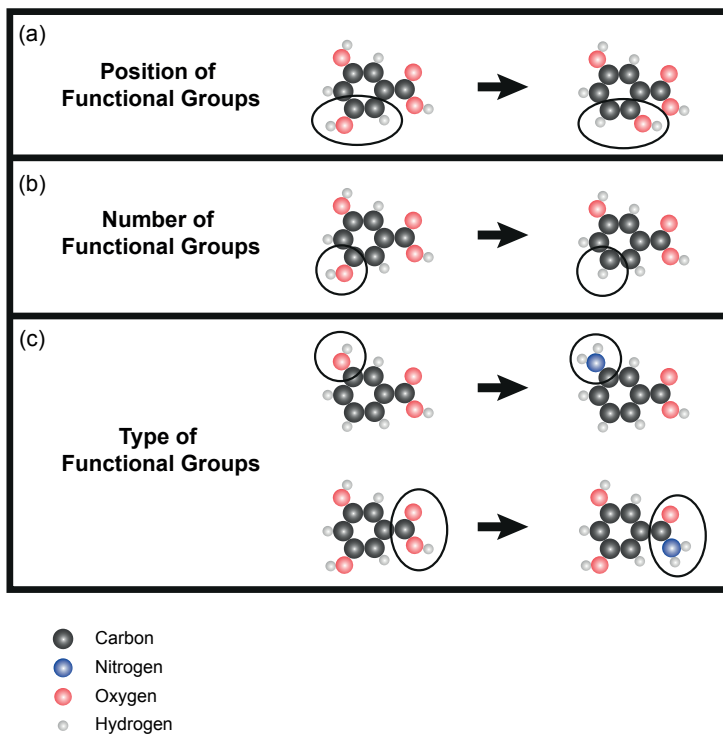
Figure 3.7: Biphenyldicarboxylic acid on calcite (10.4). (a) Overview nc-AFM image showing striped islands and streaks from mobile molecules. (b) Detail image of a molecular island. On the one hand, substrate-templated rows of molecules occur with a parallel, side-by-side arrangement along the $[4\bar{2}.1]$ direction. On the other hand, these lines are separated by areas where the molecules are arranged head-to-tail diagonal to the surface direction in a bulk-like phase. Adapted from [107].

3.4 Tuning the Self-Assembly

Combining the potential to form hydrogen bonds with the possibility for electrostatic interaction, carboxylic acids on calcite (10.4) are a promising system for molecular self-assembly on an insulating substrate. The coexistence of a substrate-templated pattern and a bulk-like pattern inside the monolayer islands of biphenyldicarboxylic acid on calcite (Fig. 3.7) points at a fragile balance of molecule-molecule and molecule-substrate interaction [107]. According to the above considerations, these interactions are dominated by rather specific molecule and substrate characteristics. Consequently, it might be possible to create a large variety of structures by only slightly varying the molecular building block.

An overview of the systematic variations of the molecular building block dihydroxybenzoic acid (DHBA) studied within this thesis is shown in Fig. 3.8. The first and maybe smallest variation is to switch to a molecule with the same functional groups but with a different arrangement of the functional groups, *i.e.*, a change of the substitution position of the functional groups. This variation is studied in Chap. 5 by comparing the self-assembly of all six constitutional isomers of DHBA. The second variation is removing one of two equal functional groups to study the influence of the number of the functional groups, see Chap. 6. Finally, the hydrogen bonding characteristics are slightly altered by substituting the hydrogen donating group by a similar group also ca-

Figure 3.8: Tuning the self-assembly by different strategies: (a) Changing the position of the functional groups (Chap. 5). (b) Changing the number of the functional groups (Chap. 6). (c) Changing the type of the functional groups (Chap. 7).



pable of hydrogen bonding. Chap. 7 illustrates the self-assembly of an aminobenzoic acid and two benzamides. A summary of all structures is shown in Appendices A and B.

4 Calcite and Benzoic Acids

Contents

4.1 The Insulating Substrate: Calcite	46
Calcite	46
The Calcite (10.4) Surface	47
4.2 The Molecular Building Block: Dihydroxybenzoic Acid	50
Interaction of Carboxyl Groups with Calcite	50
Interaction of Hydroxyl Groups with Calcite	51

This chapter introduces the molecule-substrate system studied within this thesis. First, I present the main characteristics of the insulating substrate calcite (10.4). Afterward, the molecular building block dihydroxybenzoic acid and its functionalities are discussed. The capability of both carboxyl and hydroxyl groups to interact with the substrate is demonstrated.

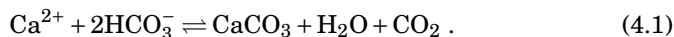


Figure 4.1: Clean calcite crystal with typical rhombohedral shape and birefringence.

4.1 The Insulating Substrate: Calcite

Calcite

Calcium carbonate (CaCO_3) is one of the most abundant minerals on earth [108, 109]. It occurs in sedimentary rocks like limestone and in marine shells. Also many industrial products contain CaCO_3 , such as paints, cement, cosmetics and pharmaceuticals. The formation of CaCO_3 is described by the following chemical equilibrium:



Depending on the conditions, pure CaCO_3 grows adopting one of three polymorphic structures: aragonite, calcite or vaterite. Under normal conditions, calcite is thermodynamically the most stable. Higher temperatures move the chemical equilibrium in Eqn. 4.1 to the right side, so that in warm waters calcite creation is favored. In turn, acidic water or acids move the equilibrium to the left side, so that calcite easily dissolves and is prone to weather.

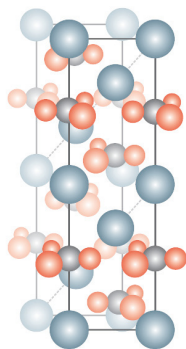


Figure 4.2: The hexagonal unit cell of bulk calcite. Adapted from [110].

Pure calcite crystallizes in a rhombohedral structure (see Fig. 4.1 and Fig. 4.2). It is transparent with an experimentally determined band gap of 6.0 eV [111]. The carbonate groups are tilted with respect to the most stable surface plane. This tilt of the carbonate groups leads to a different refraction index parallel and orthogonal to the carbonate groups causing strong birefringence.

Organic molecules can influence the growth of calcite crystals, resulting in a large variety of biominerals. The process of the formation of such minerals is widely studied [112, 113]. Interestingly, during this process characteristics of single molecules like the chirality of an amino acid can propagate to a macroscopic object [114].

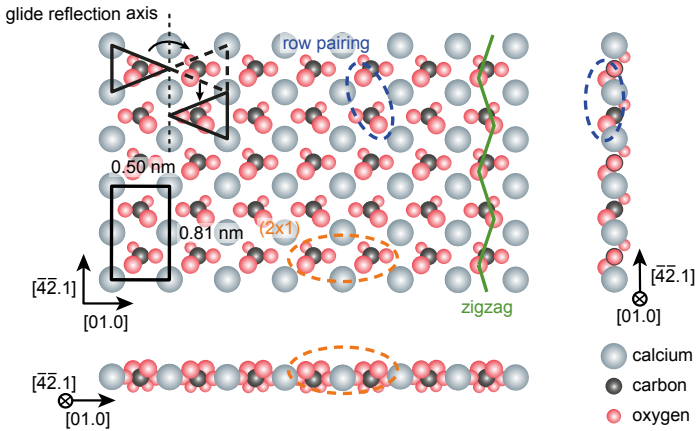


Figure 4.3: Model of the bulk-truncated (10.4) surface. Markers indicate the glide reflectional symmetry and typical surface contrasts.

The interaction of calcite with organic molecules as evident in biominerals combined with the large band gap, promise calcite to be an interesting insulating substrate for molecular self-assembly.

The Calcite (10.4) Surface

The most stable cleavage plane of calcite is the (10.4) plane [115] with a surface energy of 590 mJ/m^2 [116]. The surface directions of the (10.4) plane can be determined macroscopically, as the birefringence through this plane displaces the extraordinary ray along $[42.\bar{1}]$ (see Fig. 4.4 and [110]). For all images shown within this thesis the absolute surface directions were determined by this criterion *prior* to use.

Fig. 4.3 shows a model of the bulk-truncated (10.4) surface. Despite the hexagonal bulk structure, the surface exhibits a rectangular surface unit cell with a size of $0.50 \text{ nm} \times 0.81 \text{ nm}$. The unit cell contains two carbonate groups, which are differently tilted, such that the only symmetry operation of the surface is a glide plane reflection with the $[\bar{4}2.1]$ direction being the symmetry axis. As visualized for a triangle in Fig. 4.3, a surface area is transferred to an equivalent area by mirroring at $[\bar{4}2.1]$ followed by a translation of half a unit cell along the $[\bar{4}2.1]$ direction.

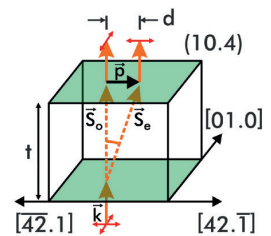
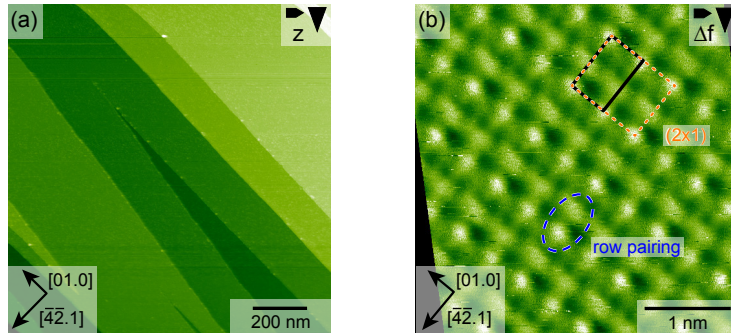


Figure 4.4: Birefringence through the (10.4) plane leads to two images, one displaced along $[42.\bar{1}]$. This gives the possibility to macroscopically determine the surface directions. Adapted from [110].

Figure 4.5: nc-AFM images of the calcite (10.4) surface. (a) Large scale topography showing cleaving edges. (b) Drift-corrected Δf image revealing a combination of the (2×1) reconstruction, row pairing and a slight lateral striped contrast.



Surface Reconstructions

A bulk-truncated surface is not necessarily stable, but surface reconstructions might occur. The calcite (10.4) surface can reconstruct with a (2×1) reconstruction [117–119]. In this reconstruction every second maximum along the [01.0] direction appears brighter resulting in a doubling of the unit cell (orange markers in Fig. 4.3). With the AFM, additionally, a large variety of surface contrasts are observed [120].

The row pairing contrast has been observed with AFM in aqueous solution [121, 122], under ambient conditions [118] and in UHV [120]. Along the $[\overline{4}\overline{2}.1]$ direction every second protrusion is imaged brighter creating a pair, possibly due to the different tilting of the carbonate groups (blue marker in Fig. 4.3). Interestingly, such a contrast removes the glide symmetry of the surface. If row pairing is not only an imaging contrast but a real surface reconstruction, the calcite (10.4) surface is chiral [123] and might be linked to the homochirality of life [124].

Another prominent imaging contrast is a zigzag along $[\overline{4}\overline{2}.1]$ (green marker in Fig. 4.3), following the pattern of the protruding oxygens. It is tempting to deduce from these two regularly occurring imaging contrasts that oxygen is responsible for the contrast in AFM.

Fig. 4.5 shows calcite imaged with nc-AFM in UHV. Cleavage results in a variety of step edges (Fig. 4.5 (a)), which maintain under UHV conditions, even when they are polar. Typical high-

resolution images on a terrace show a variety of surface contrasts simultaneously. In Fig. 4.5 (b), the (2×1) reconstruction and the row pairing contrast are visible, as along both main surface directions every second protrusion appears brighter. Additionally, a lateral striped contrast might be visible, with every second row along $[01.0]$ resembling a stripe rather than individual protrusions (contrast L6 in $[120]$).

From such an AFM image, only the relative surface directions can be deduced, as the orientation of the carbonate groups cannot be retrieved. In this thesis, the determination of the absolute surface orientation was carried out using the macroscopic measurement based on birefringence.

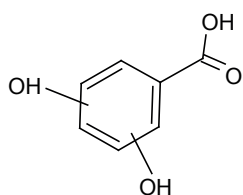


Figure 4.6: Chemical structure of dihydroxybenzoic acid (DHBA). Depending on the positions of the hydroxyl groups, different isomers exist.

4.2 The Molecular Building Block: Dihydroxybenzoic Acid

The molecular building block studied in this thesis is dihydroxybenzoic acid (DHBA). DHBA (Fig. 4.6) has three functionalities: the benzene core, the carboxyl group and the hydroxyl groups. These functionalities provide promising potential for intermolecular interaction: Benzene cores can interact via π - π -stacking, while both, carboxyl and hydroxyl groups, can form hydrogen bonds. Regarding the molecule-substrate interaction, the benzene core is not expected to interact specifically with calcite. A planar hydrocarbon, which was specifically synthesized to only interact via van-der-Waals interactions, was found to form bulk crystals on calcite at room temperature [110]. According to calculations, the carboxyl group can interact with calcite via hydrogen bonds [105]. Experimental observations hint at an interaction of both, carboxyl groups and hydroxyl groups, with calcite as shown in the following.

Interaction of Carboxyl Groups with Calcite

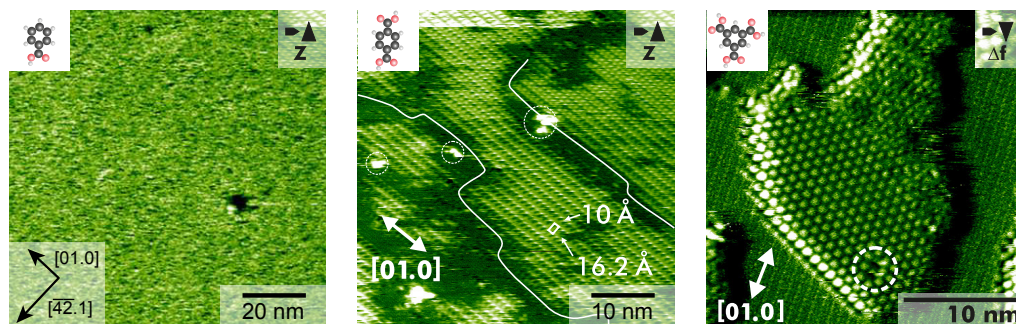


Figure 4.7: Self-assembly of benzene substituted with (a) one, (b) two and (c) three carboxylic groups on calcite. (a) Courtesy of [Personal data removed]. (b) and (c) adapted from [36].

Fig. 4.7 reveals the self-assembly of benzene substituted with one, two and three carboxylic groups. Benzoic acid does not form a stable, ordered pattern at room temperature, but sublimation results in a monolayer of diffusive molecules.¹ Terephthalic acid

¹These measurements were carried out by [Personal data removed].

forms diffusive, striped islands with a (2×2) superstructure in a distorted bulk-like arrangement [7]. Trimesic acid arranges into stable quasi-hexagonal islands commensurate to the substrate [7]. Thus, hydrogen-bonded networks are formed when intermolecular hydrogen bonds between the carboxylic groups are possible, *i.e.*, for at least two carboxylic groups per molecule. Moreover, these structures are substrate-templated, which demonstrates that the carboxylic acid groups interact with calcite.

Interaction of Hydroxyl Groups with Calcite

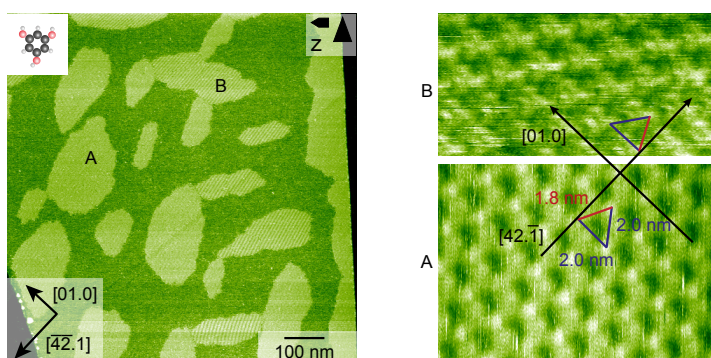


Figure 4.8: Self-assembly of 1,3,5-Trihydroxybenzene on calcite. The molecules arrange into two quasi-hexagonal patterns mirrored along the $[4\bar{2}.1]$ direction.

Analog to the carboxyl group [105], I expect hydroxyl groups to be able to form hydrogen bonds towards the substrate. Indeed, 1,3,5-Trihydroxybenzene forms substrate-templated patterns on calcite. As visible in Fig. 4.8 two island types can be distinguished. Drift-corrected, high-resolution images reveal a quasi-hexagonal pattern mirrored along the $[4\bar{2}.1]$ direction. Even if no naive adsorption model is found, the existence of two domains mirrored at the glide symmetry axis proves substrate-templating.

Consequently, both, molecules substituted with either carboxyl or hydroxyl groups are found to form substrate-templated structures on calcite indicating that both groups can provide specific molecule-substrate interaction with the calcite substrate.

5 Decisive Influence of Substitution Positions

Contents

5.1 Introduction	54
5.2 Results	56
Structures formed by DHBA isomers with high deprotonation tendency	56
Structures formed by DHBA isomers with low deprotonation tendency	58
5.3 Discussion	61
5.4 Conclusions	64

In this chapter¹, I present a systematic investigation of the constitutional isomers of dihydroxybenzoic acid on calcite (10.4) thereby revealing the impact of the substitution positions on the structural variety in molecular self-assembly on insulating surfaces. Six isomers of dihydroxybenzoic acid exist and they form six different molecular structures on the surface. Surprisingly, only two isomers arrange into stable, ordered structures at sub-monolayer coverage.

I discuss how the positions of the functional groups steer the molecular self-assembly of dihydroxybenzoic acids in three distinct ways, namely by (a) affecting the deprotonation tendency of the acid group, which, in turn, determines the character of the molecule-substrate interaction, (b) influencing the intermolecular interaction as already indicated by greatly different bulk structures and (c) altering the molecule-substrate matching.

¹This chapter is based on publication [125].

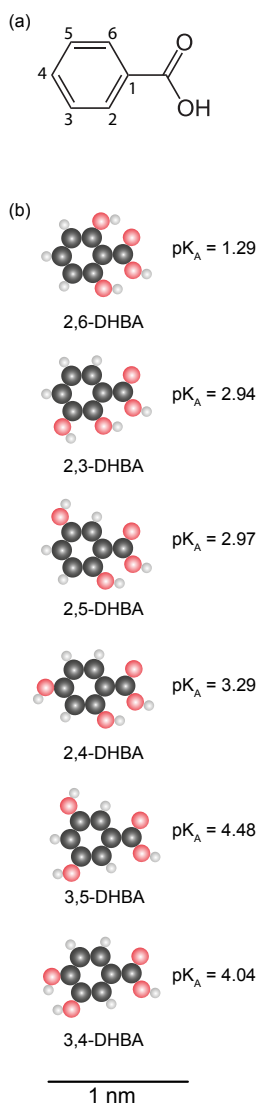


Figure 5.1: (a) Benzoic acid. (b) The constitutional isomers of DHBA ordered according to their pK_A values [126].

5.1 Introduction

In the following, I discuss the behavior of DHBA at room temperature on the calcite (10.4) surface at sub-monolayer coverage. Six constitutional isomers of DHBA exist, which differ by the positions of the hydroxyl groups at the benzene core (see Fig. 5.1). Due to the different arrangement of the functional groups, the molecules differ in their chemical behavior. For example, the tendency to deprotonate is enhanced when positioning the hydroxyl groups close to the carboxyl group. This difference in the deprotonation tendency of the carboxyl group is expressed by the pK_A values (see Fig. 5.1). The pK_A values of the isomers reflect the distance of the hydroxyl groups to the carboxyl group. In the 2,6-DHBA molecule, both hydroxyl groups are located directly next to the carboxyl group resulting in a high deprotonation tendency ($pK_A = 1.29$). In the 3,4-DHBA molecule, the hydroxyl groups are located farthest away from the carboxyl group resulting in a low deprotonation tendency ($pK_A = 4.48$).

In a recent study of 2,5-DHBA, it has been shown that deprotonation of this isomer occurs on the calcite surface, slowly enough to be followed with the nc-AFM at room temperature [57]. Spectroscopic evidence of the protonation state is difficult as most spectroscopy methods are not applicable at low molecular coverage on a bulk insulator. Although, the pK_A value is a measure for the deprotonation tendency of a molecule in aqueous solution, it provides a reliably quantity for comparing the deprotonation tendency of carboxylic acids on the same surface. Indeed, carboxylic acids with lower pK_A values than 2,5-DHBA were found to be already deprotonated on the surface, while acids with higher pK_A values were found to be protonated ([91] and supplementary information therein). Consequently, I expect DHBA isomers with a lower pK_A value than 2,5-DHBA to tend to deprotonation as well, while DHBA isomers with a higher pK_A value are expected to remain protonated. The above consideration is a simplified picture ignoring, e.g., effects of the surface on the deprotonation process. Nevertheless, it allows for categorizing the isomers: deprotonated and protonated isomers form two groups with distinctly different molecule-substrate interactions. The interaction of protonated DHBAs with the calcite surface is

likely to be dominated by hydrogen bonds between the molecules and the surface carbonate groups [105]. For deprotonated molecules, on the other hand, the molecule-substrate interaction is expected to be governed by electrostatic interaction between the carboxylate group and the surface calcium ions [57].

Intermolecular interactions between DHBA molecules decisively influence the formation of ordered patterns on the calcite surface. The bulk structure of a molecule gives a first indication of the dominant intermolecular interactions. In the bulk, all DHBAs remain protonated. Thus, the bulk structures of these molecules are dominated by hydrogen bonds. The common hydrogen bonding motif for two carboxylic acid molecules is the formation of a centrosymmetric carboxylic acid dimer [127]. For benzoic acid (Fig. 5.1 (a)), the bond energy of such a dimer in vacuum has been calculated to 0.74 eV [128]. In a crystal of benzoic acid, dimers arrange into rows, which form a herringbone pattern via π - π interaction. Similar arrangements are found in the bulk structures of DHBA isomers [129–133]. Depending on the position of the hydroxyl groups, the dimer rows can additionally interact through hydrogen bonds. For most DHBA isomers, several polymorphs of similar energy exist, which differ in their hydrogen bond motif. The polymorphs of 3,5-DHBA do not exhibit the common arrangement into dimer rows, but show a large variety of other hydrogen bond motifs, e.g., hydrogen bonds between the carboxyl group and the hydroxyl groups [133]. This finding suggests that functional groups in position 3 and 5 offer a greater variety of favorable intermolecular bond motifs besides the simple formation of carboxylic acid dimers.

When comparing isomers of the same protonation state, the strength of the molecule-substrate interaction is expected to be similar. However, the ability to form ordered structures depends crucially on the match between surface lattice and molecular arrangement which is governed by the intermolecular interactions. Consequently, the substitution positions of the functional groups are decisive for a stable substrate-templated pattern.

In the following, I briefly describe the structural arrangement of DHBA isomers at sub-monolayer coverage on calcite (10.4). I find the individual molecules of each isomer to be mobile at

room temperature on the calcite surface. Consequently, it depends on the strength and the balance of intermolecular and molecule-surface interactions whether stable structures form. In the next part of this section, I describe those molecules, which are prone to deprotonation, i.e., 2,5-DHBA, 2,3-DHBA and 2,6-DHBA. Thereafter, the arrangements of the presumably protonated molecules, namely 2,4-DHBA, 3,5-DHBA and 3,4-DHBA, are described. These descriptions will be followed by a detailed analysis in the discussion section.

5.2 Results

Structures formed by DHBA isomers with high deprotonation tendency

The adsorption of 2,5-DHBA has been studied before and two ordered phases have been identified [57]. The molecules in the striped phase are protonated forming a hydrogen-bonded network, which resembles the bulk structure. Deprotonated 2,5-DHBA molecules form the densely packed phase which consists of commensurate (1×5) islands. Directly after deposition, both phases are observed (Fig. 5.2 (a)). Over time, the molecules in the protonated, striped islands deprotonate and the amount of striped phase decreases. The deprotonated molecules attach to the densely-packed islands and these islands grow, indicating the mobility of the deprotonated molecules at room temperature. Eventually, only densely-packed islands in (1×5) arrangement remain (Fig. 5.2(b)). Thus, the previously hydrogen-bonded network formed by protonated 2,5-DHBA molecules transforms into an electrostatically stabilized structure formed by the deprotonated species.

For 2,3-DHBA, a similar phase transition is observed namely the transformation of metastable stripes into stable but unordered clusters (Fig. 5.2 (c)). Directly after deposition, stripes are seen on the calcite surface which arrange along the $[4\bar{2}.1]$ direction. These stripes are presumably molecular double rows and exhibit a periodicity of 0.8 nm in $[\bar{4}2.1]$ direction, commensurate to the

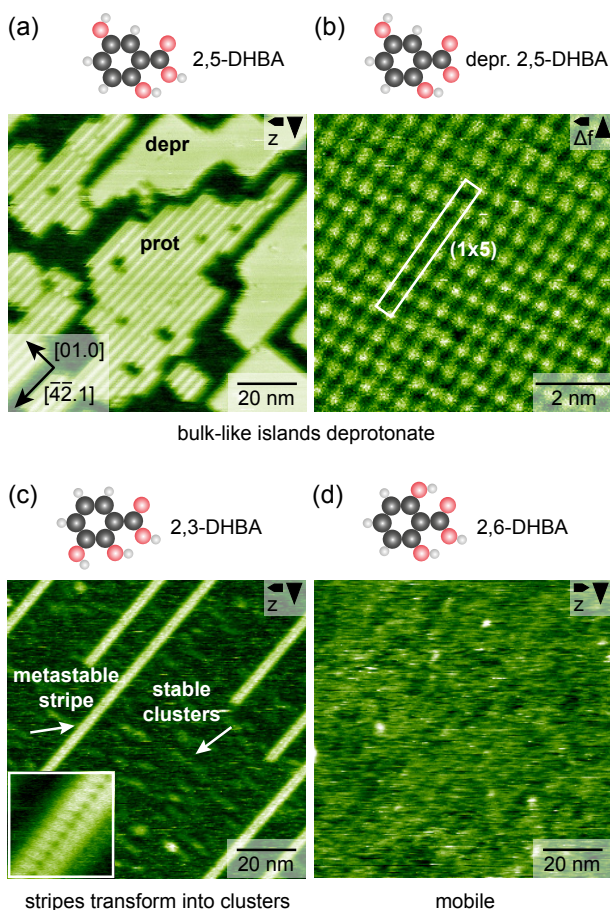


Figure 5.2: Overview of all isomers prone to deprotonation after submonolayer deposition onto the natural cleavage plane of calcite held at room temperature. nc-AFM image of (a) 2,5-DHBA, showing both phases: striped, metastable islands that transform into densely-packed, deprotonated islands over time and (b) a dense island of deprotonated 2,5-DHBA. (c) 2,3-DHBA forms metastable stripes (see inset, 7.1 nm \times 7.1 nm), which transform into stable clusters over time. (d) nc-AFM image of 2,6-DHBA revealing mobile molecules. The images in subfigures (a) and (b) were recorded by Markus Kittelmann.

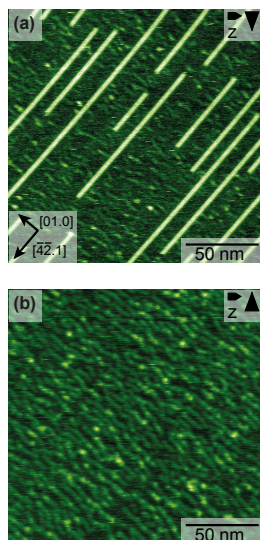


Figure 5.3: 2,3-DHBA over time. (a) Assembly 2 days after deposition. (b) Assembly after slight annealing.

surface structure (see inset of Fig. 5.2 (c)). Besides the stripes, mobile molecules and loosely arranged clusters are visible. Over time, the stripes vanish and the molecules rearrange into clusters, which are elongated along the [01.0] direction. Upon heating the sample, this phase transition is accelerated. Fig. 5.2 (c) shows the arrangement two days after sublimation, exhibiting stripes as well as elongated clusters. Depending on the coverage, the complete transition from stripes to clusters happens on a time scale of several hours to many days. The pK_A values of 2,5-DHBA and 2,3-DHBA are quite similar and both molecules show a phase transition. Thus, it is suggestive to ascribe the phase transitions of 2,3-DHBA to deprotonation analogous to the case of 2,5-DHBA. Consequently, I assign the metastable stripe structure formed after deposition to a hydrogen-bonded network of protonated 2,3-DHBA molecules, while the stable cluster phase is assigned to the deprotonated species.

Images of 2,6-DHBA reveal predominantly mobile molecules that are visible as streaks in the fast scan direction in Fig. 5.2 (d). In few experiments, some additional stripe-like structures along the [01.0] direction are noted. The high tendency for deprotonation of 2,6-DHBA reflected in its low pK_A value of 1.29 provides a strong indication that this molecule exists only as deprotonated species on the calcite surface. I assign the mobile species in Fig. 5.2 (d) to deprotonated 2,6-DHBA.

Structures formed by DHBA isomers with low deprotonation tendency

Now I take a closer look at the DHBA isomers with a smaller deprotonation tendency as compared to 2,5-DHBA. At submonolayer coverage of 2,4-DHBA, only mobile molecules are seen in the nc-AFM images (Fig. 5.4 (a)) visible as streaks in the fast scan direction. No phase transition into an ordered, substrate-templated structure is observed, even after the sample was heated to facilitate diffusion and deprotonation processes. Since no phase transition is observed and the deprotonation tendency of 2,4-DHBA is lower as compared to 2,5-DHBA we assign the mobile species in Fig. 5.4 (a) to protonated 2,4-DHBA.

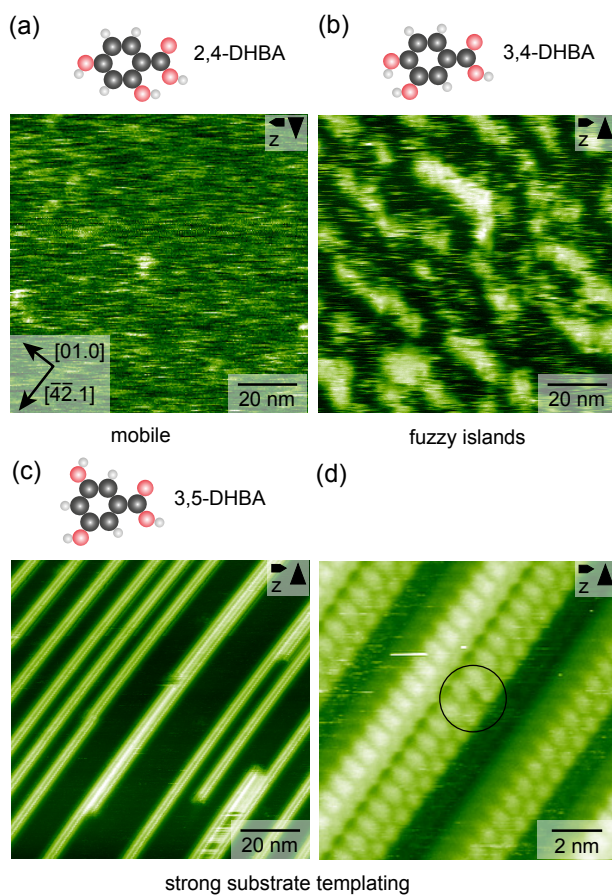


Figure 5.4: Overview of all isomers expected to remain protonated after submonolayer deposition onto the natural cleavage plane of calcite held at room temperature. (a) Overview nc-AFM image of 2,4-DHBA revealing mobile molecules. (b) Overview nc-AFM image of 3,4-DHBA revealing fuzzy islands. (c) Overview NC-AFM image of 3,5-DHBA which forms stable, ordered stripes. (d) Drift-corrected, high-resolution nc-AFM image of these double stripes. A defect is visible in the center of the image.

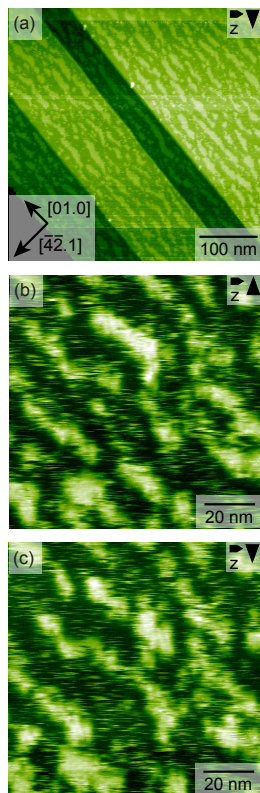


Figure 5.5: 3,4-DHBA on calcite. (a) Overview image. (b) and (c) Subsequent images revealing the mobility of the molecules in the islands.

The isomer with the smallest deprotonation tendency, 3,4-DHBA, forms islands which appear elongated along the $[01.0]$ direction (Fig. 5.4 (b)). The fuzzy outline of these islands and the additional mobile species in between indicate a significant mobility of the molecule even when arranged in islands. Moreover, the islands change their shape between consecutive NC-AFM images and they are easily manipulated with the AFM tip, further indicating weak intermolecular interaction within the islands. Therefore, the internal order within an island could not be resolved. As in the case of 2,4-DHBA, no phase transition is observed even after the sample was heated. Consequently, we assign the fuzzy islands in Fig. 5.4 (b) to be composed of protonated 3,4-DHBA.

The symmetric isomer with the two hydroxyl groups in position 3 and 5 shows a stable substrate-templated pattern on calcite: 3,5-DHBA arranges into stripes along the $[\overline{4}2.1]$ direction of the calcite surface (Fig. 3c). The stripes are typically 100 nm to 500 nm long. At low coverage, mostly individual stripes are observed. The stripes constitute molecular double rows. Drift-corrected [75], high-resolution images as shown in Fig. 5.4 (d) reveal the molecules within the stripe are arranged in a zigzag pattern with a periodicity of 0.8 nm in $[\overline{4}2.1]$ direction. The defect marked in the center of Fig. 5.4 (d) is caused by two missing 3,5-DHBA molecules, supporting the above-made assumption that each stripe consists of a molecular double row. The low apparent height of 0.2 nm and the strong directionality of the stripes, suggest a hydrogen-bonded network of flat-lying molecules. The stripes are stable even after annealing the sample to temperatures as high as 500 K.² Above this temperature the molecules start to desorb from the surface. Since no phase transition is observed and the strongly directional ordering suggest hydrogen bonds, I assign the molecules in the double rows to protonated 3,5-DHBA.³

²Temperatures are not measured directly at the sample but close to the heating stage. The temperature of the sample during annealing is estimated using a calibration curve provided by the AFM manufacturer.

³Further information to 3,5-DHBA can be found in Chapter 6.

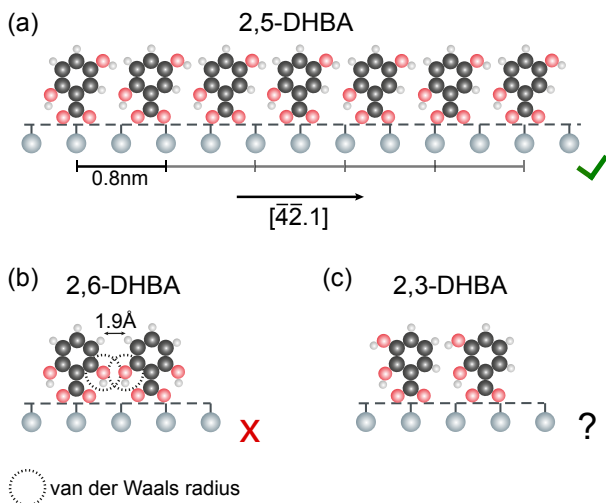


Figure 5.6: (a) Model of the densely-packed phase of deprotonated 2,5-DHBA according to [57]. The same arrangement is prohibited for (b) 2,6-DHBA, but not impossible for (c) 2,3-DHBA.

5.3 Discussion

In the following, I discuss the structural arrangements of the DHBA isomers in view of the positions of the functional groups. The preceding description of the experimental results surprisingly revealed that only two isomers of DHBA form stable, well-ordered structures at sub-monolayer coverage on the calcite surface: deprotonated 2,5-DHBA molecules form a (1×5) superstructure and protonated 3,5-DHBA molecules arrange into commensurate double rows. Due to their different deprotonation state, these two isomers serve as reference in my discussion since they represent the two fundamental possibilities for the molecule-substrate interaction between DHBA and calcite.

First, I compare the patterns formed by 2,6-DHBA and 2,3-DHBA with the (1×5) superstructure of deprotonated 2,5-DHBA, which has been proposed earlier [57]. In this model, the carboxylate ions adsorb on top of the calcium cation rows along the $[42.1]$ direction due to electrostatic attraction. The comparatively small

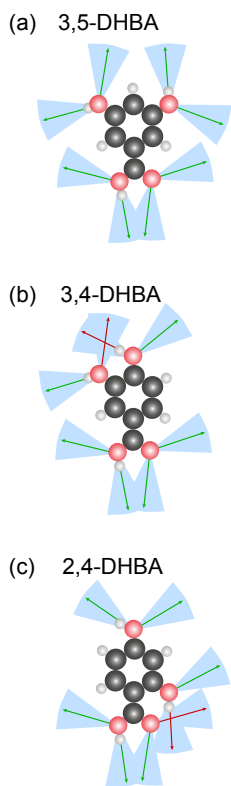


Figure 5.7: Sketches of the three protonated DHBA isomers indicating all possibilities for hydrogen bonds: blue cones indicate the preferred orientation of such a bond, green arrows show hydrogen bond opportunities with other molecules or the substrate, red arrows mark hydrogen bond opportunities that block each other.

lateral repeating units do only allow for an upright-standing or tilted fashion of the molecules. Such a tilted arrangement matches the observed apparent height of 0.4 nm. Along the same direction, neighboring 2,5-DHBA molecules align most likely via hydrogen bonds formed by the hydroxyl groups (Fig. 5.6 (a)). Since the molecule-substrate interaction is dominated by the attraction between the carboxylate group and the calcium ions, it is plausible to assume that the positions of the hydroxyl groups effect the intermolecular interaction. The formation of the same ordered structure is prohibited in the case of 2,6-DHBA due to steric hindrance between the hydroxyl groups (Fig. 5.6 (b)): in the configuration sketched in Fig. 5.6 (b) the van-der-Waals radii of the neighboring hydroxyl groups (1.52 Å [134]) overlap widely and the distance between the oxygen atoms is shorter than the bonding length of a strong hydrogen bond. Thus, it can be readily understood that deprotonated 2,6-DHBA cannot arrange into the same commensurate (1×5) pattern as 2,5-DHBA. For 2,3-DHBA, such a simple argument is not found (Fig. 5.6 (c)). The flat clusters (apparent height smaller than 0.2 nm) formed by this isomer and the mobile species in between indicate weak molecule-molecule interaction. Even though a commensurate arrangement comparable to 2,5-DHBA is not prohibited like in the case of 2,6-DHBA, the hydroxyl groups at position 2 and 3 apparently fail to stabilize an ordered structure sufficiently to prevail at room temperature. Comparing the three DHBA isomers the decisive influence of the position of each single functional group (in this case the hydroxyl group in position 3, 5 or 6) on the structural arrangement becomes very obvious.

In the case of protonated DHBA isomers, I expect both intermolecular and molecule-substrate interactions to be governed by hydrogen bonds. Since hydrogen bonds have a strong angular dependence [99], not only the distance of interacting partners but also the geometrical arrangement and, specifically, the angle between interacting functional groups is important for the formation of an ordered structure. The experiments show that only 3,5-DHBA forms stable, well-ordered structures, namely substrate-templated molecular double rows. Due to the vast number of possible combinations for hydrogen bonds between the multiple functional groups of the molecules and the calcite surface, identifying the correct structure for the 3,5-DHBA stripes

is not trivial. With the same argument there is no naive approach that explains why 2,4-DHBA and 3,4-DHBA do not form stable, ordered structures. However, considering the directionality of the possible hydrogen bonds I find a simple argument why the symmetric isomer is a more promising candidate for molecular self-assembly than the other two DHBA isomers. Fig. 5.7 shows all eight hydrogen bond opportunities for each of the three protonated isomers. Blue cones indicate the preferred direction range ($\pm 20^\circ$ [99]) for each hydrogen bond opportunity. Obviously, the even arrangement of the functional groups around the benzene ring in 3,5-DHBA allows for the formation of the maximum number of hydrogen bonds towards neighboring molecules or the substrate. In the case of the two other isomers, two hydrogen bond opportunities are pairwise blocking each other. Neighboring functional groups disturb the formation of intermolecular and molecule-substrate hydrogen bonds along the directions indicated by red arrows in Fig. 5.7 (b) and (c). Since a possible candidate for hydrogen bonding would be close to both functional groups a bond towards one of the groups is only formed if the interaction with the neighboring group is not strongly repulsive. Moreover, in the case of the hydroxyl group at position two, the formation of an intramolecular hydrogen bond with the carboxyl group is likely (Fig. 5.7 (c)). Altogether, in the cases of 3,4-DHBA and 2,4-DHBA it is possible if not likely that two out of eight hydrogen bond opportunities are not accessible for intermolecular and molecule-substrate interaction and, thereby, cannot contribute to stabilize an ordered structure.

This interpretation is corroborated by a comparison of 3,4-DHBA with 3-hydroxybenzoic acid (3-HBA), i.e., 3,4-DHBA without the hydroxyl group at position 4. Experiments with 3-HBA (Fig. 5.8 (a)) reveal this molecule forms stable stripes on the calcite surface comparable to 3,5-DHBA. In contrast, 3,4-DHBA forms only fuzzy islands. Thus, removing one functional group (the hydroxyl in position 4) appears to restore the full potential of the remaining functional groups for forming intermolecular and molecule-substrate bonds. Further experiments show 4-HBA does not form a stable structure at submonolayer coverage (Fig. 5.8 (b)) although the functional groups are not blocking each other in this molecule. This finding clearly demonstrates the importance of the position of each individual group within the

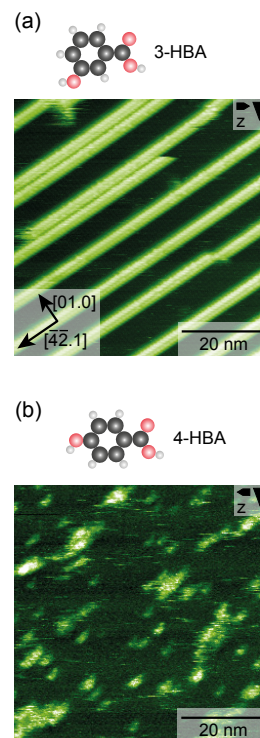


Figure 5.8: nc-AFM images of (a) 3-HBA and (b) 4-HBA at submonolayer coverage on calcite forming stable, substrate-templated stripes and no stable structure, respectively.

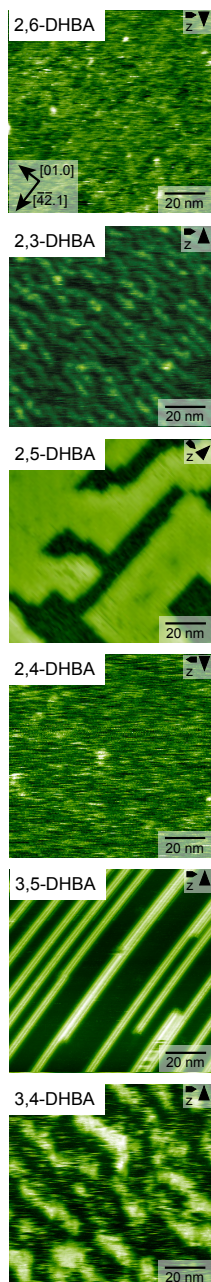


Figure 5.9: Summary of the long-term structures of the six DHBA isomers.

molecule on its self-assembly properties.⁴ The rather different self-assembly behavior of the DHBA isomers is summarized in Tab. 5.1 and in Fig. 5.9 shows the stable structures of all the isomers.⁵ Besides summarizing the observed behavior the table gives an overview about possible contributions to molecule-molecule and molecule-substrate interactions as discussed above.

5.4 Conclusions

In this chapter, I have demonstrated how a rather subtle change in the arrangement of functional groups results in a great variety of molecular structures. Dihydroxybenzoic acids on calcite (10.4) form very different structures depending on the position of the two hydroxyl groups. Among the six DHBA isomers, only 2,5-DHBA and 3,5-DHBA form stable, ordered structures on calcite at room temperature. I have discussed how the positions of the hydroxyl groups steer molecular self-assembly in three distinct aspects, namely the deprotonation tendency of the DHBA molecule, the intermolecular interactions and the molecule-surface matching. Positioning the hydroxyl groups close to the carboxyl group favors deprotonation and, thereby, influences the type of molecule-substrate interaction. The distribution of the hydroxyl groups around the benzene core determines how many opportunities for intermolecular interactions are available. The specific position of each functional group is crucial for the match with the calcite surface. In summary, positioning functional groups in a rational manner provides an option for tuning molecular self-assembly over a wide range from mobile molecules and metastable patterns to strongly substrate-templated, stable structures.

⁴I expect 3-hydroxybenzoic acid and 4-hydroxybenzoic acid to be protonated on the calcite surface, since their pK_A values [134] are 4.08 and 4.57, respectively.

⁵A summary of the structures of all molecules discussed in this thesis can be found in the appendix, including a graph which emphasizes the influence of the substitution positions.

Isomer	Observed structure	MM	MS	Assumed protonation state
2,6-DHBA	Mobile	-	ES	Deprotonated at RT
2,3-DHBA	Double-rows to clusters	HB network	ES	Transition from protonated to deprotonated at RT
2,5-DHBA	Striped islands to dense islands	HB network HB and π - π	ES	
2,4-DHBA	Mobile			Protonated at RT
3,5-DHBA	Double-rows	HB network		
3,4-DHBA	Fuzzy islands			

Table 5.1: Summary of the self-assembly of DHBA isomers on calcite. MM: molecule-molecule interaction. MS: molecule-substrate interaction. HB: hydrogen bond. ES: Electrostatic interaction.

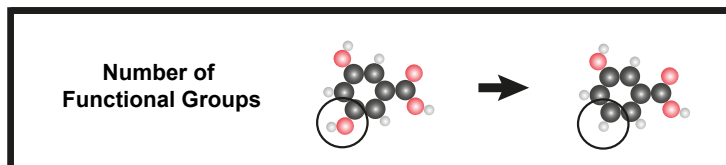
6 Long-Range Influence of a Hydroxyl Group

Contents

6.1 Introduction	68
Stripe-like Assemblies on Metal Substrates	69
6.2 Observation: Stripe-like Assembly	71
Adsorption Within the Stripes	71
Distribution of the Stripes	74
Mobility	81
6.3 Discussion	86
Interplay between Distribution and Mobility	86
Electrostatic Influences	90
6.4 Conclusions	94

In this Chapter, I report on the molecular self-assembly of 3,5-DHBA and 3-HBA on calcite (10.4). Both molecules arrange into long stripes along the $[4\bar{2}.1]$ direction with a (4×1) superstructure at a coverage of one monolayer. Mesoscopic ordering and mobility of the two molecular structures, however, differ significantly. Without changing the adsorption geometry of the individual molecules within the stripes, removing one hydroxyl group increases the mobility and induces a striking long-range order of the stripes.

Figure 6.1: Molecules studied within this chapter: 3,5-DHBA and 3-HBA.



6.1 Introduction

The self-assembly of DHBA on calcite is based on a delicate balance of intermolecular and molecule-substrate interactions (see Chap. 5). Thereby, the positions of the hydroxyl groups determine the geometry of the resulting arrangement. Another possibility to tune the self-assembly is changing the number of interacting functional groups. When providing attractive interaction, increasing the number of functional groups is expected to stabilize the arrangement, decreasing the number should destabilize it. This trend was confirmed for the carboxyl group: While terephthalic acid forms molecular chains in the fundamental bulk motif, the interaction with the surface is enhanced for trimesic acid, as trimesic acid arranges into a well-ordered flower motif unlike any bulk structure [7]. However, as the substitution positions of the carboxyl groups are not the same for the two molecules, the enhanced interaction is due to an interplay of the change in the number of functional groups and the change in the substitution positions.

Here, I present a study which demonstrates the influence of removing one of two symmetric functional groups by neither changing the geometry of the molecule nor the one of the resulting structure: 3,5-DHBA as well as 3-HBA arrange into extended molecular stripes on calcite (10.4) along the $[4\bar{2}.1]$ direction. I will demonstrate that reducing the number of hydroxyl groups does not influence the adsorption geometry of 3-HBA, but lowers binding energy and diffusion barrier or intermolecular interaction, resulting in highly mobile stripes of the same structure. Strikingly, the difference in the two molecules also induces a mesoscopic ordering of the stripes. Previously unobserved on a bulk insulator, 3-HBA stripes arrange with equidistant stripe spacing tunable by the molecular coverage.

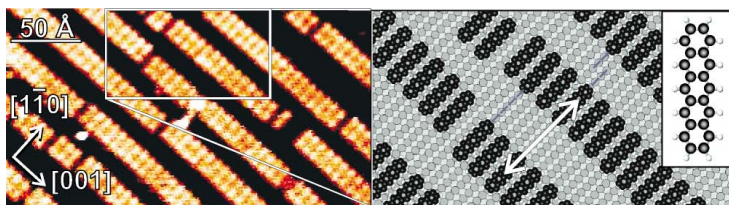


Figure 6.2: STM image of pentacene on Cu(110) showing molecular stripes with long-range ordering (after annealing to 400 K) due to so-called substrate-mediated repulsion. Adapted from [135].

Stripe-like Assemblies on Metal Substrates

The combination of surface characteristics and the geometry of the molecular building block can lead to stripe-like molecular assemblies on surfaces. Equidistant arrangements of stripes have been found on Cu(110) [135], on Ag(111) [136, 137] and on HOPG [138].

One monolayer of pentacene self-assembles on Cu(110) into one molecule wide stripes [135]. By annealing, a long-range order is established composed of extended, unidirectional rows with spacing between the rows (Figure 6.2). The spacing is not due to the weak intermolecular interaction of pentacene, but is attributed to the formation of charge-density waves in the surface state in the presence of the pentacene rows. Induced by the adsorbates, the adsorption energy exhibits an oscillatory modulation, named substrate-mediated repulsion.

Similar results are found on Ag(111), which also exhibits a surface state: 4-[trans-2-(pyrid-4-yl-vinyl)]benzoic acid forms hydrogen bonded rows with a mesoscopic ordering [137] (Figure 6.3). Also L-methionine forms an equidistant arrangement on Ag(111) [136]. In this case, however, the distance between the zwitterionic stripes depends on the coverage and can be tuned by the coverage (Figure 6.4). Without further investigation the authors assume that the mesoscopic ordering is mediated by the surface electronic structure of Ag(111). Also on HOPG in ambient conditions, L-methionine arranges into such equidistant stripes with coverage-dependent distance [138].

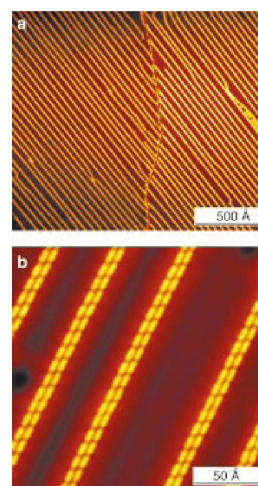
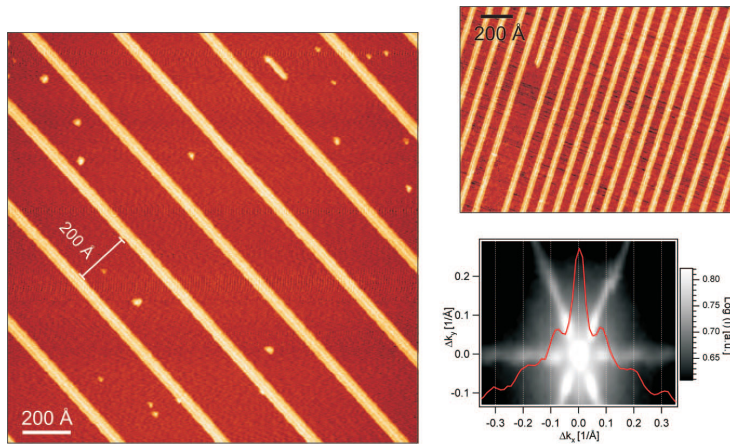


Figure 6.3: STM images of 4-[trans-2-(pyrid-4-yl-vinyl)]benzoic acid self-assembled on Ag(111) at 300 K (measured at 77 K). Adapted from [137].

Figure 6.4: Self-assembly of L-methionine on Ag(111). At intermediate coverage the distance of the rows is tunable by the coverage. STM images at (a) 0.15 ML and (b) 0.38 ML coverage. (c) Helium atom scattering at 0.6 ML coverage. Adapted from [136].



In summary, equidistant stripe arrangements have been found on metals which exhibit a surface state. A thorough investigation of the origin is not available in those cases, in which the stripe distance can be tuned by the coverage.

6.2 Observation: Stripe-like Assembly

In the following, I describe the arrangement of 3,5-DHBA and 3-HBA, which were deposited on the calcite (10.4) surface held at room temperature. I directly compare the two arrangements to emphasize similarities and differences.

Adsorption Within the Stripes

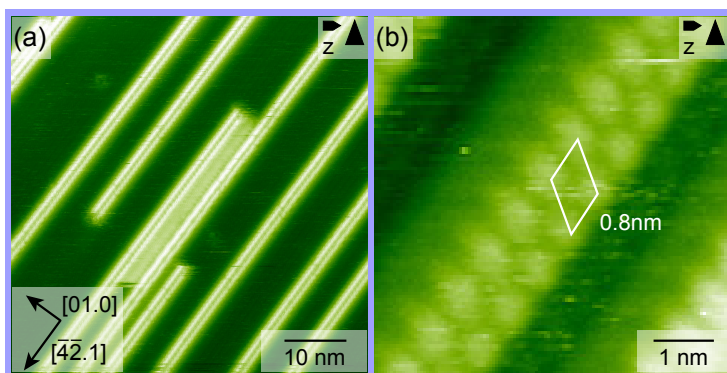


Figure 6.5: 3,5-DHBA: (a) AFM topography showing self-assembly into long stripes along the $[\overline{42}.1]$ direction. (b) Drift-corrected topography image of a single stripe consisting of a double row in zigzag arrangement.

A submonolayer of 3,5-DHBA on calcite (10.4) arranges into stripes, which run along the $[\overline{42}.1]$ direction (Fig. 6.5 (a)). At low coverage, mostly individual stripes are observed, which consist of molecular double rows. Drift-corrected, high-resolution images (Fig. 6.5 (b)) reveal a zigzag arrangement of the two molecular rows in each stripe with a periodicity of 0.8 nm along the $[\overline{42}.1]$ direction commensurate to the substrate. In the center of Fig. 6.5 (a) the area between two stripes appears fuzzy, which I attribute to mobile molecules trapped between the stripes.

The same arrangement is found for 3-HBA: A submonolayer of 3-HBA arranges into stripes running along the $[\overline{42}.1]$ direction (Fig. 6.6 (a)). The stripes consist of molecular double rows and detailed, drift-corrected images show a zigzag-like arrangement with a periodicity of 0.8 nm (Fig. 6.6 (b)).

Figure 6.6: 3-HBA: a) AFM frequency shift image showing self-assembly into long stripes along the $[4\bar{2}.1]$ direction. (b) Drift-corrected frequency shift image of a single stripe consisting of a double row in zigzag arrangement.

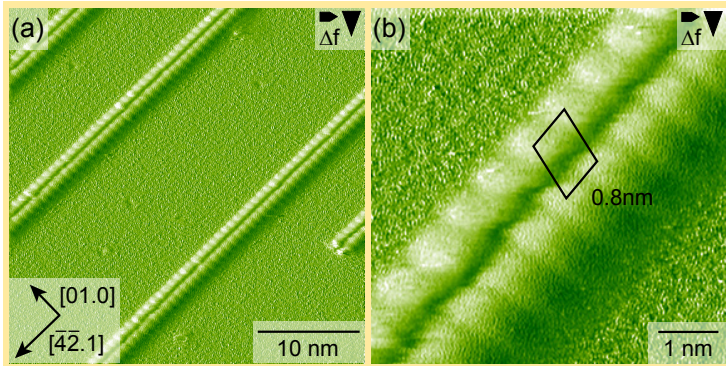
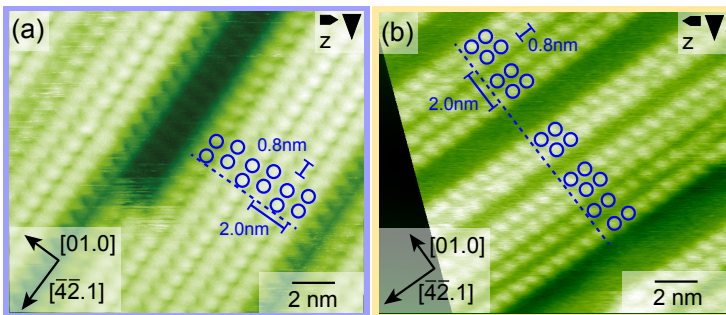
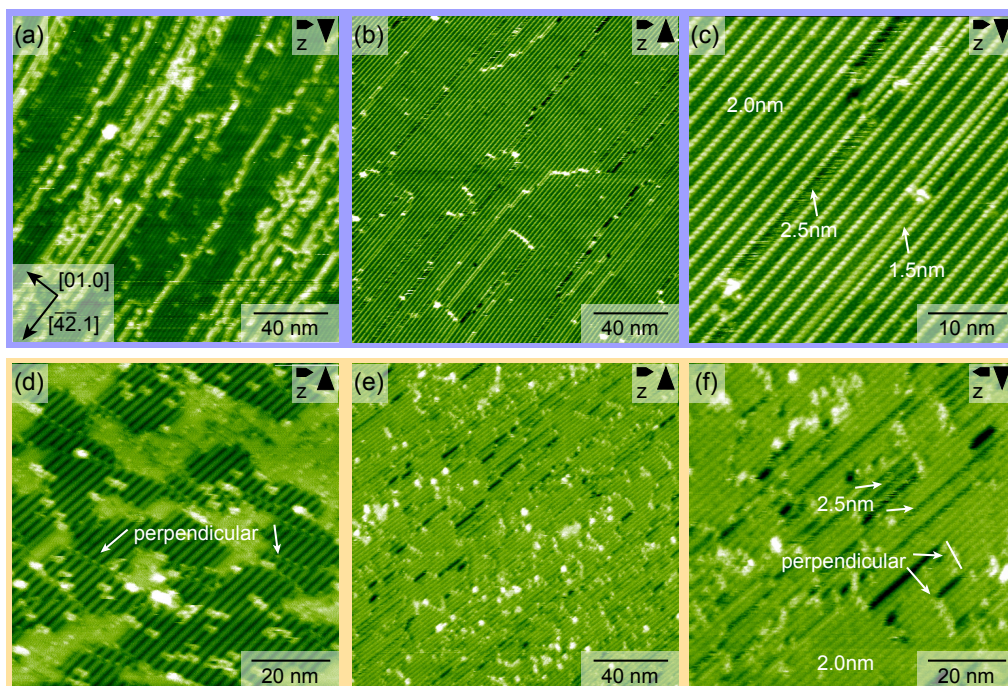


Fig. 6.7 shows the adsorption pattern of the two molecules at higher coverage for (a) 3,5-DHBA and (b) 3-HBA. To illustrate the pattern, circles highlight some protrusions in both images: The two protrusions in each stripe show a zigzag arrangement. Neighboring stripes run parallel without any shift and with a center-center distance of 2 nm, forming locally a (4×1) superstructure. Due to the surface glide symmetry, adsorption positions of neighboring stripes are the same either if the stripes are not shifted or if the stripes are mirrored and additionally shifted by half a unit cell. In all high-coverage images with sufficient resolution, no shift was observed.

Figure 6.7: Displacement of the stripes with respect to each other. Drift-corrected images at coverages above 0.5 ML for (a) 3,5-DHBA and (b) 3-HBA. Both molecules show a zigzag arrangement of the protrusions within one stripe. Neighboring stripes run parallel and have a center-center distance of 2 nm resulting in a (4×1) superstructure.



To summarize, both molecules show the same pattern in nc-AFM images, although the molecules differ by the number of their hydroxyl groups.



One Monolayer Coverage

At a coverage of one monolayer both molecules form a layer of stripes with a (4×1) superstructure.

First, I compare the pattern at a coverage slightly above one monolayer as shown in Fig. 6.8 (a) and (d) for 3,5-DHBA and 3-HBA, respectively. In both cases, the first layer is composed of stripes along $[\overline{42}.1]$ with a distance of 2.0 nm. In the case of 3,5-DHBA, molecules in the second layer adsorb along the $[\overline{42}.1]$ direction, while in the case of 3-HBA they adsorb as fuzzy regions elongated along the $[01.0]$ direction.

After annealing, 3,5-DHBA molecules in the second layer desorbed revealing domains of nicely ordered stripes with domain boundaries along the $[\overline{42}.1]$ direction (Fig. 6.8 (b) and (c)). The domain boundaries exhibit stripe distances of 2.5 nm or 1.5 nm. In conclude, second layer molecules adsorbed on such domain boundaries.

Figure 6.8: One monolayer coverage. 3,5-DHBA: (a) coverage > 1 ML. (b) and (c) after annealing. 3-HBA: (d) coverage > 1 ML. (e) and (f) coverage about 1 ML, no annealing. Both molecules form a layer of stripes with a (4×1) superstructure. For 3,5-DHBA, domain boundaries are mainly realized by stripe distances of 2.5 nm and 1.5 nm. For 3-HBA, additional perpendicular domain boundaries occur. (c) and (f) are corrected for linear drift.

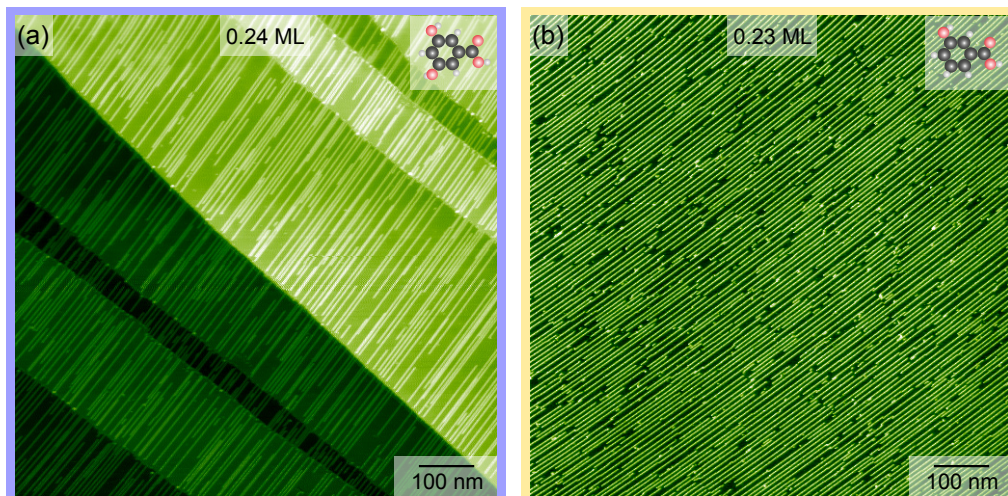


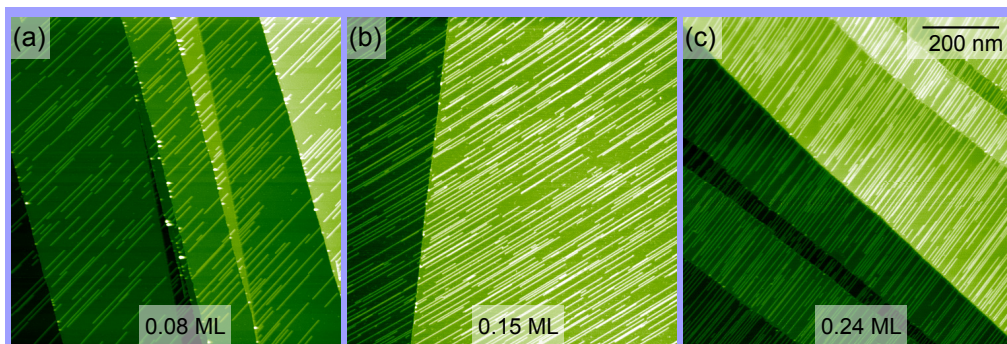
Figure 6.9: Stripe distribution of (a) 3,5-DHBA and (b) 3-HBA at similar coverage.

Annealing did not result in desorption of second-layer 3-HBA molecules (not shown, as comparable to Fig. 6.8 (d)). Instead, Fig. 6.8 (e) and (f) present a sample with a coverage of about one monolayer of 3-HBA, which was not annealed. Overall, the appearance of the 3-HBA islands is less ordered with many defects compared to 3,5-DHBA, which might be related to the missing annealing step. Besides their smaller size, the typical shape of the 3-HBA domains differs. The domains are not primarily oriented along the $[4\bar{2}.1]$ direction, but perpendicular domain boundaries exist as well. Quite intuitively, the different domain boundaries can explain the different adsorption of the second-layer molecules.

While both molecules form a (4×1) superstructure at one monolayer coverage, the difference in the shape of the domains, *i.e.*, in the type of the domain boundaries, hints at a small difference in the interaction or the microscopic packing.

Distribution of the Stripes

According to the previous paragraphs the adsorption pattern of the two molecules is the same. There is, however, a striking difference between mesoscopic images of similar coverage: While



3,5-DHBA stripes arrange randomly, 3-HBA stripes show a long-range mesoscopic order, namely, they arrange with equidistant spacing.

Fig. 6.9 (a) shows a $1\ \mu\text{m}$ wide sample area with about $1/4\ \text{ML}$ 3,5-DHBA. Extended stripes cover the calcite terraces. Most stripes run along the whole terrace, *i.e.*, they are about $300\ \text{nm}$ long. As stripes are observed to start and end in the middle of a calcite terrace, the step edge is not necessarily needed as nucleation seed. Typical stripe length range from $50\ \text{nm}$ to $400\ \text{nm}$. In some areas stripes are close to each other and even direct neighbors, other areas are without stripes, so that their distances range from the the minimum distance of $2\ \text{nm}$ for neighboring stripes to $50\ \text{nm}$ and more.

A surface area of the same size with a similar amount of 3-HBA molecules reveals a completely different behavior (Fig. 6.9 (b)): The whole surface area is uniformly covered by stripes. All stripes seem to have similar distances. Only tiny areas without stripes exist, when one stripe ends and the next one has not started yet. Furthermore, no neighboring stripes exist: Whenever two stripes meet, one of the stripes ends, instead of the two stripes continuing next to each other. In images with and without step edges, the lengths of the stripes typically ranges from $50\ \text{nm}$ to $300\ \text{nm}$.

While there is no hint for any long-range interaction of 3,5-DHBA stripes, 3-HBA stripes show a surprising long-range ordering. The similar distances of the stripes at this coverage points at an

Figure 6.10: 3,5-DHBA: Stripe distribution at different coverages. The scalebar applies to all subfigures.

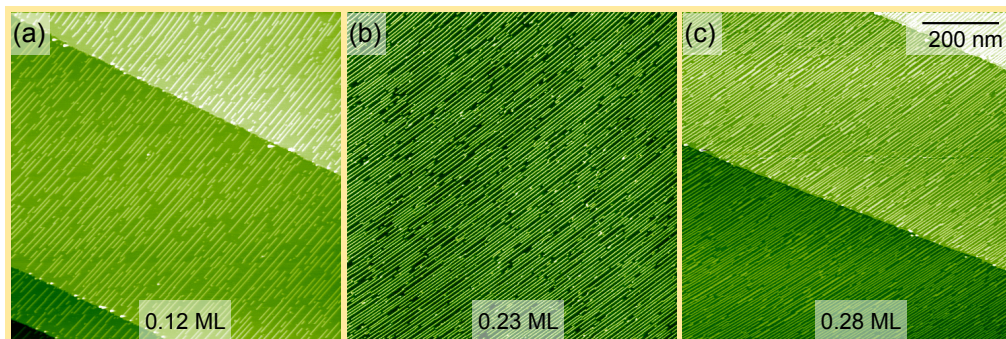


Figure 6.11: 3-HBA: Stripe distribution at different coverages. The scalebar applies to all subfigures.

equidistant arrangement. If such an arrangement is not due to a specific characteristic of the substrate, the stripe distance should depend on the coverage. To understand the behavior of this ordering samples were prepared with different molecular coverages ranging from about 1/10 ML to 1 ML of both molecules.

Fig. 6.10 illustrates the distribution of 3,5-DHBA stripes at coverages up to 1/4 ML. Data for higher coverage is included in the following analysis, but no images are shown here because at higher density of stripes no individual stripes can be distinguished in images of this scale. At all coverages areas without stripes and areas with higher density of stripes exist confirming the random distribution. Besides, all samples show long stripes. In contrast, all samples with 3-HBA (Fig. 6.11) seem to be uniformly covered by stripes, no large areas without stripes exist. Indeed, the distance between stripes is larger at lower coverage and smaller at higher coverage. Only at a coverage of 0.28 ML (and higher), neighboring stripes can be observed. Samples with lower molecular coverage do not exhibit neighboring stripes. Obviously, the stripe distance can be tuned by adjusting the coverage. As if there was a long-range repulsion, the molecular stripes arrange as far from each other as possible. Besides, the 3-HBA stripes appear to be a little shorter than the 3,5-DHBA stripes.

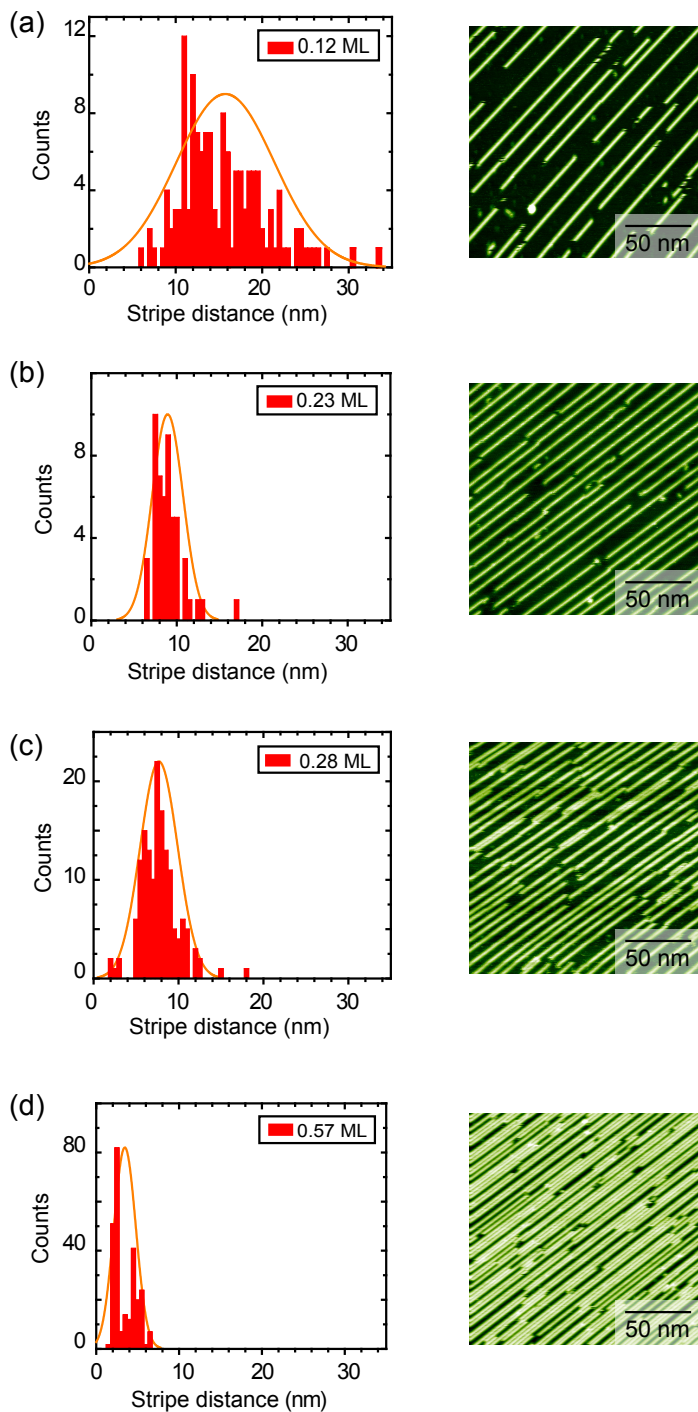
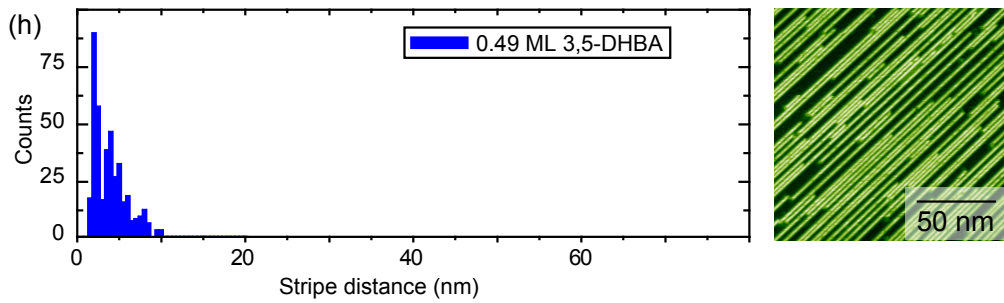
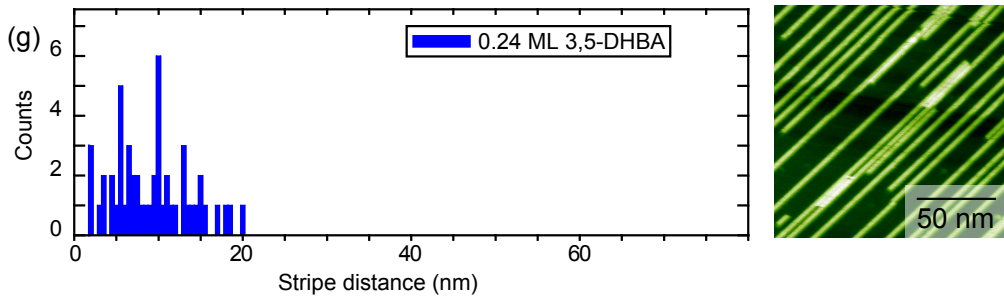
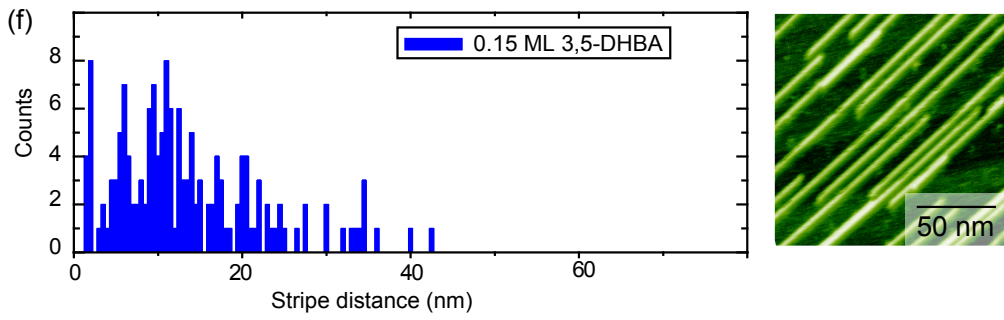
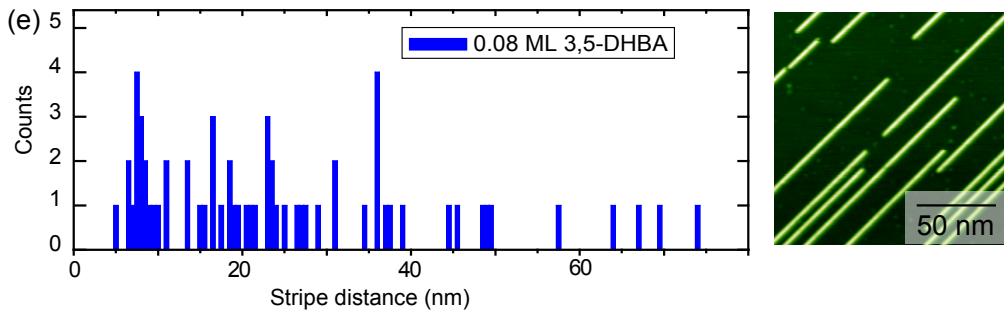


Figure 6.12: Histograms and exemplary AFM images at different coverages for (a)-(d) 3-HBA and (e)-(h) 3,5-DHBA.

6 Long-Range Influence of a Hydroxyl Group



Histograms

The qualitative observation of the distinctly different stripe distributions is complemented by a statistical analysis in this section. The center-to-center distances of the stripes were obtained by analyzing 200 nm (≈ 174 nm after calibration) wide images. The coverage was estimated by the average number of stripes, which cross the image border of an image of such width.¹ To take the finite stripe length into account and to gain reasonable statistics also for low coverage, stripe distances were measured along three lines in each image, namely along the diagonal and additionally along a diagonal line in the two quadrants without previous measurement. In total, over 600 stripe distances were analyzed for each molecule. For each coverage, the distances are summarized in a histogram with bin size 0.5 nm. This bin size corresponds to the size of the calcite unit cell along the [01.0] direction, *i.e.*, perpendicular to the commensurate stripes. For each histogram either up or down images were considered to minimize drift effects.

The histograms for 3-HBA are shown in Fig. 6.12 (a)-(d). Next to each histogram an exemplary image for the same coverage is shown. All histograms show pronounced maxima around one stripe distance, which decreases with increasing coverage. At low coverage, no neighboring stripes, *i.e.*, distance 2 nm, occur. The histogram at 0.57 ML coverage (Fig. 6.12 (d)) shows not only one peak at 2 nm/2.5 nm but a second, less pronounced maximum at 4.5 nm. This effect is attributed to the finite length of the stripes and easily illustrated by a simple picture: Let us assume there is an area with three stripes with distances of 2 nm and 2.5 nm. If the stripe in the middle ends, a distance of 4.5 nm occurs.

Histograms and exemplary images for 3,5-DHBA are shown in Fig. 6.12 (e)-(g). Here, a wide distribution of stripe distances is observed at all coverages, *e.g.*, in Fig. 6.12 (f) ranging from the minimum distance of 2 nm for neighboring stripes to distances of up to 40 nm. Even at quite low coverage neighboring stripes oc-

¹Due to this estimation, the coverage of low coverage samples of 3,5-DHBA exhibits a systematic error; because the 200 nm wide scan areas were not randomly chosen but at the time of measurement images were acquired on areas with interesting features, *i.e.*, covered by many stripes. Thus, the estimated coverages are expected to be too large.

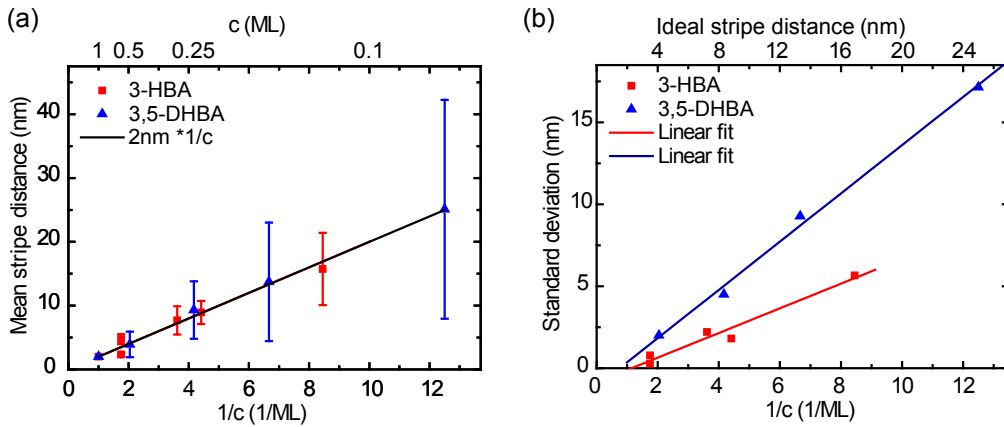


Figure 6.13: (a) Mean row distance vs. inverse coverage for 3-HBA (red squares) and 3,5-DHBA (blue triangles). The mean values of both distributions fit well with the linear behavior of an equidistant arrangement. (b) Standard deviation vs. inverse coverage for 3-HBA (red squares) and 3,5-DHBA (blue triangles). The deviation from an equidistant arrangement is more pronounced for 3,5-DHBA than for 3-HBA.

cur. Thus, in contrast to 3-HBA, these stripes show the random distribution of an assembly without long-range interaction.

For infinite stripe length and equidistant stripes the theoretical center-center distance d of two neighboring stripes is $d = 2\text{nm}/c$ with 2 nm being the minimum stripe distance (at one ML coverage) and c being the coverage in ML. Thus, plotting the mean stripe distance versus the inverse coverage should result in a linear behavior with the error bars indicating the deviation from the ideal behavior.

Fig. 6.13 (a) shows the experimental mean stripe distance plotted versus the inverse coverage for 3-HBA (red squares) and 3,5-DHBA (blue triangles). At high coverage of 3-HBA two data points are plotted for the two maxima discussed above. For both molecules, theoretical behavior (black line) matches the experimental values quite well, demonstrating that the coverage was determined correctly. The difference of the two molecular distributions is reflected by the error bars. Fig. 6.13 (b) shows the standard deviations of the distributions versus the coverage. For both molecules, the deviation increases linearly with increasing stripe distance. A clear difference of the slope is observed, which is about a factor of 2 smaller for 3-HBA.

Mobility

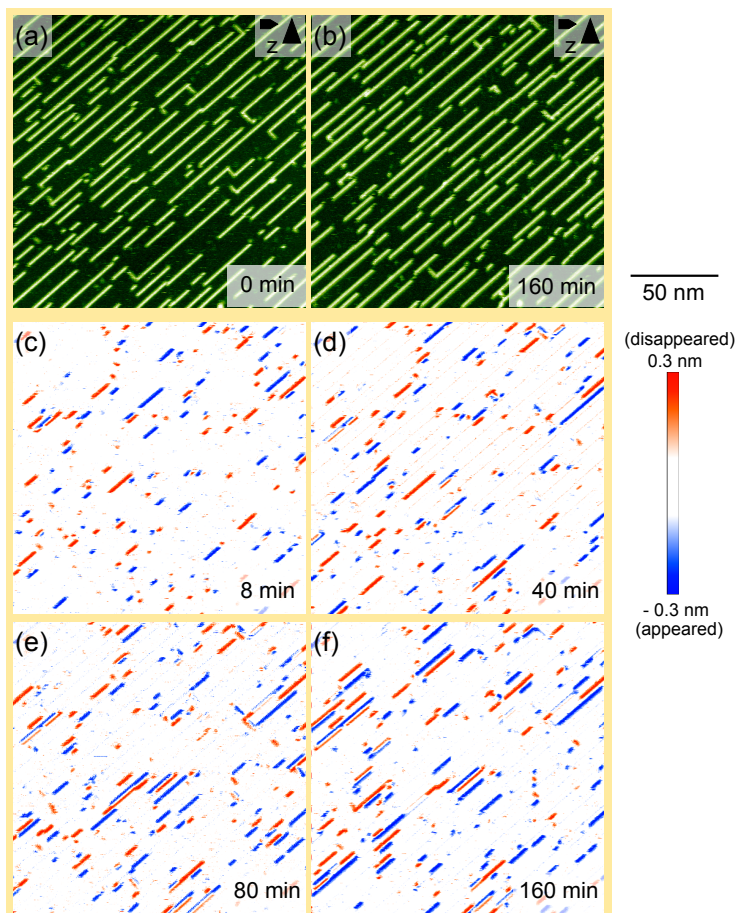
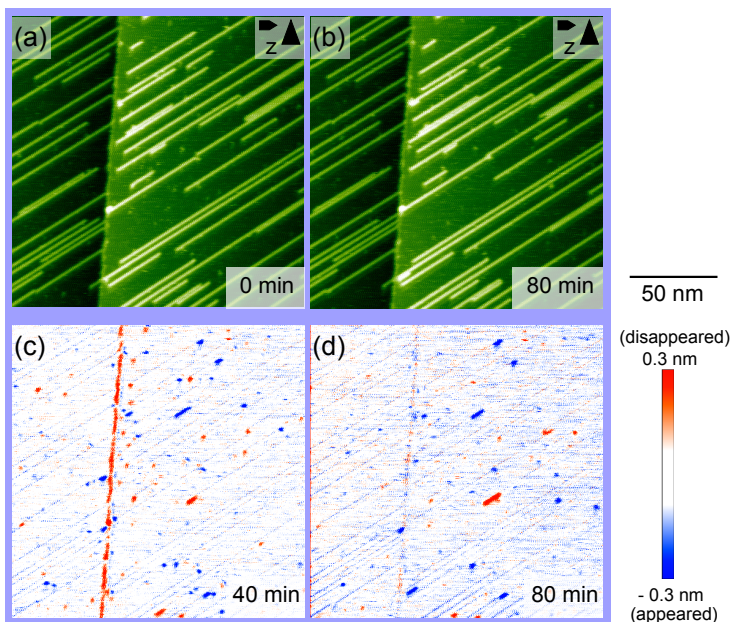


Figure 6.14: Analysis of 20 consecutive AFM images of 3-HBA. (a) First image. (b) Last image. (c) - (f) Difference images with increasing time intervals.

The second characteristic which differs significantly for the two molecules is the mobility of the stripes. For 3-HBA, consecutive scan images differ: the length of the stripes changes, (short) stripes disappear and reappear at a different position. To monitor these changes, consecutive images of the same area were acquired over 15 hours and assembled to a movie, which can be found on the attached CD. To minimize drift effects only images along the same scan direction are included. The movie is

Figure 6.15: Analysis of 10 consecutive AFM images of 3,5-DHBA. (a) First image. (b) Last image. (c) and (d) Difference images with different time intervals.



composed of 91 images with a time interval of about 9 min. No two images within the movie are completely alike, stripes change and even seem to jump when they change their length or their position. Thus, the sample area observed in the movie is dominated by changes and movement.

In comparison, consecutive images of 3,5-DHBA look nearly identical. The attached movie of 3,5-DHBA includes 89 images showing the temporal variations of the self-assembly of 3,5-DHBA. On this surface, only small variations at the edges of the stripes are observed.

To quantify the temporal variations visualized in the movies, images acquired at different times were subtracted. Prior to subtraction the images were slightly translated to compensate for drift. Fig. 6.14 shows a selection of such difference images for 3-HBA. The first and last image of the sequence analyzed here, are presented in Fig. 6.14 (a) and (b), respectively. Fig. 6.14 (c) to (f) show difference images with increasing time intervals. Red areas indicate stripes which disappeared, blue areas indicate stripes which appeared. For a time interval of 9 min, many short

stripes in both colors are visible (Fig. 6.14 (c)), *i.e.*, the length of stripes changed and short stripes disappeared. Within 45 min (Fig. 6.14 (d)), the number of changes increased. In the middle of the image more narrow blue and red lines are located directly next to each other. Here, a stripe disappeared and reappeared at a position translated by only a few unit cells in $[01.0]$ direction. The number and length of these neighboring lines increases in Fig. 6.14 (e) and (f), *i.e.*, more complete stripes rearranged. Quite obviously, a larger time separation between the subtracted images leads to a larger difference in the stripe distribution. Moreover, we learn that the stripes rearrange step-wise by changing their edges. Despite the large amount of movements, the qualitative order of the stripes stays the same. Apparently, stripes rearrange all the time without changing the overall order indicating that the distribution is in equilibrium.

A similar sequence for 3,5-DHBA is shown in Fig. 6.15. Only minor changes occur over time in terms of a few stripes changing their length. The changes of the arrangement of 3,5-DHBA after 90 min are still significantly smaller than the changes which occurred for 3-HBA in a time interval of 9 min. Obviously, the mobility of the two molecular structures differs significantly. Further, the diffusion process of the two molecules on calcite is visualized: For both molecules, changes always start at the ends of the stripes indicating that the weakest bond molecule is located at the end of a stripe.

The only difference between the two molecules is the additional hydroxyl group of 3,5-DHBA. This additional functional group does not change the adsorption pattern of the molecules within the stripes but obviously it alters the mobility of the molecular structure significantly. A straightforward explanation can be given by simply comparing the two molecules: If the hydroxyl at position five of 3,5-DHBA forms molecule-substrate bonds, the molecule-substrate interaction is lower for 3-HBA resulting in a lower diffusion barrier. On the other hand, if the hydroxyl at position five does not form a molecule-substrate bond, but an intermolecular bond, the intermolecular interaction is lower, so that the molecule can more easily detach from a stripe, which also results in a higher mobility.

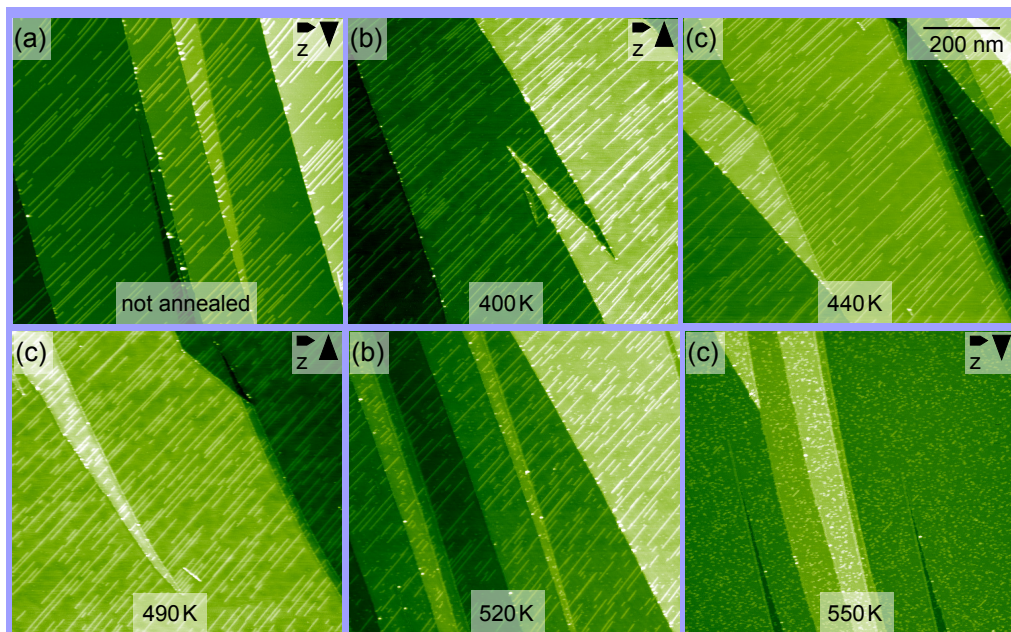


Figure 6.16: 3,5-DHBA. Overview AFM images of a step-wise annealed sample. The samples were annealed for the period of one hour.²

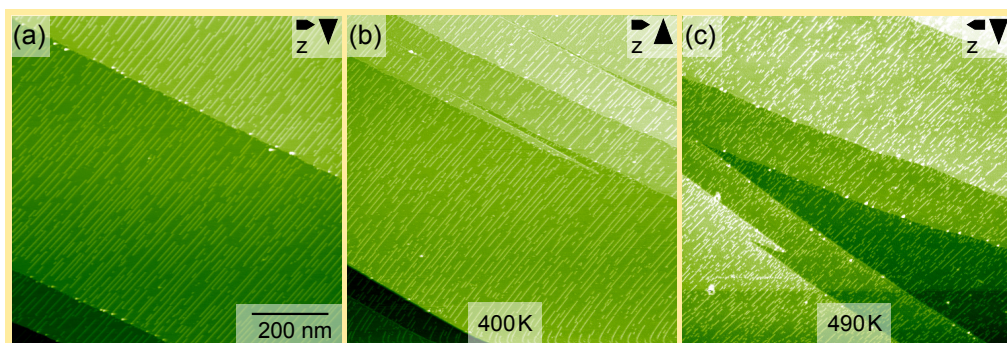
Comparison of the Binding Energies

Even if it is not possible to measure binding energies by AFM, I want to roughly compare the binding energies of the two molecules. For each molecule, a sample was step-wise annealed. After each annealing step, AFM images were acquired to observe any changes. By comparing the annealing temperatures needed for the desorption of the molecules the magnitude of the binding energies can be compared.

A sample with 3,5-DHBA was annealed to a range of temperatures for a period of one hour.² No obvious alterations are observed for annealing of up to 490 K (Fig. 6.16 (a) to (d)): The length of the stripes are still in the same range and all sam-

²Temperatures are measured using a thermocouple, which is not directly located at the sample holder. The given temperatures at the sample plate are estimated using a calibration curve provided by the AFM manufacturer. Besides the rough estimate, the temperature at the sample surface might further depend on the type of the sample holders or the thickness of the crystal.

ples show areas with higher density of stripes and areas with lower density of stripes. After annealing to 520 K (Fig. 6.16 (e)) the total density of stripes decreased and also many stripes are shorter. Still, the distribution of the stripes stays random. I conclude that the molecules started to desorb, preferably from the ends of the stripes. After annealing to 550 K, only small clusters remain on the surface.



An annealing sequence for 3-HBA is shown in Fig. 6.17. Here, first indications for desorption are already seen after annealing to 400 K. The length of the stripes decreases further after annealing to 440 K (not shown) and 490 K. After annealing to 510 K the stripes completely desorbed.

3-HBA desorbs at lower temperature than 3,5-DHBA indicating that 3-HBA has a lower binding energy to calcite than 3,5-DHBA. Thus, the additional hydroxyl group of 3,5-DHBA interacts attractively with the calcite substrate. As binding energy and diffusion barrier are related, it is plausible to assume that also the diffusion barrier of 3-HBA is lower than the one of 3,5-DHBA.

Figure 6.17: 3-HBA. Step-wise annealing for a period of one hour each. Annealing to 510 K lead to complete desorption of the stripes (not shown).

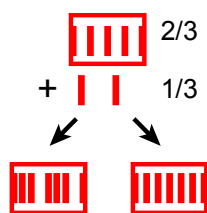


Figure 6.18: Idea of a test experiment for studying the diffusion of 3-HBA stripes. After sequential deposition of $2/3$ of a given quantity and afterward the remaining $1/3$, two possibilities for the arrangement exist: 1) The new molecules form stripes in between the previous stripes. 2) All molecules rearrange to form an equidistant arrangement with a distance according to the new coverage.

6.3 Discussion

In Section 6.2, I presented the self-assembly of 3,5-DHBA and 3-HBA. Even if the molecular adsorption pattern within the stripes is the same, two main characteristics differ: the distribution of the stripes and their mobility. The difference in mobility can be understood by the reduced number of bonding possibilities. Understanding the equidistant arrangement of the 3-HBA stripes, however, is not trivial. In this section, I first discuss the possibility of a kinetic growth mechanism. Afterward, an electrostatic origin of the stripe arrangement is discussed.

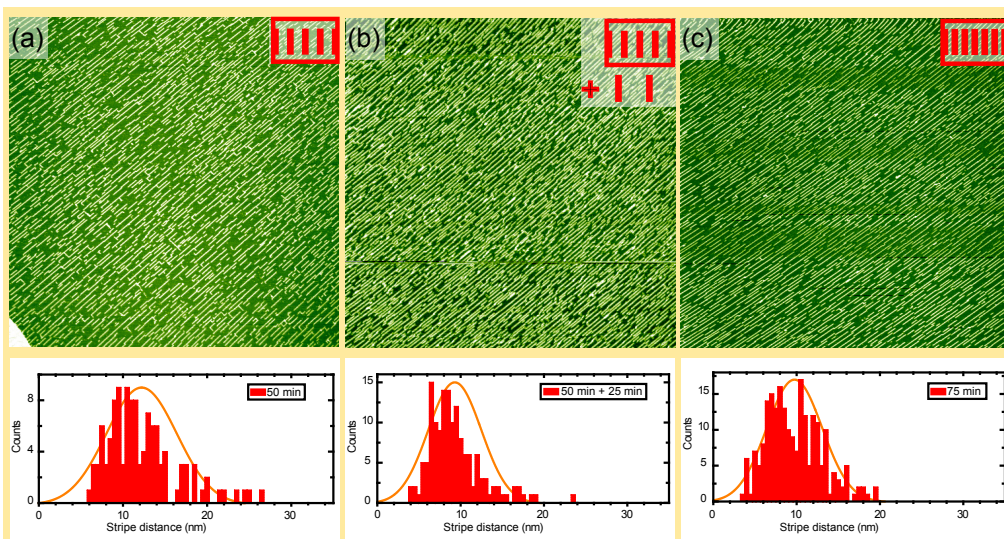
Interplay between Distribution and Mobility

As the two molecules are quite similar and their adsorption pattern is so alike, it is tempting to ask if there is an interplay between the two differing characteristics, *i.e.*, causes the increase in mobility the difference in the arrangement?

In the following, I further study the diffusion of the stripes to find out if the stripes occupy the equilibrium positions or if the arrangement is kinetically hindered. In a first experiment, I study the effect of sequential deposition of 3-HBA. Afterward I show 3,5-DHBA samples, which were annealed to enhance the diffusion.

Effect of sequential sublimation of 3-HBA

In this paragraph, I analyze the interplay between mobility and stripe arrangement. Firstly, I take a closer look at the diffusivity of the 3-HBA stripes by studying if the molecules can completely change their initial arrangement. The results will show whether the mobility is independent of the scanning process and, furthermore, whether the molecules occupy the equilibrium arrangement. The following test was performed (see sketch in Fig. 6.18): Two samples were prepared, the first one with a given quantity directly deposited via one sublimation step. Here, we expect an equidistant arrangement. On the second sample, in a



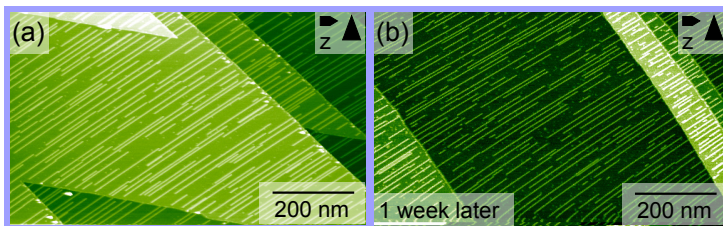
first step, a coverage of $2/3$ of this given quantity was deposited. Again, we expect an equidistant arrangement. In a second step, additionally, half of the previous amount was deposited. In total, the same amount of molecules is deposited as in the case of sample one, but now there are two possibilities for the molecular assembly:

1. The molecules are completely mobile and arrange equidistantly in the same way as on the first sample.
2. The previous arrangement stays the same and the additional molecules arrange in between. In this case, two distances should be observed: the one seen before and half of this distance.

The results of this experiment are summarized in Fig. 6.19. The coverage of $2/3$ of the chosen quantity (0.16 ML calculated from mean stripe distance) and the corresponding histogram (calculated from 118 stripe distances) in Fig. 6.19 (a) show an equidistant arrangement with a mean distance of $12.2 \text{ nm} \pm 4.2 \text{ nm}$. The distribution is broader than the one shown in Fig. 6.12, probably due to the reduced stripe length on this sample. With

Figure 6.19: Test experiment to study the diffusion of 3-HBA stripes. (a) nc-AFM image and histogram (118 stripe distances) for a coverage of 0.16 ML, resulting from 50 min deposition. (b) nc-AFM image and histogram (148 stripe distances) after additional deposition for 25 min, resulting in a coverage of 0.21 ML. (c) nc-AFM image and histogram (220 stripe distances) after direct deposition for 75 min, resulting in a coverage of 0.21 ML.

Figure 6.20: 3,5-DHBA. Stripe distribution (a) one day and (b) one week after preparation.



decreasing stripe length the number of domains increases and at domain boundaries the distance between stripes is not ideal. Additionally, a second species of stripes exists oriented perpendicular to the already known species. Both features are attributed to the density of defects, which is much higher on the current sample compared to previous ones. If there are more nucleation centers, shorter stripes and perpendicular stripes may be stable.

After deposition of additional molecules, resulting in a total coverage of 0.21 ML, the stripe distribution looks still equidistant with one maximum at $9.3 \text{ nm} \pm 3.2 \text{ nm}$ (Fig. 6.19 (b)). No second maximum at $9.3/2 \text{ nm} = 4.7 \text{ nm}$ is observed indicating that the stripes rearranged. A similar mean distance of $9.7 \text{ nm} \pm 3.3 \text{ nm}$ (and thus the same coverage of 0.21 ML) results from sublimation in one step (Fig. 6.19 (c)). Even if the distributions are not as well-pronounced as on previous samples, the equidistant arrangements around a similar mean distance suggest a rearrangement of all molecules after sequential deposition. The molecular flux in the experiment is low compared to the diffusivity of the molecules. I conclude that 3-HBA stripes are at their equilibrium positions and that the mobility is not induced by the scanning process.

Enhancing the Diffusion

Now I discuss the influence of enhancing the diffusion on the distribution of 3,5-DHBA stripes. In case of a kinetic growth mechanism this should result in an equidistant arrangement of 3,5-DHBA stripes as well. Time alone is not sufficient for altering the arrangement: Fig. 6.20 (a) and (b) show a sample

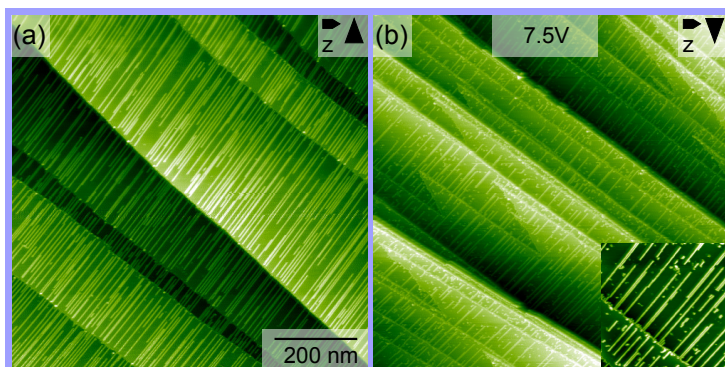


Figure 6.21: Effect of annealing on the stripe distribution of 3,5-DHBA. Topography before annealing (a) and after annealing to 510 K for 1 h. Some stripes vanished, or only short pieces remained. The inset ($200 \times \text{nm}^2$) shows remaining neighboring stripes.

one day and one week after deposition of 3,5-DHBA molecules, respectively. The only obvious change is that the sample looks significantly less clean after one week.

By annealing the diffusion can be enhanced. Fig. 6.21 shows a sample (a) *prior* to annealing and (b) after annealing to 510 K. Even if annealing resulted in a substantial reduction of the stripes, many neighboring stripes exist on the surface after annealing.³ Thus, the molecules either desorb before they reach their equilibrium arrangement or they already exhibit their equilibrium arrangement.

Another consideration might be the possible mechanism, how kinetics could change the growth between randomly distributed stripes and equidistant stripes on an unstructured surface. The kinetic growth of metal clusters on metal substrates is quite well understood [139, 140]. The cluster size depends on the temperature (and thereby the mobility), while the cluster distribution is random. In a similar picture, the stripe length could be explained by a different diffusion barrier: High diffusion barriers would lead to short stripes, small diffusion barriers to long stripes.

In summary, both experiments, the sequential deposition of 3-

³Compared to the annealing sequence in Fig. 6.16 lower temperatures were needed for the desorption of the molecules. The temperature at the sample surface strongly depends on the type of sample holder and the length of the crystal.

HBA and the annealing of 3,5-DHBA, do point at structures, which represent the thermal equilibrium structure. Consequently, a kinetic growth mechanism as sole origin of the mesoscopic order is unlikely.

Electrostatic Influences

KPFM Measurements

A quite obvious explanation for the equidistant arrangement of the 3-HBA stripes would be electrostatic repulsion. Electrostatic forces between the probe tip and surface structures can be measured by KPFM. On calcite, islands composed of deprotonated 2,5-DHBA show a significantly more negative contrast ($\Delta V = -1.75V$) than islands composed of protonated 2,5-DHBA ($\Delta V = -0.5V$) [57]. If the equidistant arrangement of the 3-HBA stripes was caused by electrostatic repulsion, pronounced KPFM contrast might be present for 3-HBA stripes but not for 3,5-DHBA stripes.

The KPFM contrast observed on 3-HBA samples is not very pronounced, but shows a similar magnitude as variations that also occur on bare calcite. To give an overview, I show the KPFM signal recorded before and after a tip change in Fig. 6.22. The KPFM signal in Fig. 6.22 (b) shows a slightly positive contrast on most of the stripes. Additional signal variations occur as well. In Fig. 6.22 (c)-(f) topographical features as well as corresponding KPFM features are better resolved, probably due to a tip change. Moreover, the KPFM features in the stripes appear dark, *i.e.*, negative. This difference in the sign of the signal might be due to an altered tip termination. The scanning tip is semiconducting and possibly covered by oxide, molecules and/or calcite. Especially when imaging at high setpoints it is likely to pick up mobile molecules. As the molecules have a dipole moment, the interaction with the sample depends on how the molecule is oriented on the tip apex. Electrostatic forces measured by nc-AFM are known to depend on the tip polarity [32, 141], thus, the different sign of the stripe contrast in subfigures (b) and (d) can be attributed to a different tip termination. Fig. 6.22 (e) and (f)

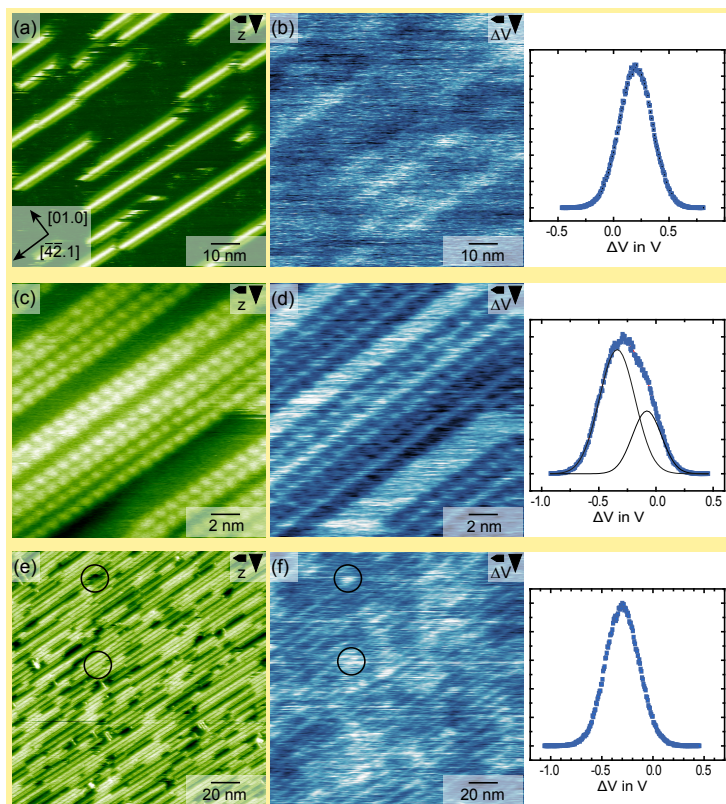
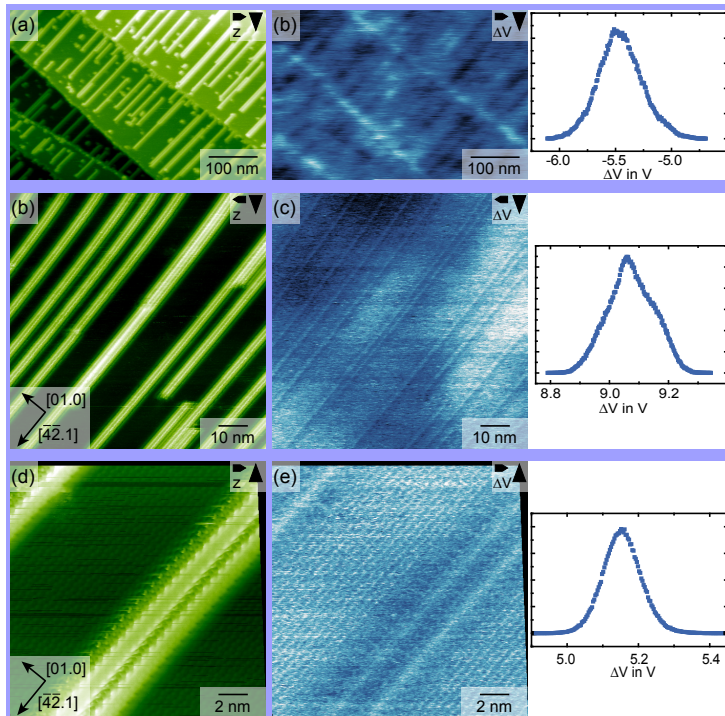


Figure 6.22: 3-HBA. (a) Topography and (b) corresponding KPFM image and tip voltage histogram showing slightly positive (bright) contrast of the stripes. (c) Topography and (b) corresponding KPFM image showing negative contrast on each protrusion. (e) Overview topography image and (f) corresponding KPFM image showing larger scale substrate variations of similar strength as the contrast observed for the stripes.

show a larger surface area. On this area, not only the stripes are visible in the KPFM signal, but additional spatial, unpronounced variations dominate the contrast. These variations are not related to the stripes. The areas marked in Fig. 6.22(e) and (f) appear bright in the KPFM signal, but in the topography signal one area is on molecular stripes, while the other area is on calcite. The origin of these variations is unknown. As similar variations were observed on bare calcite surfaces with defects, the variations are attributed to defects on the substrate.

The electrostatic contrast of the 3-HBA stripes is smaller than the variations caused by this defects on the substrate, indicating that it is unlikely that the arrangement of the stripes results solely from electrostatic repulsion of the molecular stripes. Furthermore, the weak contrast of 3-HBA in KPFM images com-

Figure 6.23: 3,5-DHBA. Topography and corresponding KPFM images for 3,5-DHBA. (a) and (b) Overview imaging showing KPFM contrast on step edges, defects and stripes. (c) and (d) KPFM signal is dominated by spatial variations. (e) and (f) At high setpoints KPFM contrast on calcite and stripes is observed.



pared to deprotonated 2,5-DHBA, suggests that the molecules remain protonated.

Fig. 6.23 shows KPFM measurements of 3,5-DHBA. With a given tip, calcite step edges and defects appear bright, 3,5-DHBA stripes dark. With another tip, the stripes are barely visible, but the image is dominated by similar variations as observed on the 3-HBA substrates. At high Δf setpoints, *i.e.*, close to the surface, more detailed KPFM contrast is visible on calcite and stripes. Unlike the case of 2,5-DHBA, in which every tip shows the same pronounced KPFM signal just in different quality, these observations point to weak electrostatic forces and, thus, to protonated molecules.

In summary, the KPFM measurements of both molecules, 3-HBA and 3,5-DHBA, are quite alike: The results depend strongly on the tip and signal variations, which are possibly due to defects on

calcite, dominate the contrast. There is no hint for a strong, long-range electrostatic repulsion of 3-HBA explaining an equidistant stripe arrangement with stripe distances up to 15 nm or more. On the other hand, an interaction without pronounced lateral variations might not be detectable by KPFM.

The strongest similarity with the arrangement of 3-HBA on calcite, is the arrangement of molecules on metals with a surface state (see Chap. 6.1). In these cases as well, the molecules did not show strong long-range intermolecular interactions. However, calcite is not known to exhibit a well-known surface state to mediate these weak interactions.

6.4 Conclusions

In summary, I presented the self-assembly of 3,5-DHBA and 3-HBA on calcite at room temperature. Both molecules form extended stripes along the $[\overline{42}.1]$ direction, with the same adsorption pattern in nc-AFM images. Due to the missing hydroxyl group at position five of 3-HBA, the binding energy is additionally, the mobility of the 3-HBA stripes is significantly enhanced compared to 3,5-DHBA. Moreover, a mesoscopic ordering is induced: 3-HBA stripes arrange equidistantly with coverage-dependent distance. Similar arrangements have been observed on metals which exhibit a surface state.

Removing one hydroxyl group, thus, changes (a) the mobility of the molecule and (b) introduces a mesoscopic ordering. The change in the mobility is straightforward to understand, as 3,5-DHBA can form an additional hydrogen bond towards the substrate. The uniform distribution of the 3-HBA stripes was analyzed in detail its origin, however, has not been fully understood yet.

To gain further insight into the different patterns formed by the two molecules, a cooperation with [Personal data removed] has been established. A detailed analysis of the adsorption patterns including electronic structure and diffusion barrier might elucidate the origin of the long-range order.

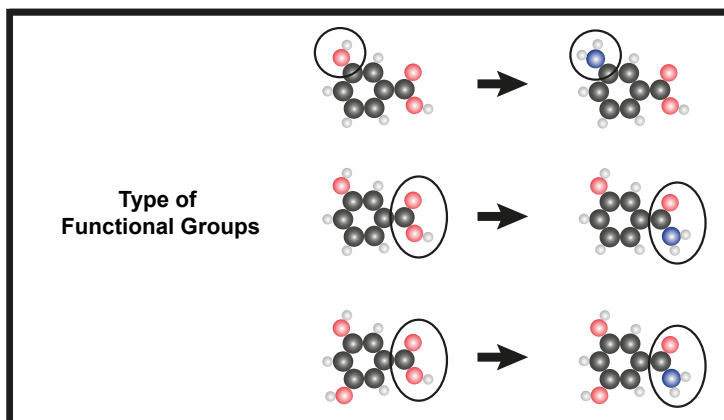
7 Influence of Different Hydrogen Bond Donors

Contents

7.1 Introduction	96
7.2 Amino vs. Hydroxyl Groups	98
3-ABA	98
Comparison to 3-HBA	102
7.3 Amide vs. Carboxyl Groups	103
3-HBA _{amide}	104
Comparison to 3-HBA	109
3,5-DHBA _{amide}	110
Comparison to 3,5-DHBA	116
7.4 Conclusions	118

In this chapter, I compare the assembly of molecules with only hydroxyl groups with the assembly of molecules, where one hydroxyl group was exchanged by an amino group. Both functional groups can serve as hydrogen bond donor towards calcite, but their bond characteristics differ. I observe how these differences result in a great variety of molecular structures. Depending on the environment of the functional group, varying between hydroxyl and amino groups can either result in a geometrically identical structure or can cause a transition from one-dimensional to two-dimensional growth.

Figure 7.1: Overview of studied molecules in this Chapter. First 3-HBA is compared to 3-ABA. Afterward 3-HBA is compared to 3-HBAamide and 3,5-DHBA to 3,5-DHBAamide.



7.1 Introduction

Dihydroxybenzoic acid holds three functionalities: the benzene core, the carboxyl group and the hydroxyl groups. All of them contribute to the self-assembly on calcite. The position of the hydroxyl groups influences the geometry of the self-assembled structure by altering the molecule-substrate match, the intermolecular interaction and also the protonation state (Chap. 5). The number of hydroxyl groups influences the mobility and can induce long-range order (Chap. 6). In this chapter, I study the influence of the characteristics of the hydrogen bonds, which are expected to be formed by carboxyl and hydroxyl groups.

Depending on their composition, hydrogen bonds can vary in strength over a wide range [99]. Among others, the bond strength depends on the strength of the hydrogen bond donor and the hydrogen bond acceptor (Chap. 3). The most well-known hydrogen bond donors are OH and NH_2 . Dihydroxybenzoic acid provides OH as hydrogen bond donor in two specific environments, either as substituent at the benzene core or as part of the carboxyl group. For hydrogen-bonded networks on calcite, the hydrogen bond acceptors of the surface are the oxygens of the carbonate groups.

Here, I study the influence on the self-assembly of exchanging

the OH donor by an NH donor for both substitution environments. In the first part, amino and hydroxyl substituted benzoic acids are compared. The example of 3-HBA and 3-Aminobenzoic acid (3-ABA) reveals that both hydrogen bond donors can be chosen to receive a hydrogen bonded network on calcite, since both groups result in the same arrangement of the molecules on calcite. In the second part the hydrogen bond donor as part of the acid group is studied. In this case, I observe a significant influence on the self-assembly. Both examples, 3-hydroxybenzamide (3-HBAmide) and 3,5-DHBAmide, show two-dimensional islands compared to the one-dimensional stripes of the corresponding acids.

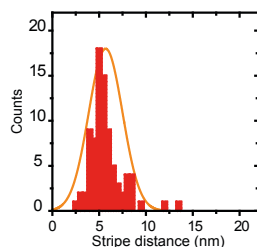


Figure 7.2: Histogram of the stripe distance of 3-ABA at the coverage shown in Fig. 7.3. The present coverage amounts to 0.35 ML based on a (4×1) superstructure at a full monolayer coverage. The distribution is well-described by a Gaussian with a mean distance of $5.7 \text{ nm} \pm 1.8 \text{ nm}$.

7.2 Amino vs. Hydroxyl Groups

Hydrogen bonds of the type O-H-O and O-H-N are typically quite strong with O-H-N bonds being in general slightly weaker due to the lower electronegativity of nitrogen compared to oxygen [99]. On calcite, the hydroxyl groups of 3,5-DHBA are expected¹ to form hydrogen bonds towards the substrate (Chap. 6). As amino-terephthalic acid [142] forms a more stable arrangement than terephthalic acid on calcite [7], I assume that also amino groups can build hydrogen bonds towards calcite. To compare the hydrogen bonds formed between calcite and either hydroxyl or amino groups, I analyze the self-assembly of 3-HBA and 3-ABA. Both molecules form stripes with the same adsorption pattern and the same long-range order, indicating a strong similarity of the hydrogen bonding possibilities. A slight difference might be indicated by the short length and high diffusivity of 3-ABA stripes at low coverage.

The present study, thus, contributes gaining precise control over molecular self-assembly on calcite by providing insight into two arrangements formed by molecules with slightly different hydrogen bonding characteristics.

3-ABA

Overview

A submonolayer of 3-ABA was deposited onto the freshly cleaved calcite (10.4) surface held at room temperature. The molecules arrange into stripes along the $[\bar{4}2.1]$ direction (Fig. 7.3) with a typical length of 20 nm to 60 nm. Drift-corrected, high-resolution images show a zigzag arrangement of molecular double rows with a periodicity of 0.8 nm along the $[\bar{4}2.1]$ direction (Fig. 7.3 (b)), like in the case of 3-HBA.

¹This is in line with preliminary DFT results.

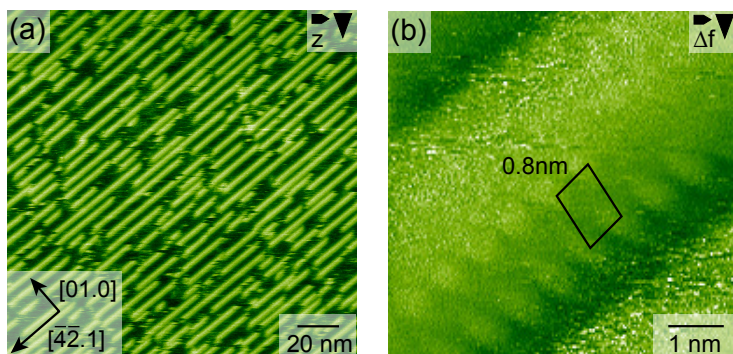


Figure 7.3: Self-assembly of 3-ABA on calcite. (a) AFM Topography showing equidistant stripes along the $[42.1]$ direction. (b) High-resolution, drift-corrected frequency shift image revealing a double row in zigzag arrangement with a periodicity of 0.8 nm along $[42.1]$. Due to a tip change, the molecular resolution is lost in the upper part of the image.

Long-Range Order

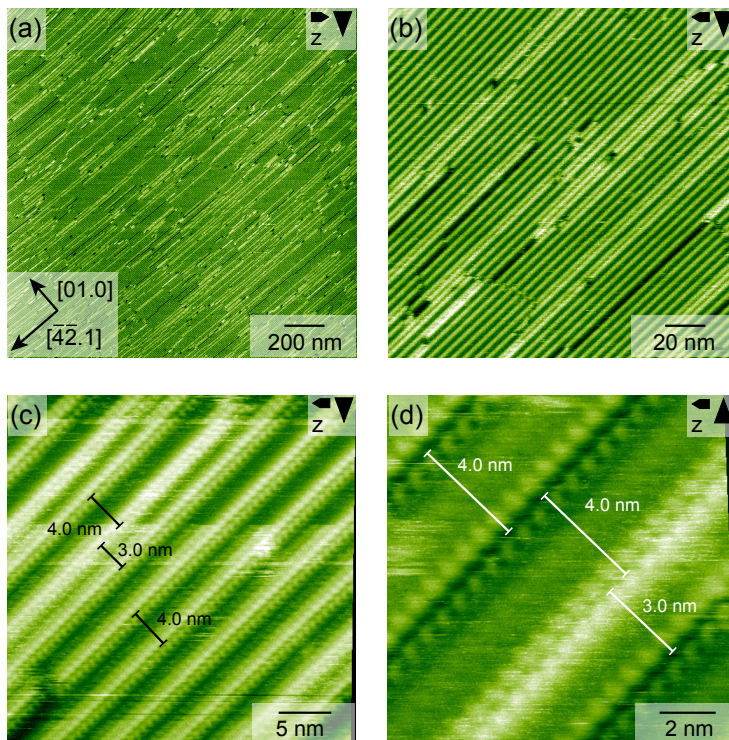
As for 3-HBA, also for 3-ABA a long-range order exists: The stripes exhibit an equidistant spacing. At this coverage, the stripe distances show a sharp distribution, which can be described by a Gaussian function, around the mean distance of $\bar{d} = 5.7 \text{ nm} \pm 1.8 \text{ nm}$ (Fig. 7.2).

At higher coverage, the equidistant arrangement becomes even more obvious. At the coverage shown in Fig. 7.4 extended domains form with stripe distances of 4 nm. At domain boundaries, smaller and larger stripe distances occur. If stripes have a smaller distance, one of the stripes appears brighter in the nc-AFM images (Fig. 7.4 (c) and (d)), which is attributed to the overlap of side features of the tip. The broadness of the tip becomes obvious for stripes with larger distances than 4.0 nm (see, e.g., bottom left corner of Fig. 7.4 (c)).

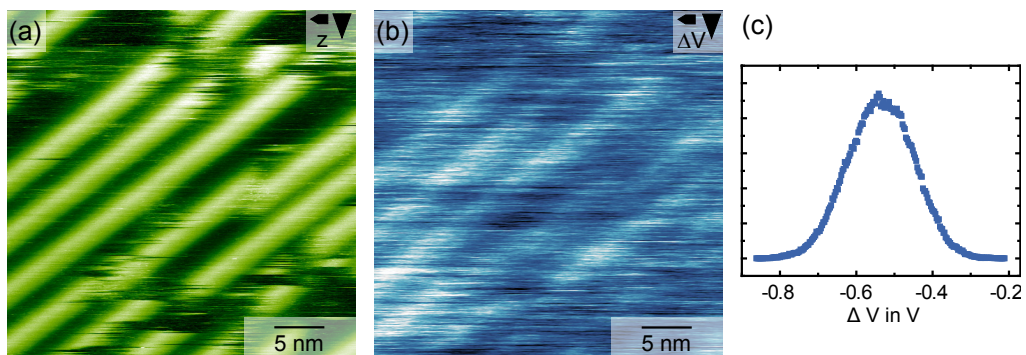
Based on a (4×1) superstructure at one monolayer coverage, the coverage in Fig. 7.4 amounts to about 0.5 ML .² In Chap. 6, Fig. 6.12 (d) and (h) show 3-HBA and 3,5-DHBA, respectively, at approximately half a monolayer coverage. While 3,5-DHBA shows a random distribution of the stripes with distances ranging from 2.0 nm to about 10 nm, the arrangements of 3-ABA and 3-HBA resemble strongly in their homogeneous appearance. In the case

²No higher coverages of 3-ABA were tested. Due to the similarity to 3-HBA and 3,5-DHBA, I consider the same superstructure for one monolayer coverage.

Figure 7.4: 3-ABA at higher coverage. The topographies show a homogeneous arrangement with extended domains of stripes of 4 nm distance. At domain boundaries, larger distances can occur as well as stripe distances of 2.5 nm and 3.0 nm. Assuming a minimum distance of 2 nm like in the case of 3-HBA, the coverage is about 0.5 ML.



of 3-HBA, stripes have either a distance of 4.0 nm and 4.5 nm or they are closer together showing distances of 2.5 nm and 2.0 nm. In the case of 3-ABA, the coverage is slightly lower and larger domains with stripe distances of 4.0 nm occur. In both cases no significantly larger distances are observed and the arrangement is such that the number of neighboring stripes is as low as possible. Concluding, 3-ABA shows the same long-range order as 3-HBA with equidistant stripe spacing. Like in the case of 3-HBA, this spacing is tunable by the coverage as evident from Figures 7.3 and 7.4.



Mobility

Another characteristic is the mobility of the stripes, which is quite evident: Many streaks are visible in the nc-AFM images. Furthermore, consecutive images differ, *i.e.*, the length of the stripes changes and short stripes vanish and reappear, revealing a high mobility of the stripes. The short stripe length and unstable scanning conditions at low coverage hint at a significant mobility of 3-ABA that might be even higher than the one of 3-HBA, but a definite prediction is difficult due to the influence of the tip.

Energies

Annealing experiments suggest the binding energy is in a similar range as the one of 3-HBA: No large changes occur up to annealing to 440 K. After annealing to 520 K the molecules had desorbed or arranged into immobile clusters. Furthermore, the high mobility of the stripes indicates a small diffusion barrier or a weak intermolecular interaction, which seem as well to be in a similar range as for 3-HBA.

Figure 7.5: KPFM measurements of 3-ABA. (a) Topography. (b) Corresponding KPFM image showing a slight positive KPFM contrast. (c) Tip voltage histogram.

KPFM Measurements

Similar to 3,5-DHBA and 3-HBA, no well-defined KPFM contrast is observed. Fig. 7.5 shows the mobile 3-ABA stripes exhibiting a slightly positive KPFM signal.

Comparison to 3-HBA

Like 3-HBA, 3-ABA forms equidistant stripes along the $[\overline{4}2.1]$ direction consisting of molecular double rows in zigzag arrangement with 0.8 nm periodicity. Both functional groups, hydroxyl and amino group, thus, allow for a similar molecule-molecule and molecule-substrate interaction. Consequently, either amino or hydroxyl groups can be chosen as substituents for hydrogen-bonded networks on calcite.³

The mobility of the stripes composed by 3-ABA might be increased compared to 3-HBA, which indicates that the stability of the self-assembled arrangement follows the same trend as the strength of the hydrogen bond donors. This finding might provide a promising tool for future self-assembly as it allows for precisely tuning the arrangement by deliberately choosing between amino or hydroxyl substituents.

³To gain further understanding, measurements were also performed with para-substituted benzoic acid. As shown in Fig. 5.8 in Chap. 5, 4-HBA did not result in stable structures on calcite. The same behavior was observed for 4-ABA, namely the molecules are mobile. These measurements confirm the similarity of the two hydrogen bond donors.

7.3 Amide vs. Carboxyl Groups

The binding motifs of carboxylic acids and amides in their bulk crystals reveal many similarities. Both functional groups frequently form hydrogen bonds in the common dimer motif by collinear hydrogen bonding through the formation of a centrosymmetric dimer. While the binding energy of a benzoic acid dimer is calculated to be 0.74 eV, the binding energy of a benzamide dimer is only 0.61 eV [128]. This difference in binding energy influences the optimal bond lengths, which are 1.64 Å for the acid dimer and 1.86 Å for the amide dimer. Small changes can influence the optimal binding geometry in a bulk structure [127]. For instance, only 30% of the crystal structures of carboxylic acids show the dimer motif [143].

On calcite, carboxylic acids were observed to form substrate-templated structures [7, 107]. Not only molecule-substrate and intermolecular interaction determine these arrangements, but the high deprotonation tendency allows carboxylic acids to deprotonate on the calcite surface [57, 91, 92]. Acids with a pK_A lower than three have been observed to exist as deprotonated species with electrostatic binding between carboxylate ion and calcium dominating the molecule-substrate interaction. In contrast, acids with higher pK_A values have been shown to remain protonated on the surface and form hydrogen bonds ([91] and Chap. 5).

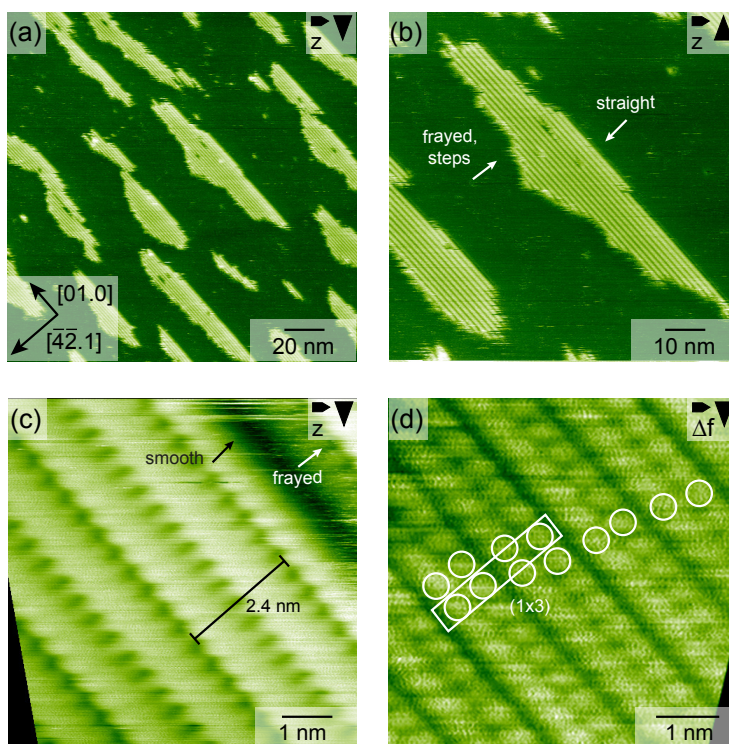
Likewise, amides, namely oligo benzamide derivatives [93], were observed to form substrate-templated structures on calcite. There is no indication for deprotonation, which is reasonable considering the comparatively low deprotonation tendency of amides compared to carboxylic acids. To compare the influence of the hydrogen-bonding characteristics of the two functional groups on the self-assembly on calcite, I study the self-assembly of benzamides in relation to the one of the corresponding protonated benzoic acids in the following.

In a first step, I compare the self-assembly of 3-HBA_{amide} with the one of 3-HBA. In a second step, the self-assembly of 3,5-

DHBamide is analyzed in comparison to 3,5-DHBA. Both amides do not form stripes, but striped islands. In the case of 3-HBAamide these islands do not resemble the 3-HBA stripes, but are composed of tilted molecules. 3,5-DHBamide on the other hand, arranges into striped islands of flat-lying molecules with a similar pattern as the 3,5-DHBA stripes, *i.e.*, I observe a transition from one-dimensional to two-dimensional growth.

3-HBAamide

Figure 7.6: Self-assembly of 3-HBAamide on calcite. (a) and (b) Topography showing elongated islands composed of stripes along the [01.0] direction. (c) and (d) Drift-corrected, high-resolution images of the molecular pattern within the islands.



Overview

Deposition of a submonolayer of 3-HBAamide onto calcite (10.4) held at room temperature, results in stable islands on the sur-

face (Fig. 7.6). Annealing up to 490 K does not change this assembly, while annealing to 550 K leads to desorption of the molecules. The elongated islands consist of stripes along the $[01.0]$ direction. In the images presented in Fig. 7.6, the right island edge appears smooth, while the left island edge appears fuzzy. Some islands appear grown together leaving a small gap and frequently holes are seen inside the islands.

The stripes along the $[01.0]$ direction are commensurate to the substrate with a periodicity of 0.5 nm. Along the $[\overline{4}2.1]$ direction the pattern is not as obvious: Two neighboring stripes form a unit with a width of 2.4 nm, *i.e.*, occupying three substrate unit cells (Fig. 7.6 (c) and (d)). Each stripe is composed of two rows of protrusions. If every protrusion corresponds to one molecule, four molecules occupy a spacing of the length of three calcite surface unit cells. Thus, not every molecule adopts the same adsorption position. Furthermore, the four protrusions do not form a straight line along the $[\overline{4}2.1]$ direction: In one of the two stripes the protrusions are aligned, in every other stripe the protrusions are shifted. The stripe with the parallel protrusions is slightly narrower than the one with the shifted protrusions. All in all, the islands show a (1×3) superstructure consisting of four protrusion per unit cell. Such a pattern is too dense to match a flat-lying arrangement of the molecules.

Adsorption Model

In an upright-standing or tilted configuration the largest part of the molecule interacts via intermolecular interactions. The bulk structure gives insight into the preferred intermolecular interactions of a specific molecule. 3-HBamide molecules form double rows in the bulk structure [144]. Two molecules, which are rotated by 180° with respect to each other, are arranged next to each other and connected *via* hydrogen bonds between the hydroxyl group at position three and the oxygen atom of the amide group (Fig. 7.7). One pair of molecules is connected to the next pair by hydrogen bonds between the hydroxyl groups at position three and the amino groups. In such a way, four molecules are connected by a ring-like arrangement of hydrogen bonds. The third dimension is realized *via* π - π -stacking in a parallel-

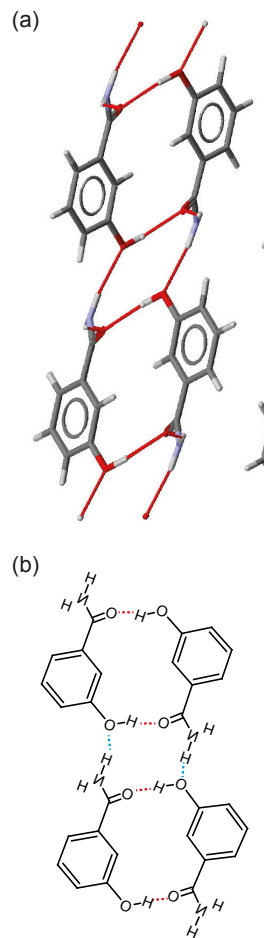
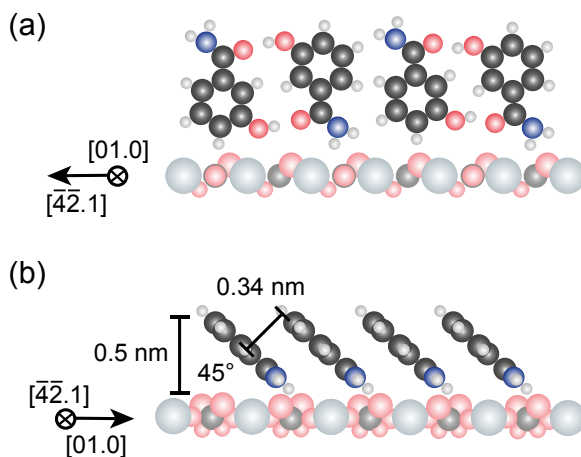


Figure 7.7: The bulk structure of 3-HBamide contains four molecules per unit cell, which are connected via a ring-like hydrogen bonding motif. (a) Structural data by [144] plotted with Mercury. (b) Sketch illustrating the hydrogen bond motif.

Figure 7.8: Bulk-like adsorption model for 3HBamide explaining the observed features. The exact adsorption positions of the molecules and the direction of the tilt in (b) are chosen randomly.



displaced arrangement of the benzene cores.

A bulk-like arrangement of 3-HBamide on the calcite (10.4) surface can explain the observed features in the nc-AFM images. Along the $[\bar{4}2.1]$ direction pairs of protrusions are observed. Similar to the bulk, the molecules could arrange pair-wise (Fig. 7.8 (a)). Instead of being connected to the next pair of molecules, hydrogen bonds between the amino group and the surface carbonate groups can be imagined. The adsorption positions of the neighboring double rows differ due to the different orientation of the carbonate groups. In Fig. 7.8 (a), w.l.o.g., the amino group of the right molecule points towards a carbonate group which is tilted out of the plane, while the next amino group points towards a carbonate group which is tilted away from the plane. This might explain the different arrangement of the molecules in the two stripes shown in Fig. 7.6 (d).

Along the $[01.0]$ direction, stripes are visible in the AFM images. The stripes could originate from a row of tilted molecules interacting *via* $\pi - \pi$ -stacking (Fig. 7.8 (b)), like in the bulk. The optimal distance of benzene cores in a parallel-displaced configuration was found to be 0.34 nm [145]. This distance is realized for a tilting angle of 43° , which results in an island height of 0.54 nm , instead of 0.8 nm for upright-standing molecules. Considering the observed apparent height of about 3 \AA a reduced island height seems reasonable.

Island Shape

The islands show a characteristic shape. They are elongated along the [01.0] direction with a straight right edge and a fuzzy, frayed left edge. While the molecules along the right edge seem to be strongly bonded (Fig. 7.6 (c)), the mobility of the molecules is increased along the left edge. Furthermore, the left edge shows many steps. The hole inside the island pictured in Fig. 7.6 (c) reveals loosely bonded molecules along this edge. Thus, molecules seem to attach and detach *via* the left side of the island, and growth of the island seems to start from this side. The difference in the island edges presumably originates from the tilt of the surface carbonate groups, which break the symmetry of the surface along this direction. Obviously, this symmetry break influences the symmetry of the molecular adsorption. Accordingly, the two molecules in a pair in the adsorption model in Fig. 7.8 are expected to adsorb in a specific orientation, as a mirrored adsorption would not lead to equivalent adsorption symmetry. From molecularly resolved images it is not possible to determine, which of the two possible orientations is correct. The island edges, however, give a reasoning for the model drawn in Fig. 7.8. In this model, the right molecule can form a hydrogen bond towards the substrate possibly explaining the clean right edge (see also Fig. 7.9). The other edge, however, is not as cleanly terminated, as the left molecule can only bound by intermolecular interaction towards the island, so that it might not be as strongly attached as one at the right island edge. Besides, the upward-pointing amino group at the left side of the left molecule might attract mobile molecules, rationalizing why the island grows from the left side. Thus, the above adsorption model gives a reasoning for the different island edges.

KPFM Measurements

The islands show a surprisingly strong, positive KPFM contrast with the mean value for several tips being $\Delta V_{3HBA\text{amide}} - \Delta V_{\text{calcite}} = 1.2\text{V} \pm 0.2\text{V}$. The origin of KPFM contrast on a bulk insulator might be due to dipoles or localized charges. On calcite, deprotonated carboxylic acids, like 2,5-DHBA [57] and 4-iodobenzoic

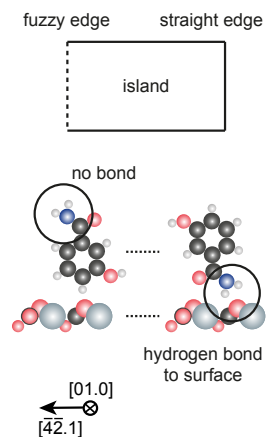
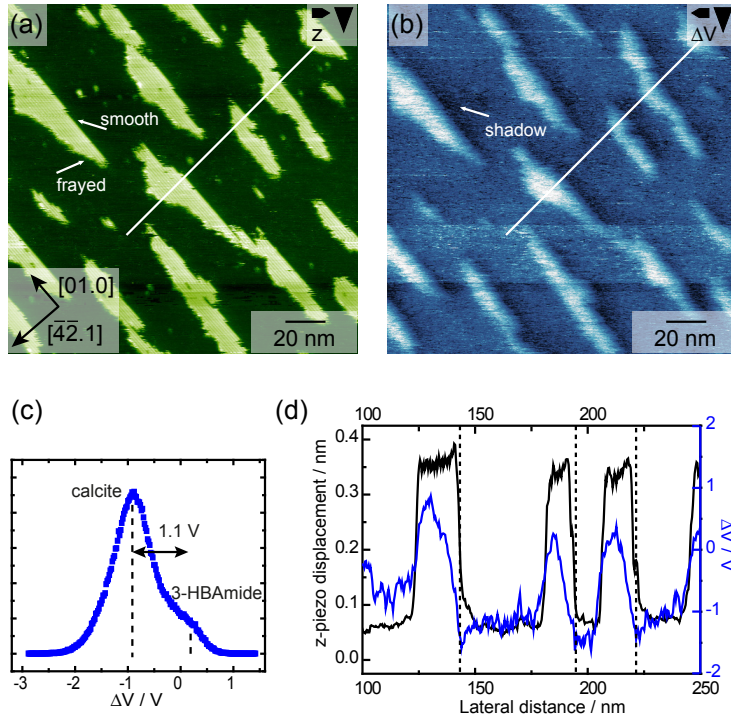


Figure 7.9: The difference in the island edges might be explained by the bulk-like adsorption model presented in Fig. 7.8.

7 Influence of Different Hydrogen Bond Donors

Figure 7.10: KPFM measurements of 3-HBAmide on calcite. (a) Topography. (b) Corresponding KPFM image showing positive islands with a more negative shadow at the right edge. (c) Tip voltage histogram. (d) Line profiles on topography and ΔV .



acid [92] were found to show strong negative contrast (≈ -1.7 V). Weaker contrast of protonated 2,5-DHBA, which has a dipole moment of 5 D, was attributed to a slight electron transfer from the substrate to the molecules [57]. Here, the contrast shows the opposite sign. An analogous explanation would be a slight electron transfer from the molecules to the substrate.

An additional feature is visible in the KPFM data: Along the right island edges a shadow appears in ΔV , independent of the scan direction. In contrast to the rest of the island, which appears more positive compared to the substrate, this area appears more negative. The line profiles in Fig. 7.10 (d) suggest, the most negative part coincides with the right island edge with ΔV slowly increasing afterward. Possibly, this shadow is related to the difference in the island edges. In the proposed model, the amino groups point upward along one island edge, while they point downward along the other island edge. If the KPFM sig-

nal is due to an interface dipole, a different orientation of the molecules might result in a different KPFM signal along the two island edges due to a different charge distribution.

Comparison to 3-HBA

Obviously, the assemblies of 3-HBA_{amide} and 3-HBA on calcite differ greatly: While 3-HBA_{amide} forms islands with a (1×3) superstructure, 3-HBA arranges into stripes along the [42.1] direction, with a (4×1) superstructure at one monolayer coverage. Besides, 3-HBA_{amide} shows well-pronounced, positive KPFM contrast, while the KPFM signal obtained for 3-HBA is quite small.

Here, switching between an OH and an NH₂ group changes the self-assembly completely. While hydroxyl and amino groups substituted at the benzene core were found to contribute in a similar way to the self-assembly on calcite (Chap. 7.2), their contribution differs significantly if they are part of the acid/amide group.

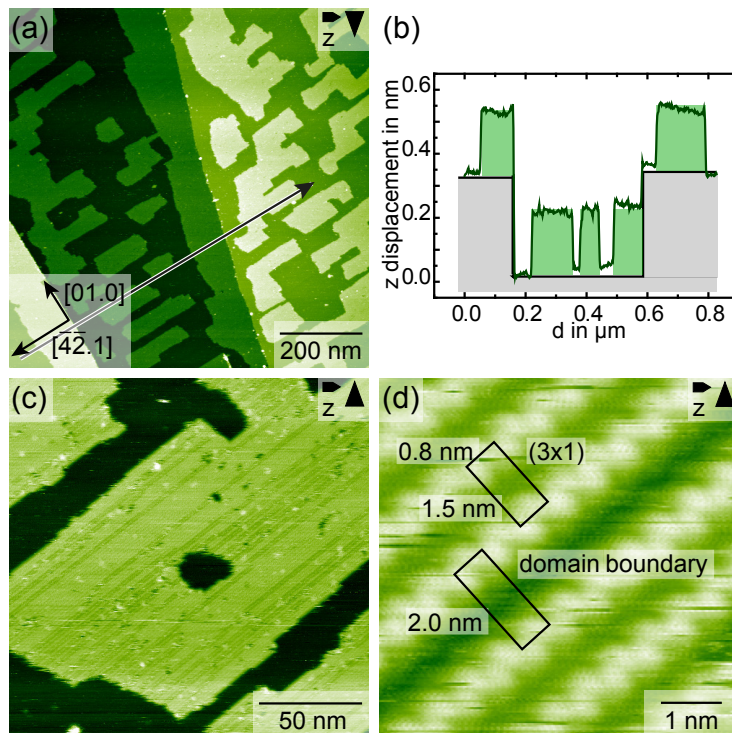
There are several possible explanations. Switching from acid to amide does not only change the strength of possible hydrogen bonds but also the preferred bond length and directionality. As known from an analysis of crystallographic structures, about 30% of the structurally analyzed carboxylic acids form dimers, while only 10% of amides form dimers [143], indicating a stronger favor towards dimer formation of acids. The pattern of flat-lying 3-HBA allows for an arrangement, in which the carboxylic groups interact while pointing at each other. The upright pattern of 3-HBA_{amide} on the other hand, is dominated by an interaction parallel to the molecules.

Another possible explanation might be related to the different KPFM contrast. Difference in KPFM signal hints at a different charge distribution, which might change the electrostatic interaction with the substrate.

3,5-DHBAmide

The previous paragraphs have shown that 3-HBAmide forms tilted, possibly bulk-like islands. An increased number of hydroxyl groups, which can form hydrogen bonds towards the surface, might increase the molecule-substrate interaction and lead to a flat-lying assembly of the molecules. Such an assembly might be closer related to the one of the corresponding acid, which was found to arrange flat on the calcite surface (Chap. 6). Indeed, 3,5-DHBAmide forms islands composed of flat-lying molecules with some similarity to 3,5-DHBA. In this section, I first describe the islands composed of 3,5-DHBAmide and then compare the two-dimensional arrangement of 3,5-DHBAmide to the one-dimensional arrangement formed by 3,5-DHBA.

Figure 7.11: Self-assembly of 3,5-DHBAmide on calcite. (a) Assembly in large, rectangular islands with borders aligned along the substrate directions. (b) Height profile taken at the indicated position in (a), elucidating substrate steps and molecular islands. (c) Detailed image of a striped island with holes and domain boundaries. (c) Drift-corrected, high-resolution image of an island showing the (3×1) superstructure and a domain boundary.



Overview

3,5-DHBamide forms extended islands on the calcite (10.4) surface at submonolayer coverage (Fig. 7.11 (a)). The apparent height of the islands is quite low, the islands appear even lower than the monatomic substrate steps in Fig. 7.11 (a) and (b). The surface area in subfigure (a) shows three calcite terraces with the one in the center being a monatomic step lower. On a terrace, the islands have a rectangular shape aligned with the substrate directions. Along the left side of the step edges in Fig. 7.11, that is coming from the $[\bar{4}2.1]$ direction, the molecules assemble in an elongated island, no matter if the calcite step goes up or down. The step on the left side of the image runs along the $[01.0]$ direction, the right one is not completely straight, but presumably a higher indexed step composed of many low-indexed steps. Due to the tilt of the carbonate groups, step edges on calcite are not symmetric (Fig. 7.12). It is known, that the obtuse and acute step edges of calcite, the two most stable step edges, show different reactivities [116]. Obviously, such a distinction also exists for steps approximately along the $[01.0]$ direction. Along this direction the tilt of the carbonate groups is most prominent (Fig. 7.12). The preferential arrangement of 3,5-DHBamide might be related to the geometrical arrangement of the molecules due to the tilt of the carbonate groups or could be of electrostatic origin, as charges might be differently distributed along the step depending on the termination. The same preference towards these calcite steps has been observed for several other molecules on calcite as well, *e.g.*, oligo iodo benzamides [93], but it is not observed for every molecule on calcite, *e.g.*, 3-HBamide does not show any preference for specific step edges.

Adsorption Pattern

Inside the islands, 3,5-DHBamide arrange into commensurate stripes along the $[\bar{4}2.1]$ direction with a periodicity of 0.8 nm in a zigzag arrangement (Fig. 7.11 (c) and (d)). Along the $[01.0]$ direction the repeat distance is 1.5 nm, resulting in a (3×1) superstructure. Domains are separated by domain boundaries, which exhibit an interrow-distance of 2.0 nm, *i.e.*, the molecules are dis-

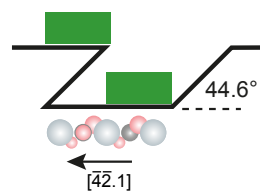
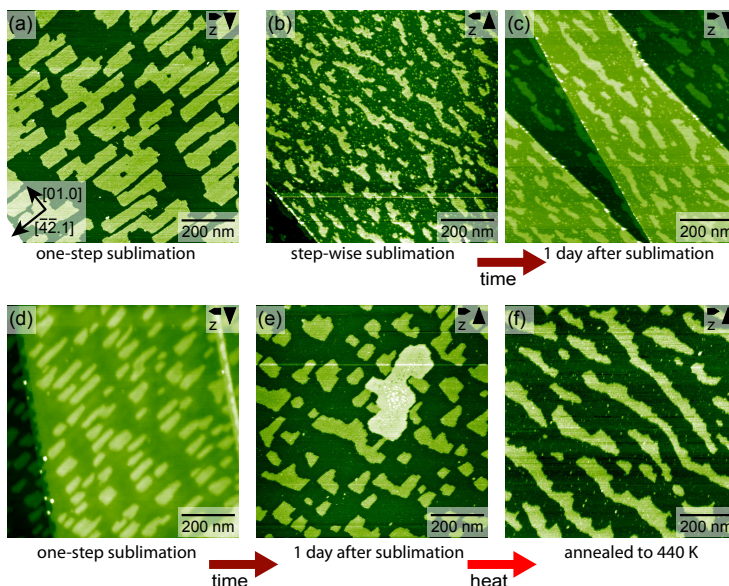


Figure 7.12: Due to the tilt of the carbonate groups, step edges along the $[01.0]$ direction are not symmetric but show an angle of about 45° . 3,5-DHBamide islands (sketched as green rectangles) arrange only from the left side to the steps.

Figure 7.13: Island shape of 3,5-DHBamide islands on calcite(10.4). Initial shape of the islands after (a) and (d) sublimation in one step and (b) sublimation in several steps. (c) and (e) - (f) reveal the change of the initial island shape over time and due to annealing. The second island morphology in (e) is referred to later.



placed by one substrate unit cell. The large density of the line defects suggests significant stress of the arrangement, which will be discussed in connection with the island shape.

A similar adsorption as for 3,5-DHBA can be imagined, as both molecules arrange in double rows along $[4\bar{2}.1]$ with a zigzag arrangement. For 3,5-DHBA, the stripe separation appears quite large compared to the molecular dimension. A slightly altered adsorption position in the case of 3,5-DHBamide might be the reason for a more dense packing with a stripe distance of 1.5 nm without largely altering the overall adsorption geometry.

Island Shape

The island shape depends on the preparation conditions and varies over time. Fig. 7.13 displays a series of samples prepared using different sublimation conditions, after waiting or annealing. If the molecules are sublimed in one step, the islands show the previously described rectangular shape (Fig. 7.13 (a) and (d)). Step-wise sublimation (Fig. 7.13 (b)) results in smaller, ir-

regularly shaped islands, which are elongated along the $[01.0]$ direction. Upon waiting, the mean island size increases (Fig. 7.13 (c)). Islands of similar shape form upon time and after annealing for a sample with previously rectangular shaped islands (Fig. 7.13 (d) - (f)). The left island edge of these islands appears smoother, while the right edge exhibits more kinks. Such large, elongated islands with kinks exist up to annealing to 520 K. After annealing to 550 K the island shape is still the same, but the size is reduced indicating that the molecules started to desorb from the surface. To conclude, the elongated islands seem to be thermodynamically more stable than the rectangular islands.

Fig. 7.14 illustrates the observations: Rectangular islands with a dimension of 100 nm along $[\overline{42}.1]$ and 40 nm along $[01.0]$ (typical values for the sample in Fig. 7.13 (d) to (f)), combine to an elongated island with up to several hundred nanometer extension along $[01.0]$ by slightly reducing the length along $[\overline{42}.1]$. In the sketch, long islands were divided into two islands to visualize this effect. Besides, the resulting island shows a more irregular shape with kinks instead of a rectangular shape.

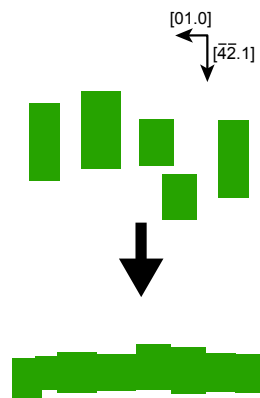


Figure 7.14: Schematic illustrating the change in island shape upon time.

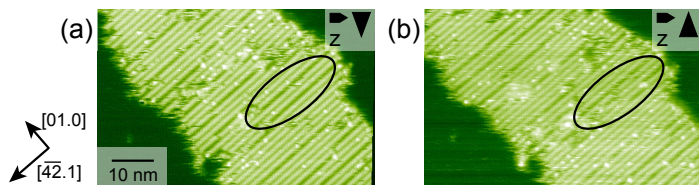


Figure 7.15: Consecutive drift-corrected images of 3,5-DHBAamide revealing changes and shifts in the domain boundaries. To visualize the domain boundaries, the image in (b) was processed using a line-by-line correction.

Independent of the island shape, the adsorption pattern within the islands stays the same, indicating that the adsorption geometry of the individual molecules remains unchanged. As the islands are composed of stripes along the $[\overline{42}.1]$ direction with domain boundaries along the same direction, the initial rectangular shape elongated along the $[\overline{42}.1]$ direction is the intuitive one. However, the domains are not static, but a reordering of the domain boundaries is observed. As highlighted in Fig. 7.15, domain boundaries can change between consecutive images. Stripes break or holes appear in long stripes indicating stress or weak intermolecular interaction along this direction. Thus, despite the large number of domain boundaries along

$[\overline{42}.1]$, the interaction along $[01.0]$ dominates. Over time, the domains seem to stabilize by forming irregularly shaped domains elongated along the $[01.0]$ direction with many short boundaries. The reason for this behavior remains unclear. Still, the large amount of reordering hints at a less favorable adsorption arrangement compared to the acid 3,5-DHBA. The larger amount of kinks at the right island border might be related to the adsorption behavior at step edges.

KPFM Measurements

The islands show a positive KPFM contrast with respect to the calcite surface (Fig. 7.16 (b)). A mean difference of $\Delta V = 1.1\text{V}$ between calcite and molecular islands is acquired for several tips. This difference is comparable to the one between 3-HBamide and calcite. The different adsorption patterns (upright-standing versus flat-lying) of the molecules imply that the KPFM contrast is not solely related to the orientation of the molecules on calcite. The fact that the same contrast is observed for both amides suggests a connection to the functional group contained by both molecules, the amide group. In contrast to molecules with a carboxyl group, for which the negative KPFM contrast of (protonated) 2,5-DHBA was attributed to a slight electron transfer from the substrate to the molecules creating a dipole, the amide group might result in a slight electron transfer from the molecules to the substrate. Calculations are required to understand the mechanism of such an electron transfer or a dipole formation between amides and calcite.

An additional observation, which is not related to the molecular islands, is a shift in the KPFM signal for the different calcite terraces. Tip voltage histograms acquired on the two different terraces are shown in Fig. 7.16 (b). Both histograms show the same difference between calcite and molecular islands. However, the histograms are shifted by about 0.3V , indicating that the background KPFM signal is different for the two calcite terraces. Such a shift of the absolute value of the KPFM signal on different terraces of a bulk insulating substrate has been observed before on $\text{NaCl}(001)$ and was attributed to a different charge distribution on or below the terraces [52]. It is observed

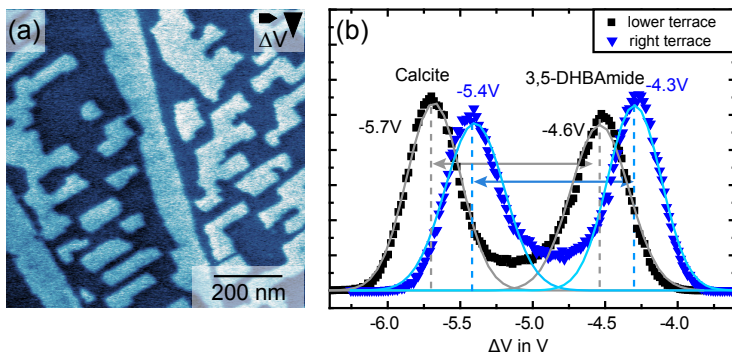


Figure 7.16: KPFM measurements of 3,5-DHBAmide. (a) Corresponding KPFM image to Fig. 7.11 (a). (b) Tip voltage histograms of lower terrace (black rectangles) and upper, right terrace (blue triangles) showing the same difference of -1.1V between calcite and molecular islands but exhibiting a shift of 0.3V of the absolute values.

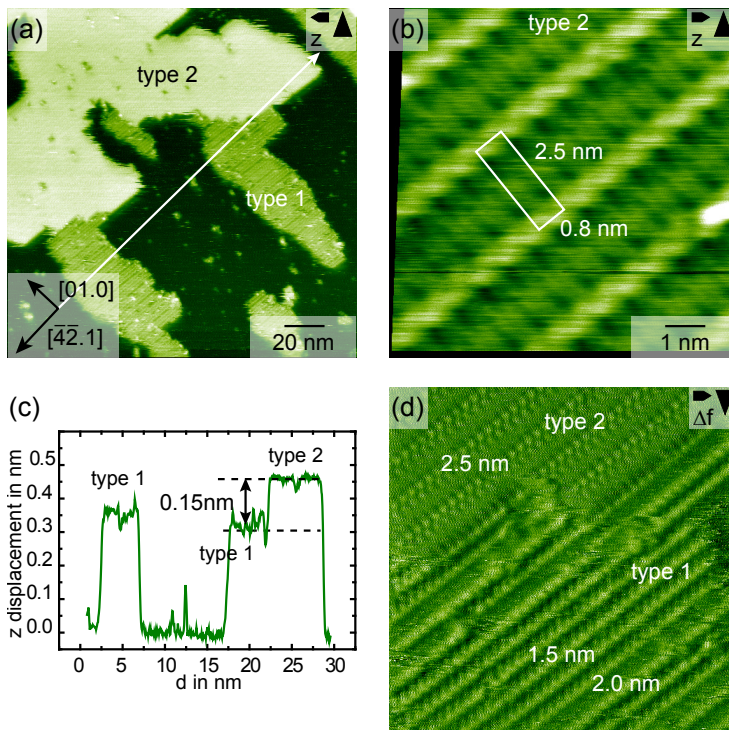
that the absolute value of the KPFM signal measured on calcite differs for different samples, depends on the preparation conditions, varies over time and depends on the tip. Especially after cleavage, many bulk insulating samples are observed to be charged [52], with the charge state decaying over time. As in both areas the absolute signal is not negligible on calcite, but shows a value of around $5\text{-}6\text{V}$, charges seem to be present, so that a difference in the charge density on the two terraces seems plausible.

Second Island Type

In some areas, *e.g.*, in Fig. 7.13 (e), a second island type is observed (Fig. 7.17). Islands of this type are always connected to the islands described previously. The larger apparent height of the second island type suggests an upright-standing configuration or a second layer. A second layer configuration seems plausible as the islands appear to overgrow first layer islands. The second island type shows a (5×1) superstructure with two features per unit cell. The part with the lower apparent height in the unit cell marked in Fig. 7.17 (b) resembles the zigzag arrangement of the first type along the $[4\bar{2}.1]$ direction. Between these zigzag rows protruding rows occur.

The two island types cannot be distinguished by their KPFM contrast indicating a similar charge distribution, which is not dominated by the molecular orientation. This is plausible considering the similarity with the KPFM contrast of the differ-

Figure 7.17: Second island morphology of 3,5-DHBAamide. (a) Topography showing type 2 island growing next to/on top of type 1 island. (b) Drift-corrected, high-resolution image of type 2 island revealing (5×1) superstructure. (c) corresponding line profile to (a) visualizing the difference in apparent height. (d) Frequency shift image of the transition between the two island types.



ently assembled 3-HBAamide. The existence of a second layer at low coverages suggests that the molecule-molecule interaction is stronger than the molecule-substrate interaction, giving further evidence of the rather weak molecule-substrate interaction of 3,5-DHBAamide with calcite.

Comparison to 3,5-DHBA

3,5-DHBAamide and 3,5-DHBA both arrange into a commensurate pattern of flat-lying molecules with 0.8 nm periodicity along the $[4\bar{2}.1]$ direction. While individual stripes are stable for 3,5-DHBA, the corresponding amide forms striped islands. The minimum distance of the 3,5-DHBA stripes is 2 nm, only at one monolayer coverage 1.5 nm are observed at domain boundaries. 3,5-

DHBamide islands show distances of 1.5 nm with domain boundaries of 2.0 nm. Furthermore, over time, the stripes in the islands break forming narrow islands, which connect along the [01.0] direction. While the assembly of 3,5-DHBA is dominated by the strong interaction along the stripes, *i.e.*, along the $[\overline{42}.1]$ direction, the assembly of 3,5-DHBamide appears to be dominated by the interaction between the stripes, *i.e.*, along the [01.0] direction. Possibly the linking along $[\overline{42}.1]$ is realized in a similar way but weaker due to the weaker hydrogen bonding strength of the amide group. Besides, the pronounced positive KPFM contrast on 3,5-DHBamide hints at an electrostatic contribution to the structure formation, which also might explain differences in the assembly.

7.4 Conclusions

In conclusion, I present how small changes in the hydrogen bonding characteristics influence the resulting hydrogen bonded networks on calcite.

The comparison of 3-HBA and 3-ABA reveals that switching between hydroxyl- and amino-substituted molecules does neither influence the adsorption pattern nor the long-range order. Thus, amino or hydroxyl substituents can be chosen depending on convenience or due to further considerations like required functionalization.

A greater variation is achieved by switching between carboxylic acids and amides, in which case I observe a transition from one-dimensional to two-dimensional growth. For the comparison of 3-HBamide and 3-HBA, *i.e.*, benzene with two functional groups, the two-dimensional and one-dimensional patterns differ strongly. In the case of three functional groups for 3,5-DHBamide and 3,5-DHBA, the two-dimensional islands are composed of stripes resembling the one-dimensional pattern. As expected, the influence of changing a functional group is stronger with smaller number of interacting functional groups. In all cases, the hydrogen bonded networks are more stable with oxygen containing groups than with nitrogen containing groups following the trend of the stronger electronegativity.

Interestingly, both amides show similarly strong, positive KPFM contrast despite their completely different arrangement. This opposite sign of the KPFM contrast compared to carboxylic acids like 2,5-DHBA, implies a different charge distribution and supports the idea of different molecule-surface interactions for the two molecular groups due to electrostatic interaction.

8 Long-Range KPFM Contrast on Monopole and Dipole Assemblies

Contents

8.1 Introduction	120
8.2 Experimental Details	122
8.3 Slices: Lateral and Vertical Signal Extension	126
Sample with High Molecular Coverage	126
Sample with Low Molecular Coverage	127
Determination of the Effective Area	130
8.4 Long-Range Curves: Shape of the Distance Dependence	134
Long-Range Electrostatics	134
Tip Influence	141
Long-Range Van-Der-Waals	142
8.5 Conclusions	145

The KPFM contrast mechanism of organic molecules on bulk insulators is not well understood yet and often ascribed to the formation of dipoles. The considerations in Chap. 2.3 suggest a distance dependence of the KPFM signal in the presence of local charges.

In this chapter, I study 2,5-DHBA on calcite as a model system for dipole islands (protonated 2,5-DHBA) and monopole islands (deprotonated 2,5-DHBA) on a bulk insulator. Using 2-dimensional Kelvin probe force spectroscopy, I demonstrate a distinctly different long-range distance dependence for the differently charged molecular islands.

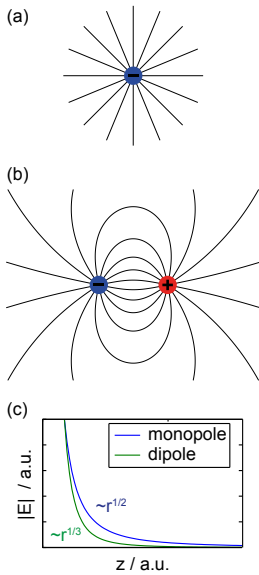


Figure 8.1: Electrostatic field lines of (a) a single charge, (b) a dipole and (c) the distance dependence of the electrostatic field above a monopole and a dipole.

8.1 Introduction

One possibility to describe charge distributions is to use the electric field. The total electric field is the superposition of the fields created by all individual charges. For a monopole and a dipole, the electric field and its distance dependence are visualized in Fig. 8.1. KPFM minimizes the electrostatic interaction between a tip and a sample (see Chap. 2.3). In the vicinity ($z \approx 1 \text{ nm}$) above a single molecule, the KPFM signal was found to resemble the z -component of the electric field caused by the molecule [13, 146]. The electric far-field above adsorbates in a tip-sample system is expected to be caused by a variety of components. Between metal tip and metal sample, the electric field originates from the difference in work function between the two metals. While the geometrical arrangement is expressed by the capacitance, the condition $\partial F / \partial V = 0$ and, thus, the KPFM signal is only determined by the work function difference, which is not distance dependent (Chap. 2.3). Therefore, a distance dependence observed on structured metal samples is attributed to averaging caused by the large tip segment, which contributes to the KPFM signal [147–149]. The same is expected in the case of a thick, nonpolar dielectric material on top of the metal substrate (Chap. 2.3). The dielectric material only changes the capacitance of the system, but not the zero-force condition, which is again proportional to the difference between the applied voltage and the work function difference between the backelectrodes. If, however, a local charge is present in the system, the force is not only described by the capacitive interaction, but an additional contribution occurs. The analysis in Chap. 2.3 showed that this contribution is determined by the geometry and composition of the tip-sample system and is most likely distance-dependent. In the case of finite assemblies of charges, an additional term for each charge exists in the KPFM condition. The distance dependence of the resulting KPFM signal is then determined by the distance dependence of the sum over all contributions, similar to the simple picture of a monopole and a dipole (Fig. 8.1).

While the atomic scale variations and their distance dependence are discussed by several studies [55, 63, 69, 150, 151], the origin of the contrast on assemblies of organic molecules on bulk

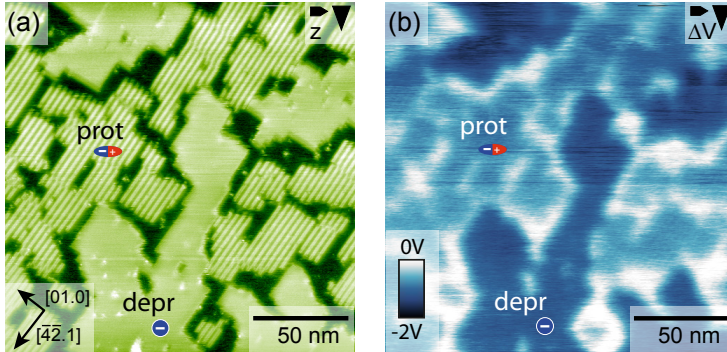


Figure 8.2: Representative KPFM measurement of 2,5-DHBA on calcite (10.4) showing (a) the topography and (b) the corresponding KPFM signal at one specific Δf setpoint, here $\Delta f = -5$ Hz. An offset is added such that $\Delta V_{\text{calcite}} = 0$.

insulators [54–56, 58, 152] is still poorly understood and mostly attributed to the formation of dipoles. Typically, a distance dependence is neglected and the performed KPFM measurements yield only one experimental channel at one specific Δf setpoint, namely the KPFM signal ΔV .

Here, I study 2,5-DHBA on calcite (10.4) as a model system to further understand the KPFM contrast mechanism on monopole and dipole arrangements on a bulk insulator. Two phases of 2,5-DHBA are known to exist on the calcite surface, one is ascribed to protonated molecules, the other to deprotonated molecules ([57] and Chap. 5). Both phases form distinctly different islands as depicted in Fig. 8.2. The protonated molecules arrange in such a way that dipoles develop, while the islands formed by deprotonated molecules are understood to be negatively charged yielding a more pronounced KPFM signal at a specific Δf setpoint. Consequently, 2,5-DHBA/calcite acts as an extremely well-suited model system to study the difference in the long-range KPFM signal of a monopole and a dipole arrangement on a bulk insulator.

As described in section 8.2, 2D-Kelvin probe force spectroscopy (KPFs)¹ was employed to visualize the different charge distributions. Based on these 2D data, the lateral and vertical extension of the KPFs signal is discussed in section 8.3 including effects like averaging. The shape of the long-range curves, *i.e.*, their

¹For simplicity I denote $\Delta V(z)$ curves Kelvin Probe Force spectroscopy or KPFs in analogy to [148].

Overview data 10

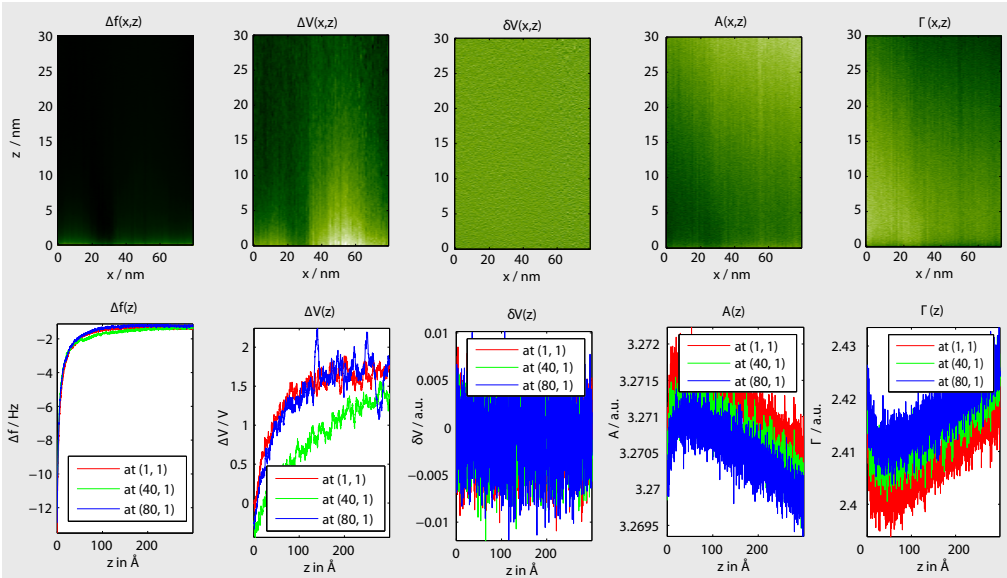


Figure 8.3: Overview of 2D-spectroscopy data set for *data10* showing all data channels which were acquired: frequency shift (Δf), KPFM signal (ΔV), KPFM error (δV), amplitude (A) and dissipation (Γ).

starting values and their curvature, is reported in section 8.4 accompanied by a detailed discussion of the contributions to the tip-sample interaction. The main conclusions are summarized in section 8.5.

8.2 Experimental Details

The following channels are acquired during KPFS experiments: frequency shift (Δf), KPFM error signal (δV), KPFM signal (ΔV), amplitude (A) and dissipation (Γ). PLL, amplitude and KPFM feedback are engaged during acquisition of each curve, while all above-mentioned channels are recorded simultaneously. The topography feedback is switched off during data acquisition. The measurement data are contained in Δf , ΔV and Γ , the control signals of the feedback loops are phase, δV and A . Each spectrum was started close to the sample by typically retracting the tip by 30 nm in 2000 points, at which the data was acquired. The retract curve is followed by an approach curve with the same

number of data points. An acquisition time of 10-20 ms was used at each data point. For a 2D (x,z)-data set, also referred to as slice, typically a total of 75 to 150 z-spectra were acquired on a line orientated along the x-direction. After each spectrum, the z-feedback was enabled for several seconds to correct for the z-position before acquiring the next spectrum. Along the x-direction the slices extend over 50-150 nm, with a resolution of 1 point/nm. Thus, the slices are dense along the z-direction but comparable sparse along the x-direction. Using such parameters, the acquisition of a 2D-data set takes typically about 1.5 hours.

Fig. 8.3 shows all recorded channels of a 2D-data set. The upper row presents the slices, the lower row depicts three selected spectra, namely the first (at $x = 0$ nm), the last (at $x = 80$ nm) and the one in the middle (at $x = 40$ nm). For the slices, only the $\Delta V(z, x)$ channel shows pronounced substrate-related contrast over the whole z-range. Within each single spectrum, the channels $\Delta f(z)$ and $\Delta V(z)$ show significant variations. Typical frequency shift versus distance curves presenting attractive interactions are found at each lateral position, with the interaction only being present in the first few nanometers. Furthermore, small long-range variations between different sample regions are observed. $\Delta V(z)$ starts at a value corresponding to the specific substrate feature and reaches a more positive constant offset after several tens of nanometers, as discussed in detail throughout this chapter. The KPFM error signal $\delta V(z)$ only consists of noise indicating proper *feedback conditions*. For completeness, amplitude and dissipation are shown as well in the same figure. Except close to the sample in the z-range [0 nm, 3 nm], the amplitude feedback was working correctly. The decrease in amplitude and increase in dissipation along z is attributed to an artifact of the measurement system. Variations of amplitude and dissipation with different absolute z-piezo positions are frequently observed with the VT-AFM. This effect is tentatively explained by a non-linear transfer function between the excitation signal amplitude for the excitation piezo and the resulting cantilever oscillation amplitude [153]. As no similar variations are observed in the other channels, crosstalk is unlikely. Moreover, these variations are below 0.1%.

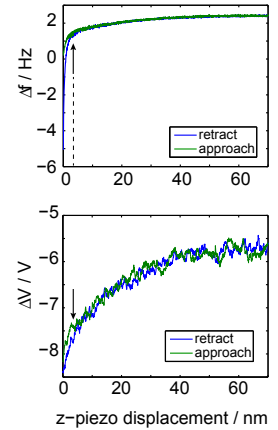
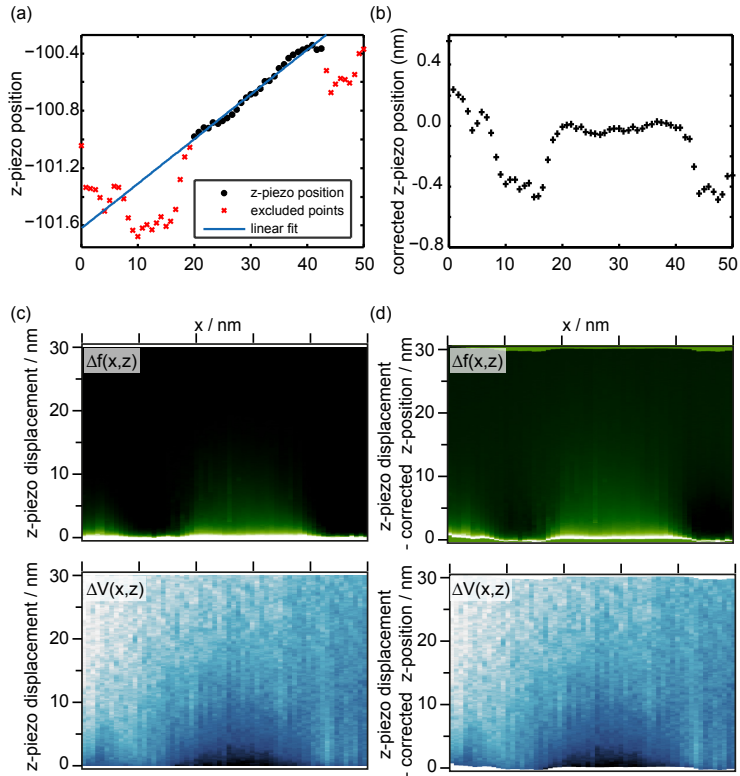


Figure 8.4: Hysteresis between retract and corresponding approach at z-range of 70 nm.

Figure 8.5: *Data15* on calcite and deprotonated island in constant height representation. (a) Recorded z-position with linear fit. (b) z-position corrected for linear z-drift. (c) Raw data of $\Delta f(z,x)$ and $\Delta V(z,x)$. (d) Constant height representation of $\Delta f(z,x)$ and $\Delta V(z,x)$ after subtracting the corrected z-positions using (b).



Piezo creep along z becomes apparent over the large z -range used herein. Fig. 8.4 shows an example of retract and corresponding approach curve of $\Delta f(z)$ and $\Delta V(z)$. As Δf is rather flat and ΔV rather noisy for large z , the creep is only visible in the first 3-4 nm with the deviation in ΔV being smaller than 0.5 V, *i.e.*, comparable to the noise. Such an hysteresis seems reasonable for a z -range of 70 nm.

Data acquisition over long time is always subject to *thermal drift*. Before starting the 2D-data acquisition, I waited for stable measurement conditions and used the atom tracking system described in [30] to compensate for linear z -drift. During 2D-data acquisition the z -drift compensation was not adjusted further, but the absolute z -position of each spectrum was recorded. As the z -feedback was engaged between consecutive spectra, the z -

position before each spectrum reflects the topography of the sample along the x-direction superimposed with the z-drift during the measurement. If this z-drift is linear, the substrate-related z-position can be extracted and used to present the 2D-data set as *constant height data*. In the example in Fig. 8.5, the z-drift is linear except for the first points (Fig. 8.5 (a)). Thus, a linear function can be fitted and subtracted, resulting in the z-position relative to the sample (Fig. 8.5 (b)). The curves in the 2D-data set (raw data in Fig. 8.5 (c)) were shifted by subtracting the corrected, relative z-position. The resulting constant-height representation is shown in Fig. 8.5 (d). After drift correction, I find maximum z-shifts of 0.4 nm corresponding to the apparent height of the molecular islands. Compared to the the full z-range of 30 nm, this corresponds to an uncertainty of about 1%. Consequently, this correction is not applied to all data sets.

A total of 15 2D-data sets (*data1* - *data15*) were acquired on three different samples (*sample1* - *sample3*) using three different tips (*tip1* - *tip3*). A thorough analysis shows that in some slices the absolute values of $\Delta V(x, z_{end})$ shift. As the data was acquired using highly doped silicon tips which are possibly not perfectly conducting, such changes are attributed to a change in the charge state of the tip [154], which might also be induced by molecules attached to the tip. The data sets discussed in the following were carefully selected to only address those without such tip changes.

Additional to the 2D-data sets, numerous individual curves were acquired with a larger z-range of up to 100 nm.

8.3 Slices: Lateral and Vertical Signal Extension

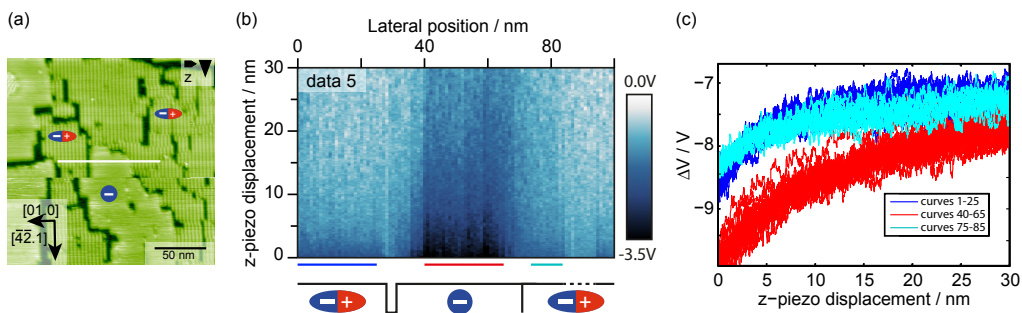
In this section, I present slices acquired on two samples with different molecular coverages. These data clearly present the distance dependence of the KPFM signal above the different substrate features. I discuss the lateral and vertical range of the KPFM signal including the averaging effect, while a discussion of the shape of the $\Delta V(z)$, including its curvature, follows in section 8.4.

The deprotonation of 2,5-DHBA on calcite (10.4) occurs at room temperature with strongly coverage-dependent kinetics. At coverages below about 0.7 ML^2 , protonated islands are completely absent already a few hours after molecule deposition, *i.e.*, all molecules are deprotonated before stable spectroscopy conditions are reached. At coverages of 0.95 ML and higher, the deprotonation process is inhibited, as soon as a specific coverage of deprotonated islands exists. In the following, I present data on two different samples. In the case of high molecular coverage, the molecular islands directly touch, in the case of low molecular coverage, calcite is clearly visible between the islands.

Sample with High Molecular Coverage

Some data sets were acquired on a sample nearly completely covered by 2,5-DHBA (Fig. 8.6 (a)). At the time of the measurement no further island changes were observed: the islands were either already deprotonated or they stayed protonated. The scan direction is rotated such that the island borders are perpendicular to the x-direction. A line in Fig. 8.6 (a) marks the position at which the 2D-spectroscopy *data5* was recorded. Below this line, a shift in the topography indicates the position where the scan was stopped before the slice and resumed after the slice. The shift is due to lateral drift during spectra acquisition, in this

²The deprotonation kinetics of 2,5-DHBA on calcite are currently under investigation but not completely understood yet.



case about 10 nm along $-x$. This drift was considered when assigning the substrate features to the 2D-data. In addition, steps in the absolute z -position were considered for a correct assignment of the island edges.

According to this assignment, Fig. 8.6 (b) shows from left to right a protonated island, a narrow gap, a deprotonated island and again a protonated island. In subfigure (c), the spectra recorded in the center of each region are plotted, *i.e.*, protonated (dark blue), deprotonated (red), protonated (light blue). The gap between the islands is so narrow that only two spectra were recorded in this region. As the z -position differs for calcite and the molecular islands (which show the same apparent height), this can be concluded from their differing starting position in z . Consequently, except for these two curves, this slice was recorded in constant height due to the same apparent height of the two types of molecular islands. It allows for the following observations: Firstly, both types of 2,5-DHBA islands on calcite exhibit long-range $\Delta V(z)$ contrast, which extends up to at least 30 nm in z . Secondly, the distance behavior differs significantly for the differently charged 2,5-DHBA islands. As in the case of dipoles, the overall charge is neutral, the stronger pronounced signal above the deprotonated islands seems reasonable.

Sample with Low Molecular Coverage

In the next step, I present data acquired on a sample with lower coverage of 2,5-DHBA as pictured in Fig. 8.7. Here, calcite areas are visible next to the islands. At this coverage, deprotonation

Figure 8.6: *Data5* acquired on *sample2* with *tip2*. (a) Topography (line-by-line corrected) with a line marking the position of the 2D-data set. (b) $\Delta V(x,z)$. (c) Curves on the three regions for the areas marked in (b). On protonated islands: 1-25 (dark blue) and 75-85 (light blue). On deprotonated island 40-65 (red).

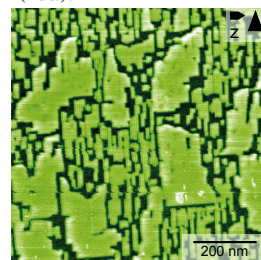


Figure 8.7: Topography of *sample3* (line-by-line corrected). On a timescale of hours small protonated islands disappear, while large, deprotonated islands grow.

8 Long-Range KPFM Contrast on Monopole and Dipole Assemblies

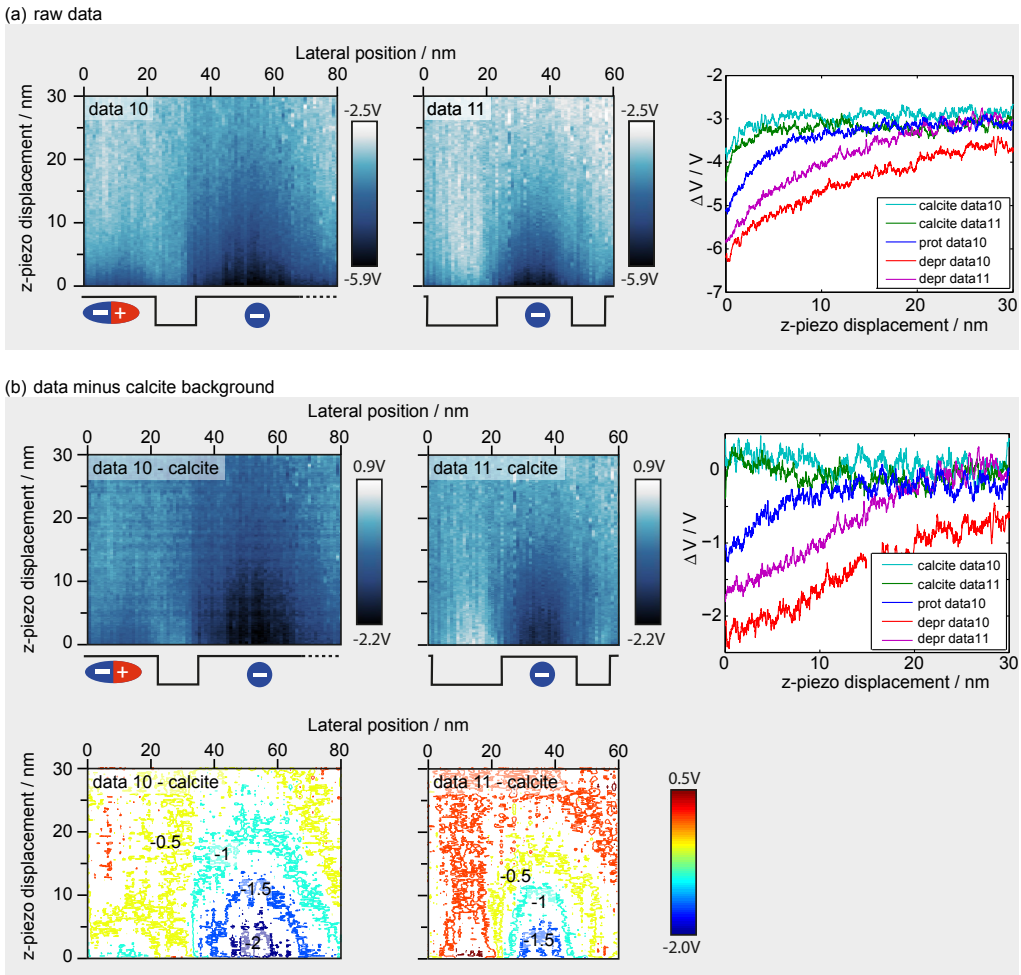


Figure 8.8: *Data10* and *data11* acquired on *sample3* with *tip2*. (a) Raw $\Delta V(x,z)$ data and selected $\Delta V(z)$ curves. (b) The same slices, curves and corresponding contour plots after subtraction of the calcite background.

proceeds on a time scale of hours to days, thus, protonated islands can disappear and deprotonated islands can grow during 2D-data acquisition. To assign the features in $\Delta V(x,z)$ correctly, images before and after the slice are compared to assign the island type, while the absolute z -position is used to identify the position of the island edges, as at island edges a step in the z -position occurs due to the change in apparent height. The slice *data10* (Fig. 8.8) contains a protonated island, a bare calcite

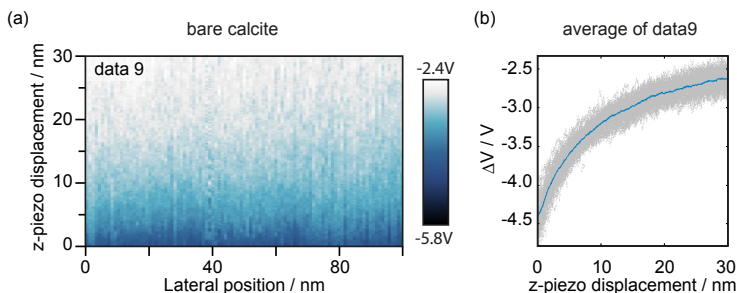


Figure 8.9: 2D-data on bare calcite (*tip2*, *sample3* before molecule deposition) shows a distance dependence of the long-range KPFM signal. The colorscale is adjusted to the same range as for slices on 2,5-DHBA/calcite to visualize the different magnitude of the signals. (b) shows tall curves of *data9* with the average superimposed.

region and a deprotonated island (from left to right). *Data11* shows calcite and a deprotonated island, which is narrower than the one in *data10*. As in the case of high molecular coverage, a long-range distance dependence is observed on all regions with the signal above the deprotonated islands being longer-ranged and more negative than above the protonated islands. Surprisingly, a distance dependence is also observed on calcite.

The raw KPFS data does not only show the local electrostatic behavior of 2,5-DHBA on calcite, but also includes contributions from the whole tip-sample system. Fig. 8.9 shows a slice acquired on a bare calcite surface without 2,5-DHBA. Surprisingly, a significant long-range distance dependence is observed on bare calcite. The considerations for the plate capacitor filled with a dielectric in Chapter 2.3 demonstrate that no distance dependence is expected in the KPFM signal for a nonpolar dielectric in the absence of charges. Consequently, charges need to be present to explain the observed distance dependence on bare calcite. One possibility is the existence of a surface double layer. Due to bivalent impurities in the bulk, alkali halides exhibit a negative surface charge to ensure charge equalization [5]. As the calcite crystals are of natural origin impurities in the bulk might be present. Besides, cleavage of bulk insulators in UHV is observed to produce a considerable amount of charges, which are present for a long time due to the low ion conductivity [52].

Another origin are charges on the tip. As tip charging was observed during data acquisition of several slices, such a contribution can also be plausible.

Here, I am interested in the difference of the distance depen-

dence of the charged molecular islands and the islands consisting of dipoles. If we assume an additive background, the background can be subtracted from the experimental ΔV data (more information in section 8.4). This approach to separate the measurement related quantities of the KPFM signal, *i.e.*, the distance dependence of the substrate, and the components related to surface features by subtraction has been used before [148, 155]. As curves quantitatively differ for different tips, the calcite curves recorded directly before and after each slice are averaged and then used for subtraction resulting in the corrected 2D-data as shown in Fig. 8.8 (b).

After background subtraction, the distance dependence should be defined only by the molecular islands and their interaction with calcite only. Qualitatively, there is no difference between the slices before and after calcite background subtraction. For a further comparison, one might look at the curves plotted next to the 2D-data. The curves on calcite are zero within the noise limit after subtraction of the averaged calcite curves. Curves on the molecular islands seem to increase linearly (discussion in 8.4) until no interaction is reached after specific distances. Upon retraction of the tip by about 10 nm, the signal above the protonated island drops toward zero. In contrast, about 20 nm are required until $\Delta V(z)$ reaches zero above the deprotonated island of *data11*. On the larger deprotonated island in *data10*, the $\Delta V(z)$ signal is still not zero even after tip retraction of 30 nm, indicating an influence of the islands size. This influence is further visualized by the contour plots depicted below, which demonstrate the more negative character of *data10* compared to *data11*. Consequently, the island size of the deprotonated islands seems to have a significant effect on the z-extend of the KPFM signal.

Determination of the Effective Area

The averaging effect of the tip is a well-known effect causing a distance dependence of KPFM data. The KPFM signal has been described as a weighted average of the physical signal and the point-spread-function of the measurement system [149]. The deconvolution has been realized using extensive calculations, which

are beyond the scope of this work. Further studies found that the averaging effect is very pronounced in AM-KPFM, where the cantilever plays a crucial role in the imaging process, while the averaging effect plays only a minor role in FM-KPFM due to a faster decay of the imaging signal [63, 64, 149]. Nevertheless, most distance dependent KPFM studies are done using AM-KPFM, including the only existing distance dependent study of molecules on an insulating surface [156]. To my knowledge, this is the only FM-KPFM study which probes the long-range distance dependence above molecules. As discussed in Chapter 2.3, a comparison to distance dependent AM-KPFM studies is not directly possible. In the following, I study the lateral averaging by analyzing data recorded on differently sized islands and with different distance to the island edge.

Due to the long-range nature of ΔV especially above the deprotonated islands, a large surface area contributes to the signal. If the KPFM signal is only determined by one species, the center of the island as visualized in the slices should have a plateau. This is the case for the protonated islands (Fig. 8.10 (b)). In contrast, the deprotonated islands in *data10* and *data11* do not show a plateau (contour plots Fig. 8.8 (b) and Fig. 8.10 (a)). As the deprotonated island in *data11* is 15 nm to 20 nm wide, the one in *data10* 40 nm, 20 nm distance to the island edge of a deprotonated island are not sufficient for the KPFM signal to be unaltered by the surroundings of the island, *i.e.*, a surface area with a radius larger 20 nm contributes to $\Delta V_{depr}(z)$. This fits nicely to the z-extension of the signal as also $\Delta V_{depr}(z = 20 \text{ nm}) \neq 0$.

For further evaluation, curves of up to 100 nm z-range were acquired. Comparisons between many long-range curves acquired on deprotonated islands reveal a minimum edge distance of about 35-40 nm to yield $\Delta V(z)$ curves that are identical within the noise limit, *i.e.*, curves being unaffected by the island edges.

Fig. 8.11 shows (a) several $\Delta V(z)$ curves, (b) the corresponding positions at which the curves were recorded and (c) an analysis of the area covered by deprotonated molecules around the curve position. To obtain these areas, circles with different radii were drawn around the curve position and the area covered by deprotonated molecules within the circle was evaluated using a

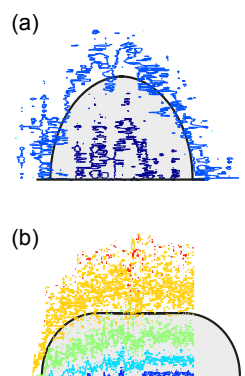
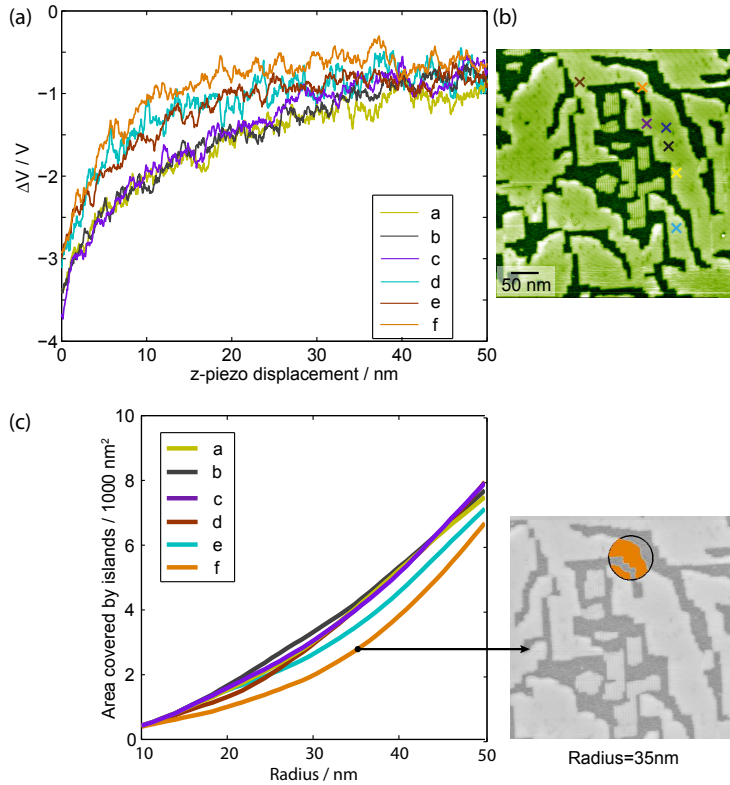


Figure 8.10: (a) Contour of deprotonated island (*data10*). (b) Contour of protonated island (*data12*).

Figure 8.11: (a) Long-range curves acquired at six different positions a-f. (b) Corresponding positions, where the curves a-f were recorded. (c) Evaluation of the area covered by deprotonated islands in a circle around the curve position plotted versus the radius of the circle. The image at the right side illustrates the origin of each data point in the curve: A circle with the respective radius is drawn around the curve's position. A threshold criterion is used to evaluate the area within this circle covered by a molecular island. This procedure is repeated for radii from 10 to 50 nm. Afterward it was checked that no protonated molecules are within the circles. The Matlab code was provided by Philipp Rahe.



threshold criterion in the z-channel. A varied radius was chosen, as firsthand the effective measured area was unknown due to the unknown tip geometry.

The curves in Fig. 8.11 (a) consist of two groups, with the light brown, the dark brown and the turquoise curves being less negative compared to the rest. Consequently, the occupied areas around these three curves are expected to differ. This clearly is observed for the area in Fig. 8.11 (c) of the light brown curve and maybe the turquoise curve. The area around the dark brown curve cannot be clearly distinguished. Consequently, the area around the curve position occupied by deprotonated molecules is one criterion for the quantitative shape of the curve. Further agreement might be reached if a weighting is applied to the area to take into account closer areas more strongly than those further away. Slight differences observed above different deproto-

nated islands might also be due to defects in the islands, which vary the charge state of the island.

In summary, the 2D-KPFS data clearly visualize a long-range behavior, which is different on the different substrate features. Unexpectedly, bare calcite areas show a long-range distance dependence pointing to the existence of charges in the tip-sample system. As expected, protonated and deprotonated 2,5-DBHA islands exhibit a long-range distance dependent KPFM signal. What is even more, the signals above the differently charged molecular islands are distinctly different for a wide z -range. Above the deprotonated islands the long-range character of $\Delta V(x, z)$ results in significant lateral averaging, which is present up to 40 nm from the island edge. In the following section, I analyze curves with a z -range of up to 100 nm to discuss the shape of the distance dependence more quantitatively.

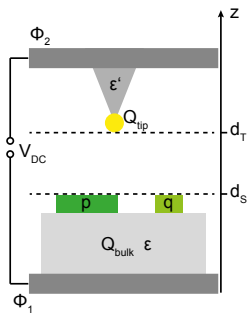


Figure 8.12: Sketch of the tip-sample system with included charges and dipoles.

8.4 Long-Range Curves: Shape of the Distance Dependence

In the previous section, I demonstrated that 2D-KPFS data is sensitive to a distinctly different long-range distance dependence on protonated islands, deprotonated islands and also the bulk insulating substrate. In the following, I compare starting values and curvature of individual curves with a z -range of up to 100 nm within the aim to give a more quantitative description.

Long-Range Electrostatics

The electrostatics of 2,5-DHBA/calcite are determined by the contact potential difference between tip and backelectrode $\Phi_1 - \Phi_2$, local charges and local dipoles (see also Chapter 2.3). Further, the applied voltage V_{DC} needs to be considered.³ Fig. 8.12 shows a sketch of the tip-sample system. The following polarizable materials can be present in the system:⁴

- The tip cone might be (partly) covered by a dielectric material with relative permittivity ϵ' .
- The dielectric bulk has a relative permittivity ϵ .

Besides, the following local charges can be present in the system:

- charges at the tip Q_{tip}
- charges in the bulk calcite Q_{bulk}
(This term includes charges on the calcite surface but excludes charges present in the adsorbates.)
- charged molecular islands q

³Additional effects by the AC modulation voltage are neglected here.

⁴An induced dipole due to the polarizability of the molecular islands is neglected, instead a static dipole is considered.

- molecular islands with static dipoles p

According to Kantorovich et al. [67, 68] the effective electrostatic energy can be described by (see also Chap. 2.3):

$$\begin{aligned}
 W_{eff} = & - \frac{1}{2} CV^2 + \sum_i q_i \phi^0(\vec{r}_i) \\
 & + \frac{1}{2} \sum_{i,j} q_i \phi_{ind,j}(\vec{r}_i, \vec{r}_j) + \sum_{\substack{i,j, \\ i \neq j}} q_i \phi_{coul,j}(\vec{r}_i, \vec{r}_j) \quad (8.1)
 \end{aligned}$$

In this expression, the first term describes the capacitive interaction without local charges. The second term describes the interaction of local charges with the potential of the uncharged capacitor. The third term represents the interaction of a charge q_i with the image charge potential produced by q_j . Finally, the Coulomb energy of the local charges interacting with each other is included.

It can safely be assumed (see also Chap. 2.3 and [61, 69]) that only the first two terms depend on the applied bias V_{DC} .⁵ Because of the KPFM condition $\partial F/\partial V = 0$ ⁶ only these components are relevant for the KPFM signal. Therefore, the effective energy is a sum of terms relevant for the KPFM signal W_{kpfm} and terms W_F that do not depend on the bias: $W_{eff} = W_{kpfm} + W_F$. Considering the charge distributions in the system (for simplicity I consider point charges), the energy relevant for determining the KPFM signal can be written as:

$$W_{kpfm} = - \frac{1}{2} CV^2 \quad (8.2)$$

$$\begin{aligned}
 & + Q_{tip} \phi^0(\vec{r}_{Qtip}) + Q_{bulk} \phi^0(\vec{r}_{Qbulk}) \\
 & + q \phi^0(\vec{r}_q) + q_+ \phi^0(\vec{r}_+) + q_- \phi^0(\vec{r}_-) \quad (8.3)
 \end{aligned}$$

⁵Further assumptions are that the partial derivatives with respect to V and d and any integrals describing the charge distributions are commutative.

⁶This condition is directly valid for AM-KPFM, where the force is directly measured. In FM-KPFM Δf is measured and the complete condition is $\partial \Delta f/\partial V = 0$. To extract the force from Δf , the integration in [43] needs to be solved. As the integration is along z , V can be factored out and the terms will slightly differ from the case of $\partial F/\partial V = 0$ (see also [61]). As here only the existence of terms is discussed not their quantitative values, the simpler condition is adequate.

Here, I consider the molecular dipole as the sum of a positive and a negative charge at slightly different positions. If the capacitance C and the potential ϕ^0 are known, the KPFM signal can be calculated. Each of these terms will lead to a contribution to the KPFM signal (see also Chap. 2.3):

$$\begin{aligned} \frac{\partial^2 W_{kpfm}}{\partial V \partial z} = & + \Delta V_{CPD} \\ & + \Delta V_{Qtip} + \Delta V_{Qbulk} \\ & + \Delta V_q + \Delta V_p \end{aligned} \quad (8.4)$$

When the tip only interacts with one type of molecular island (which is assumed to be valid when measuring above the center of a large molecular island), the contributions to the KPFM signal above specific substrate features can be written as follows: KPFM signal above calcite:

$$\Delta V_{calcite} = \Delta V_{CPD} + \Delta V_{Qtip} + \Delta V_{Qbulk} \quad (8.5)$$

KPFM signal above charged molecular islands adsorbed on calcite:

$$\Delta V_{q-on-calcite} = \Delta V_{CPD} + \Delta V_{Qtip} + \Delta V_{Qbulk} + \Delta V_q \quad (8.6)$$

KPFM signal above dipole molecular islands adsorbed on calcite:

$$\Delta V_{p-on-calcite} = \Delta V_{CPD} + \Delta V_{Qtip} + \Delta V_{Qbulk} + \Delta V_p \quad (8.7)$$

Subtracting the calcite background results in the effective signals above the molecular islands:⁷

$$\Delta V_{q,eff} = \Delta V_{q-on-calcite} - \Delta V_{calcite} = \Delta V_q \quad (8.8)$$

$$V_{p,eff} = \Delta V_{p-on-calcite} - \Delta V_{calcite} = \Delta V_p \quad (8.9)$$

⁷Here, I assume that the polarizability of the molecules does not influence the potential ϕ^0 . If the polarizability influences ϕ^0 , $\Delta V_{calcite}$ will be different above the bare substrate and above the molecular islands.

The KPFM signal above all substrate features is determined by the potential ϕ^0 , *i.e.*, the distance dependence of all components is described by the same potential.⁸ On the surface, all charges interact with $\phi^0(r_{surface})$. As there is no coupling terms between the charges, a difference in distance dependence just follows from the sum over all the contributions due to the molecular island. On a dipole island, every two contributions have opposite sign, while all contributions have equal sign on a monopole island. Thus, the KPFM signal above the dipole islands is expected to decay faster than above the monopole islands.⁹

For a quantitative description of the KPFM signal, (only) ϕ^0 and C , which are determined by the real tip-sample geometry without local charges, need to be known. A simple analytical solution is only available for a sphere in front of a metal plate ([27]) or a dielectric halfspace [62]. For a realistic tip-sample system, finite elements methods like in [63] need to be applied, which is beyond the scope of this work. Still, the above considerations give a reasoning why subtracting the calcite background is feasible.

Fig. 8.13 (a) and (b) show typical long-range curves acquired with two different tips above calcite, protonated islands and deprotonated islands. In subfigure (a), several curves are presented recorded with *tip2* superimposed with the average curves. Subfigure (b) displays two curves for each substrate feature acquired with *tip3*. All curves resemble an inverse power law. At large z -range all curves share the same ΔV , which I ascribe to the macroscopic tip-sample system, *i.e.*, $\Delta V(z > 60nm) = \Delta V_{CPD}$ with differing absolute values for the two tips.¹⁰

⁸The potential might be defined in sections. Thus, charges on the tip, in the bulk and on top of the surface might not be described by a potential with the same distance dependence, while different molecular islands on the surface are expected to be described by the same potential.

⁹As the fate of the proton is unknown for the deprotonation of 2,5-DHBA on calcite, it cannot be excluded that the proton is still in the vicinity of the deprotonated molecule. In this case, the island would not be composed of charges of equal sign, but consist of dipoles. These dipoles are expected to be stronger than the ones formed by the protonated molecules as the charge is $1e$ and the separation is larger than the molecule's extension.

¹⁰This offset might not be solely due to the work function difference of the back-electrodes, but charges in the tip or the sample might contribute. Depending on their position, they might not induce a distance dependence but instead

Due to this offset, the values for $\Delta V(z = 0 \text{ nm} = z_0)$ differ for the different tips. For *tip2* in Fig. 8.13 (a), they are $\Delta V_{\text{calcite}}(z_0) \approx 1\text{V}$, $\Delta V_{\text{prot}}(z_0) \approx 0\text{V}$ and $\Delta V_{\text{depr}}(z_0) \approx -1\text{V}$. For *tip3* in Fig. 8.13 (b) they are $\Delta V_{\text{calcite}}(z_0) \approx -1\text{V}$, $\Delta V_{\text{prot}}(z_0) \approx -2\text{V}$ and $\Delta V_{\text{depr}}(z_0) \approx -3\text{V}$. Thus, the starting values follow the trend:

$$\Delta V_{\text{calcite}}(z_0) > \Delta V_{\text{prot}}(z_0) > \Delta V_{\text{depr}}(z_0) .$$

Furthermore the distance z_{CPD} , at which the curves reach the asymptotic value ΔV_{CPD} , differs for the different substrate features. These distances are approximately $z_{\text{CPD}}^{\text{calcite}} \approx 10 \text{ nm}$,¹¹ $z_{\text{CPD}}^{\text{prot}} \approx 20 \text{ nm}$ and $z_{\text{CPD}}^{\text{depr}} \approx 60 \text{ nm}$. Thus

$$z_{\text{CPD}}^{\text{calcite}} < z_{\text{CPD}}^{\text{prot}} < z_{\text{CPD}}^{\text{depr}} .$$

In between, the shape of the curves resembles an inverse power law¹² with the curvatures b in the range of $[z_0, z_{\text{CPD}}]$ ordering as:

$$b_{\text{calcite}} > b_{\text{prot}} > b_{\text{depr}} .$$

This order seems plausible. The presumably dilute distribution of single charges in the calcite crystal and on the tip result in the lowest absolute value and the largest curvature. As the charges in the molecular islands are more densely packed, larger deviations and smaller curvatures are expected. For the protonated islands, which are composed of the same number of positive and negative charges, a smaller absolute value and a larger curvature is expected than for the deprotonated islands presumably only composed of negative charges.

In a next step, the calcite background is subtracted to separate the local contributions (see Eq. 8.8 and 8.9). After this procedure, the KPFM signal should only be determined by the interaction of the adsorbed molecules with the potential field of the capacitor. Fig. 8.13 (c) and (d) show the same curves as in (a) and (b) but after calcite subtraction. Due to this procedure the curves acquired with different tips resemble strongly. To visualize this effect, Fig. 8.14 shows the averages plotted in the same

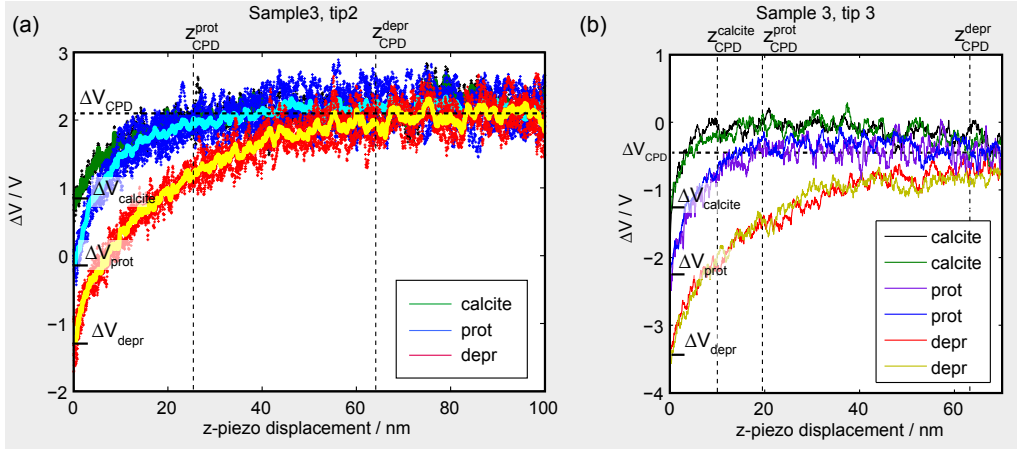
lead to an offset.

¹¹The curves on calcite in Fig. 8.13 (a) were recorded close to molecular islands and are possibly slightly influenced by these.

¹²Due to the large number of unknown parameters, fit equations are overdetermined, so that a more specific model is needed to extract the curvatures.

8.4 Long-Range Curves: Shape of the Distance Dependence

raw data



data minus calcite background

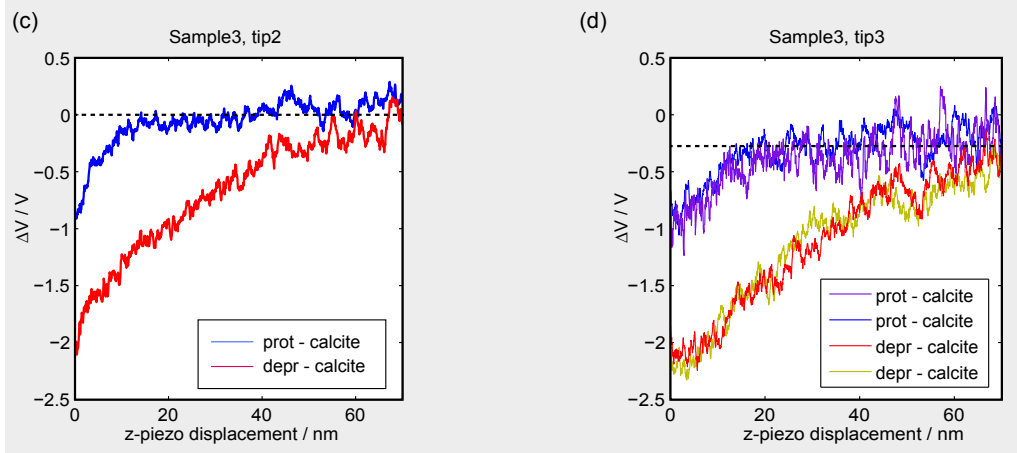
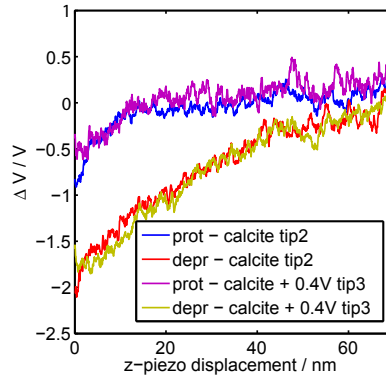
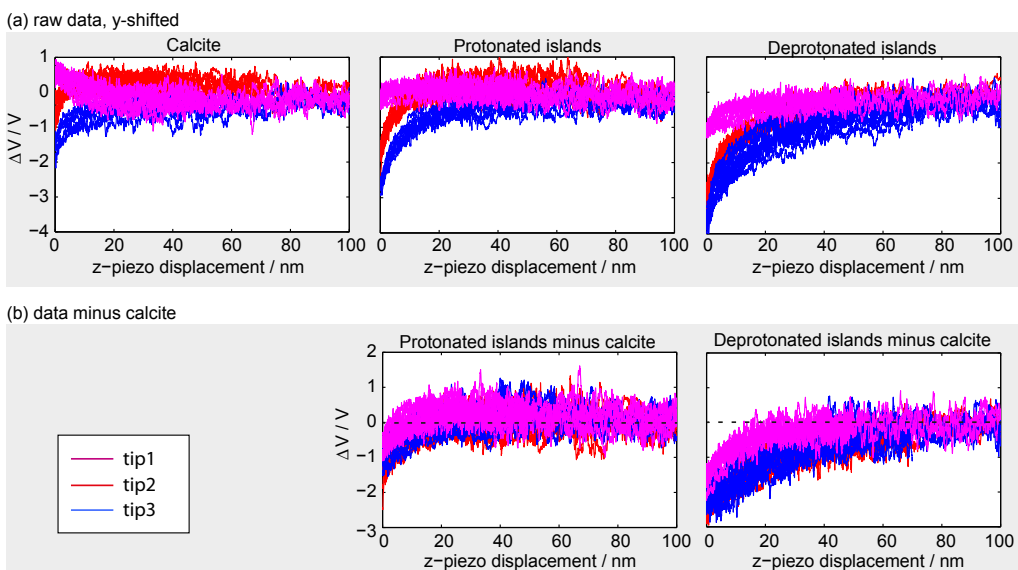


Figure 8.13: Typical long-range curves acquired on *sample3* with (a) *tip2* and (b) *tip3*. (c) and (d) show the curves after calcite background subtraction. 139

Figure 8.14: Averages from Fig. 8.13 after background subtraction. An offset of 0.4 V was added to the curves recorded with tip 3. After background subtraction and adding this offset, the curves acquired with the different tips appear identical within the noise limit.



graph. Their shape is identical within the noise limit. However, the curves for tip3 were offset by 0.4 V for the asymptotic value to reach zero. The reason for this offset (which results from $\Delta V_{CPD}^{molecule} \neq \Delta V_{CPD}^{calcite}$) is unknown. A charging of the tip over time resulting in a different tip state for calcite and molecular island curves, can be excluded as the curves on calcite and on the molecular islands were acquired in random order. A large surface area is expected to determine V_{CPD} . If this area is occupied by more deprotonated molecules, which show a longer-range contribution to the signal, a shift of V_{CPD} could be imagined. This effect might be enhanced if the tip segment contributing to the signal differs significantly for calcite and deprotonated islands. Except for an offset, background subtraction cancels the effect of different tips (A comparison of more curves is presented in the paragraph Tip Influence): Curvatures and z_{CPD} are independent of the tip. Thus, they can be attributed to characteristics of the surface features. Compared to the raw data, the curvatures after background subtraction are less pronounced and appear nearly linear. To quantitatively understand the shape of these curves, knowledge about the potential of the capacitor and its distance dependence is required.



Tip Influence

In the following, I address the influence given by different tips on the long-range curves. As calcite background subtraction yielded nearly identical curves in Fig. 8.13, this effect demands further investigation.

Fig. 8.15 shows long-range curves acquired with three different tips at sufficient distance to the island edges. Panel (a) shows the raw $\Delta f(z)$ data on calcite, protonated islands and deprotonated islands, respectively. For better comparison, the curves were shifted along the ΔV -axis to reach the same asymptotic value. Curves recorded with the same tips are plotted using the same color. The quantitative shape of the curves is clearly tip-dependent. Most surprisingly, one tip even shows a curvature of opposite sign on calcite. Qualitatively, though, all curves resemble the findings from before, *i.e.*, the trends of $\Delta V(z_0)$, z_{CPD} and b are tip-independent. In a second step, I subtract again the respective calcite background curve from the molecular data; results are shown in Fig. 8.15 (b) for the protonated and deprotonated islands, respectively. Most interestingly, this strategy

Figure 8.15: $\Delta V(z)$ curves with a z -range > 50 nm for three different tips (plotted using different colors). (a) shows the curves shifted such that ΔV_{CPD} is the same. (b) shows the curves on the molecular islands after subtracting respective calcite curves.

results in virtually identical curves for the protonated islands. The remaining spread is comparable to the already present one when using a single tip and may result from a varying tip apex or slightly different surface contributions.

For the deprotonated islands, the curves still exhibit differences, though these are smaller when compared to the raw data. Due to the longer-range character of the deprotonated islands, a larger part of the tip is expected to contribute to the signal, *i.e.*, shape and composition of the tip are expected to have a larger influence. Moreover, the tip segment contributing might differ from the one contributing to the shorter-ranged calcite curves.

The same trend is visible in averages of the curves (not shown). Thus, a quantitative description of the raw data is difficult due to the unknown tip characteristics, calcite subtraction, however, allows for a quantitative description independent of the used tip.

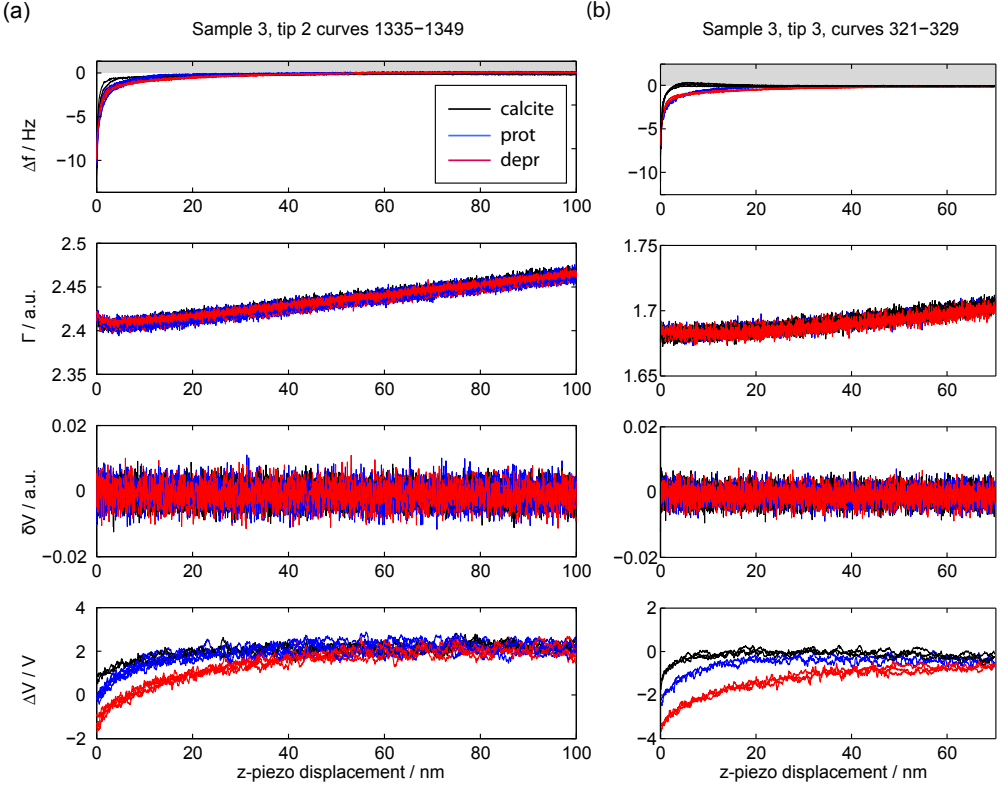
Further, a comparison of all curves acquired with one tip but on two different samples shows no difference for the two samples. Consequently, the overall coverage is not important for the shape of the curves. The surroundings at a specific position might have an influence such as the offset seen in Fig. 8.14. Furthermore, the spread of the curves and the noise level of ΔV_{CPD} is larger than the offset of 0.4 V in Fig. 8.14.

Long-Range Van-Der-Waals

Besides the distinct difference in $\Delta V(z)$, the different surface features also show a difference in the long-range frequency shift signal. Fig. 8.16 shows additional data channels, namely $\Delta f(z)$, $\Gamma(z)$ and $\delta V(z)$, of the same curves as in Fig. 8.13. Except for the previously described increase in $\Gamma(z)$, both, $\Gamma(z)$ and $\delta V(z)$, display noise. $\Delta f(z)$ has a pronounced long-range character, which, interestingly, differs for the different surface features also in present case, where the electrostatic interaction is minimized. On calcite, $\Delta f(z)$ reaches zero¹³ faster than on the molecular islands, while the differently charged molecular islands influence $\Delta f(z)$ in the same way. One possible explanation might be the ef-

¹³A small offset in Δf was attributed to a slight change in the eigenfrequency and was corrected.

8.4 Long-Range Curves: Shape of the Distance Dependence



fect of the modulation voltage on the force (Chap. 2.3, Eqn. 2.13):

$$F_{el,DC} = \frac{1}{2} \frac{\partial C}{\partial z} \left[\left(V_{DC} - \frac{\Delta\Phi}{e} \right) - \frac{V_{AC}^2}{2} \right] \quad (8.10)$$

Due to the modulation voltage, $F_{el,DC}$ has an additional component $\neq 0$ if $\frac{\partial C}{\partial z} \neq 0$. This fact would readily explain a long-range signal in the Δf channel. However, $\partial C / \partial z$ has to be different on calcite and the molecular islands to additionally explain the difference in the $\Delta f(z)$ on these two sample sites. This might be the case, if the polarizability of the molecules has a strong effect on the capacitance. If this is not the reason, and electrostatic forces are completely compensated for as suggested by the error signal, another long-range force component has to be present which is

Figure 8.16: Additional channels for the same long-range curves as shown in Fig. 8.13 with (a) *tip2* and (b) *tip3*. The different substrate features are not only visible in $\Delta V(z)$, but $\Delta f(z)$ differs for calcite and the molecular islands.

not of electrostatic origin. The difference might be attributed to van-der-Waals forces. Such an assignment seems plausible as weaker van-der-Waals interactions are expected from bare calcite than from calcite with an additional molecular island. As the slight difference in the molecular stacking of the two molecular islands, is not expected to effect the van-der-Waals forces originating from the molecules at larger distances significantly, the similar signal above the molecular islands could also be understood. Thus, in a very simple picture, the difference in the force measured by Δf between calcite and molecular islands might originate from the van-der-Waals interactions of the molecules. Consequently, the possibility to separate electrostatic and van-der-Waals contributions by z-spectroscopy with engaged KPFM controller allows not only to investigate the electrostatic interactions of a system but also the long-range van-der-Waals interactions of different substrate features.

In summary, the analysis of long-range curves leads to the following conclusions: The starting values of the long-range $\Delta V(z)$ curves order as $\Delta V_{calcite}(z_0) > \Delta V_{prot}(z_0) > \Delta V_{depr}(z_0)$. Their range shows the same order: $z_{CPD}^{calcite} < z_{CPD}^{prot} < z_{CPD}^{depr}$. The shape of the raw data follows an inverse power law with the curvatures $b_{calcite} > b_{prot} > b_{depr}$. For different tips, the quantitative shape differs. After calcite background subtraction, however, the data recorded with different tips are practically identical over the protonated islands and resemble strongly over the deprotonated islands, justifying the assumption of additivity and allowing for a quantitative description. Due to background subtraction the shape of the curves changes and their curvatures are weaker pronounced. This shape will be further investigated in a cooperation with **[Personal data removed]**.

The long-range KPFS measurements do not only give insight into the electrostatic interactions but separate electrostatic and van-der-Waals interactions. The van-der-Waals interactions show a long-range behavior. Even more, this behavior differs on calcite and on the molecular islands, so that such an approach can be used to measure the van-der-Waals interactions of adsorbed molecular assemblies.

8.5 Conclusions

To conclude, I explored 2,5-DHBA on calcite (10.4) as a model system to study the long-range distance dependence of the KPFS signal caused by monopole (deprotonated 2,5-DHBA) and dipole (protonated 2,5-DHBA) arrangements on a bulk insulator.

Charges are expected to induce a distance dependence to the KPFS signal. The KPFS signal of an assembly of charges is expected to be determined by a sum of contributions due to the single charges. Indeed, 2D KPFS measurements reveal a long-range behavior with a range of up to 50 nm, which is distinctly different above the different molecular islands. Also bare calcite shows long-range variations in the KPFS signal pointing at the existence of local charges in the calcite bulk or on the tip. For the molecular islands, dipole interactions were found to be not as long-ranged as the interactions from monopoles in agreement with a simple electrostatic picture. The long-range nature of the signal above the deprotonated islands leads to significant lateral averaging. A relation between the effective island size and the KPFS signal magnitude was evident for selected sample positions.

The tip shape is known to play an important role on the long-range Kelvin probe signal. Here, the qualitative trends for the different surface features are the same for all tips, while the quantitative shape of the curves depends on the specific tip. Remarkably, most of these differences cancel upon subtraction of the calcite background, allowing to study surface features quantitatively independent of the probe tip. The resulting curves on the molecular islands after background subtraction will be investigated further in a cooperation with theory.

The long-range distance-dependent measurements do not only give insight into the electrostatics but separate electrostatic and van-der-Waals interactions. Consequently, such measurements also give access to the van-der-Waals interactions of molecular assemblies. Quite reasonably, the interactions above molecular islands were found to be stronger than above bare calcite regions.

9 Summary

In this thesis, I report on the molecular self-assembly of benzoic acid derivatives on calcite (10.4) at room temperature studied by nc-AFM in UHV. The influence of small variations at the molecular building block on the structure formation was systematically investigated. As motivated in Chapters 3 and 4, I chose dihydroxybenzoic acid (DHBA) as starting molecule for the formation of hydrogen-bonded networks on calcite.

In Chap. 5, I discussed how the positions of the hydroxyl groups steer the molecular self-assembly. The six constitutional isomers of DHBA form six different structures on the surface, only two of which are stable. The substitution positions affect the structure formation in three distinct aspects, namely the deprotonation tendency of the DHBA molecule, the intermolecular interaction and the molecule-surface matching. Positioning the hydroxyl groups closely to the carboxyl group favors deprotonation and, thereby, influences the type of molecule-substrate interaction. The distribution of the hydroxyl groups around the benzene core determines how many opportunities for intermolecular interaction are available. The specific position of each functional group is crucial for the match with the calcite surface.

The influence of the number of functional groups at the molecule is analyzed in Chap. 6 by using the only stable and substrate-templated structure formed by protonated DHBA as reference, namely 3,5-DHBA. Both, 3,5-DHBA and 3-HBA, form extended stripes along the $[4\bar{2}.1]$ direction, with the same adsorption pattern in nc-AFM images. Monitoring the stripes over many hours revealed a significant diffusivity of the 3-HBA stripes. More-

over, a mesoscopic ordering was found: 3-HBA stripes arrange equidistantly with coverage-dependent distance. Similar arrangements have so far been observed on metals which exhibit a surface state.

Removing one hydroxyl group, thus, changes (a) the mobility of the molecules and (b) introduces a mesoscopic ordering. The change in mobility is straightforward to understand, as 3,5-DHBA can form an additional hydrogen bond towards the substrate. The mesoscopic order was analyzed in detail and is currently investigated by calculations to fully understand its origin.

The influence of the type of the hydrogen donating functional groups on the hydrogen-bonded networks was investigated in Chap. 7.

First, I compared hydroxyl and amino groups by a comparison of 3-HBA and 3-ABA. Both molecules show the same adsorption pattern and the same long-range order.

A greater variation is achieved by switching between benzoic acids and benzamides, in which case I observed a transition from one-dimensional to two-dimensional growth. For 3-HBA and 3-HBA, *i.e.*, benzene with two functional groups, the two-dimensional and one-dimensional patterns differ strongly. In the case of three functional groups for 3,5-DHBA and 3,5-DHBA, the two-dimensional islands are composed of stripes resembling the one-dimensional pattern. Quite plausible, the influence of changing a functional group is stronger with smaller number of interacting functional groups. In all cases, the hydrogen-bonded networks are more stable with oxygen containing groups than with nitrogen containing groups, following the trend of the stronger electronegativity.

Interestingly, both amides show similarly strong, positive KPFM contrast despite their completely different arrangement. This opposite sign of the KPFM contrast compared to carboxylic acids like 2,5-DHBA implies a different charge distribution, which might indicate a different electrostatic contribution to the molecule-substrate interaction.

In Chap. 8, I explored 2,5-DHBA on calcite (10.4) as a model system to study the long-range distance dependence of the KPFS signal caused by monopole (deprotonated 2,5-DHBA) and dipole (protonated 2,5-DHBA) arrangements on an insulating substrate.

2D KPFS measurements reveal a long-range contrast, which is distinctly different above the different molecular islands. Besides, the monopole islands show pronounced lateral averaging, which has been related to the effective islands size.

I demonstrated how subtraction of the calcite background effectively cancels the effect of the probe tip. Thus, background subtraction allows to study the signal caused by the monopole and dipole arrangements adsorbed on calcite quantitatively. The resulting shape of the curves is now investigated further in cooperation with theory.

In conclusion, hydrogen-bonded networks composed of molecules on an insulating substrate can be adjusted by only slightly altering the molecular building block. Positioning functional groups in a rational manner provides plenty of opportunities for tuning the structure formation over a wide range from mobile molecules and metastable patterns to strongly substrate-templated, one- or two-dimensional, stable structures. The detachment of a single functional group can have significant influence, not only on the structure formation but also on the mesoscopic order of the arrangement. If chosen properly, slight changes in the type of the functional groups can either be used for functionalization purposes without changing the self-assembly properties or to deliberately switch, *e.g.*, between one-dimensional and two-dimensional patterns. Finally, long-range electrostatic forces can be present and, thus, charging effects need to be considered for self-assembled structures on an insulating substrate.

Bibliography

- [1] G. M. WHITESIDES: Self-Assembly at All Scales.
Science **295**, 2418 (2002)
- [2] G. M. WHITESIDES, J. P. MATHIAS, C. T. SETO: Molecular self-assembly and nanochemistry: a chemical strategy for the synthesis of nanostructures.
Science **254**, 1312 (1991)
- [3] J.-M. LEHN: Toward Self-Organization and Complex Matter.
Science **295**, 2400 (2002)
- [4] J.-M. LEHN: Supramolecular Chemistry—Scope and Perspectives Molecules, Supermolecules, and Molecular Devices (Nobel Lecture).
Angew. Chem. Int. Ed. **27**, 89 (1988)
- [5] J. V. BARTH: Molecular Architectonic on Metal Surfaces.
Annu. Rev. Phys. Chem. **58**, 375 (2007)
- [6] P. RAHE, M. KITTELMANN, J. L. NEFF, M. NIMMRICH, M. REICHLING, P. MAASS, A. KÜHNLE: Tuning Molecular Self-Assembly on Bulk Insulator Surfaces by Anchoring of the Organic Building Blocks.
Adv. Mater. **25**, 3948 (2013)
- [7] P. RAHE, M. NIMMRICH, A. KÜHNLE: Substrate Templating upon Self-Assembly of Hydrogen-Bonded Molecular Networks on an Insulating Surface.
Small **8**, 2969 (2012)
- [8] M. LACKINGER, W. M. HECKL: Carboxylic Acids: Versa-

- tile Building Blocks and Mediators for Two-Dimensional Supramolecular Self-Assembly.
Langmuir **25**, 11307 (2009)
- [9] E. MEYER, H. J. HUG, R. BENNEWITZ: Scanning probe microscopy: The lab on a tip. Berlin : Springer, 2004
- [10] G. BINNIG, H. ROHRER, C. GERBER, E. WEIBEL: Surface Studies by Scanning Tunneling Microscopy.
Phys. Rev. Lett. **49**, 57 (1982)
- [11] G. BINNIG, C. F. QUATE, C. GERBER: Atomic Force Microscope.
Phys. Rev. Lett. **56**, 930 (1986)
- [12] M. NONNENMACHER, M. P. O'BOYLE, H. K. WICKRAMASINGHE: Kelvin probe force microscopy.
Appl. Phys. Lett. **58**, 2921 (1991)
- [13] F. MOHN, L. GROSS, N. MOLL, G. MEYER: Imaging the charge distribution within a single molecule.
Nat. Nanotechnol. **7**, 227 (2012)
- [14] MORITA, S, (Hrsg.), WIESENDANGER, R, (Hrsg.), MEYER, E, (Hrsg.): Noncontact Atomic Force Microscopy. Berlin, Heidelberg : Springer, 2002
- [15] J. N. ISRAELACHVILI: Intermolecular and surface forces. 3. ed. Amsterdam : Elsevier, Acad Press, 2011
- [16] F. J. GIESSIBL: Advances in atomic force microscopy.
Rev. Mod. Phys. **75**, 949 (2003)
- [17] J. E. LENNARD-JONES: Cohesion.
P. Phys. Soc. **43**, 461 (1931)
- [18] W. H. KEESOM: Die van derWaalsschen Kohäsionskräfte.
Phys. Z. **22**, 129 (1921)
- [19] DEBYE, P. J. W.: Polar Molecules. New York : Chemical Catalog Co., 1929

- [20] F. LONDON: Zur Theorie und Systematik der Molekularkräfte.
Zeitschrift für Physik **63**, 245 (1930)
- [21] H. C. HAMAKER: The London—van der Waals attraction between spherical particles.
Physica **4**, 1058 (1937)
- [22] W. ALLERS, A. SCHWARZ, U. D. SCHWARZ, R. WIESEN-DANGER: Dynamic scanning force microscopy at low temperatures on a van der Waals surface: graphite (0001).
Appl. Surf. Sci. **140**, 247 (1999)
- [23] H. HÖLSCHER, W. ALLERS, U. D. SCHWARZ, A. SCHWARZ, R. WIESENDANGER: Interpretation of “true atomic resolution” images of graphite (0001) in noncontact atomic force microscopy.
Phys. Rev. B **62**, 6967 (2000)
- [24] S. KUHN, P. RAHE: Discriminating short-range from van der Waals forces using total force data in noncontact atomic force microscopy.
Phys. Rev. B **89**, 235417 (2014)
- [25] M. REICHLING, C. BARTH: Scanning Force Imaging of Atomic Size Defects on the CaF₂(111) Surface.
Phys. Rev. Lett. **83**, 768 (1999)
- [26] F. GIESSIBL: Theory for an electrostatic imaging mechanism allowing atomic resolution of ionic crystals by atomic force microscopy.
Phys. Rev. B **45**, 13815 (1992)
- [27] S. HUDLET, M. SAINT JEAN, B. ROULET, J. BERGER, C. GUTHMANN: Electrostatic forces between metallic tip and semiconductor surfaces.
J. Appl. Phys. **77**, 3308 (1995)
- [28] T. R. ALBRECHT, P. GRÜTTER, D. HORNE, D. RUGAR: Frequency modulation detection using high-Q cantilevers

- for enhanced force microscope sensitivity.
J. Appl. Phys. **69**, 668 (1991)
- [29] F. J. GIESSIBL: Forces and frequency shifts in atomic-resolution dynamic-force microscopy.
Phys. Rev. B **56**, 16010 (1997)
- [30] P. RAHE, J. SCHÜTTE, W. SCHNIEDERBEREND, M. REICHLING, M. ABE, Y. SUGIMOTO, A. KUHNLE: Flexible drift-compensation system for precise 3D force mapping in severe drift environments.
Rev. Sci. Instrum. **82**, 063704 (2011)
- [31] P. RAHE, R. BECHSTEIN, J. SCHÜTTE, F. OSTENDORF, A. KÜHNLE: Repulsive interaction and contrast inversion in noncontact atomic force microscopy imaging of adsorbates.
Phys. Rev. B **77**, 195410 (2008)
- [32] J. V. LAURITSEN, A. S. FOSTER, G. H. OLESEN, M. C. CHRISTENSEN, A. KÜHNLE, S. HELVEG, J. R. ROSTRUP-NIELSEN, B. S. CLAUSEN, M. REICHLING, F. BESENBACHER: Chemical identification of point defects and adsorbates on a metal oxide surface by atomic force microscopy.
Nanotechnology **17**, 3436 (2006)
- [33] N. W. ASHCROFT, N. D. MERMIN: *Solid state physics*. 30. print. Singapore : Brooks/Cole, 2003
- [34] KELVIN: V. Contact electricity of metals.
Philos. Mag. 5 **46**, 82 (1898)
- [35] S. HÜFNER: *Photoelectron spectroscopy: Principles and applications*. 3., rev. and enl. ed. Berlin : Springer, 2003
- [36] SADEWASSER, S. (Hrsg.) , GLATZEL, T. (Hrsg.): *Kelvin probe force microscopy: Measuring and compensating electrostatic forces*. Bd. 48. Heidelberg : Springer, 2012
- [37] M. J. KITTELMANN: *On-surface chemical reactions on*

- an insulating substrate. Mainz, Johannes Gutenberg-Universität, PhD thesis, 2013
- [38] S. KITAMURA, M. IWATSUKI: High-resolution imaging of contact potential difference with ultrahigh vacuum non-contact atomic force microscope. *Appl. Phys. Lett.* **72**, 3154 (1998)
- [39] T. GLATZEL, S. SADEWASSER, M. LUX-STEINER: Amplitude or frequency modulation-detection in Kelvin probe force microscopy. *Appl. Surf. Sci.* **210**, 84 (2003)
- [40] J. M. R. WEAVER: High resolution atomic force microscopy potentiometry. *J. Vac. Sci. Technol. B* **9**, 1559 (1991)
- [41] A. KIKUKAWA, S. HOSAKA, R. IMURA: Vacuum compatible high-sensitive Kelvin probe force microscopy. *Rev. Sci. Instrum.* **67**, 1463 (1996)
- [42] C. SOMMERHALTER, T. W. MATTHES, T. GLATZEL, A. JÄGER-WALDAU, M. C. LUX-STEINER: High-sensitivity quantitative Kelvin probe microscopy by non-contact ultra-high-vacuum atomic force microscopy. *Appl. Phys. Lett.* **75**, 286 (1999)
- [43] F. J. GIESSIBL, H. BIELEFELDT: Physical interpretation of frequency-modulation atomic force microscopy. *Phys. Rev. B* **61**, 9968 (2000)
- [44] C. BARTH, A. S. FOSTER, C. R. HENRY, A. L. SHLUGER: Recent Trends in Surface Characterization and Chemistry with High-Resolution Scanning Force Methods. *Adv. Mater.* **23**, 477 (2011)
- [45] W. MELITZ, J. SHEN, A. C. KUMMEL, S. LEE: Kelvin probe force microscopy and its application. *Surf. Sci. Rep.* **66**, 1 (2011)
- [46] K. WANDEL: The local work function: Concept and im-

- plications.
Appl. Surf. Sci. **111**, 1 (1997)
- [47] S. SADEWASSER, T. GLATZEL, M. RUSU, A. JÄGER-WALDAU, M. C. LUX-STEINER: High-resolution work function imaging of single grains of semiconductor surfaces.
Appl. Phys. Lett. **80**, 2979 (2002)
- [48] M. BIELETZKI, T. HYNNINEN, T. M. SOINI, M. PIVETTA, C. R. HENRY, A. S. FOSTER, F. ESCH, C. BARTH, U. HEIZ: Topography and work function measurements of thin MgO(001) films on Ag(001) by nc-AFM and KPFM.
Phys. Chem. Chem. Phys. **12**, 3203 (2010)
- [49] C. LOPPACHER, U. ZERWECK, L. M. ENG: Kelvin probe force microscopy of alkali chloride thin films on Au(111).
Nanotechnology **15**, 9 (2004)
- [50] J. LÜ, L. ENG, R. BENNEWITZ, E. MEYER, H.-J. GÜNTHERODT, E. DELAMARCHE, L. SCANDELLA: Surface potential studies of self-assembling monolayers using Kelvin probe force microscopy.
Surf. Interface Anal. **27**, 368 (1999)
- [51] H. SUGIMURA, K. HAYASHI, N. SAITO, O. TAKAI, N. NAKAGIRI: Kelvin Probe Force Microscopy Images of Microstructured Organosilane Self-Assembled Monolayers.
Jpn. J. Appl. Phys. **40**, 4373 (2001)
- [52] C. BARTH, C. R. HENRY: Kelvin probe force microscopy on surfaces of UHV cleaved ionic crystals.
Nanotechnology **17**, 155 (2006)
- [53] H. H. PIEPER, C. BARTH, M. REICHLING: Characterization of atomic step structures on CaF₂(111) by their electric potential.
Appl. Phys. Lett. **101**, 051601 (2012)
- [54] S. A. BURKE, J. M. LEDUE, Y. MIYAHARA, J. M. TOP-

- PLE, S. FOSTNER, P. GRÜTTER: Determination of the local contact potential difference of PTCDA on NaCl: a comparison of techniques.
Nanotechnology **20**, 264012 (2009)
- [55] E. J. SPADAFORA, M. LINARES, NISA YAHYA, WAN ZAIREEN, F. LINCKER, R. DEMADRILLE, B. GREVIN: Local contact potential difference of molecular self-assemblies investigated by Kelvin probe force microscopy.
Appl. Phys. Lett. **99**, 233102 (2011)
- [56] A. HINAUT, A. PUJOL, F. CHAUMETON, D. MARTROU, A. GOURDON, S. GAUTHIER: An NC-AFM and KPFM study of the adsorption of a triphenylene derivative on KBr(001).
Beilstein J. Nanotechnol. **3**, 221 (2012)
- [57] M. KITTELMANN, P. RAHE, A. GOURDON, A. KÜHNLE: Direct Visualization of Molecule Deprotonation on an Insulating Surface.
ACS Nano **6**, 7406 (2012)
- [58] B. HOFF, M. GINGRAS, R. PERESUTTI, C. R. HENRY, A. S. FOSTER, C. BARTH: Mechanisms of the Adsorption and Self-Assembly of Molecules with Polarized Functional Groups on Insulating Surfaces.
J. Phys. Chem. C **118**, 14569 (2014)
- [59] P. RAHE, J. L. NEFF, C. WILLIAMS: KPFM contrast mechanism: ver009. June 16, 2014. – ver009
- [60] J. D. JACKSON, K. MÜLLER: *Klassische Elektrodynamik*. 3., überarb. Aufl. Berlin : de Gruyter, 2002
- [61] C. BARTH, T. HYNINEN, M. BIELETZKI, C. R. HENRY, A. S. FOSTER, F. ESCH, U. HEIZ: AFM tip characterization by Kelvin probe force microscopy.
New J. Phys. **12**, 093024 (2010)
- [62] W. R. SMYTHE: *Static and dynamic electricity*: Chap. 5.

3. ed. New York : McGraw-Hill, 1950

- [63] A. SADEGHI, A. BARATOFF, S. A. GHASEMI, S. GOEDECKER, T. GLATZEL, S. KAWAI, E. MEYER: Multiscale approach for simulations of Kelvin probe force microscopy with atomic resolution. *Phys. Rev. B* **86** (2012)
- [64] U. ZERWECK, C. LOPPACHER, T. OTTO, S. GRAFSTRÖM, L. ENG: Accuracy and resolution limits of Kelvin probe force microscopy. *Phys. Rev. B* **71** (2005)
- [65] U. ZERWECK, C. LOPPACHER, T. OTTO, S. GRAFSTRÖM, L. M. ENG: Kelvin probe force microscopy of C60 on metal substrates: towards molecular resolution. *Nanotechnology* **18**, 084006 (2007)
- [66] C. LOPPACHER, U. ZERWECK, L. M. ENG, S. GEMMING, G. SEIFERT, C. OLBRICH, K. MORAWETZ, M. SCHREIBER: Adsorption of PTCDA on a partially KBr covered Ag(111) substrate. *Nanotechnology* **17**, 1568 (2006)
- [67] L. N. KANTOROVICH, A. I. LIVSHITS, M. STONEHAM: Electrostatic energy calculation for the interpretation of scanning probe microscopy experiments. *J. Phys.: Condens. Matter* **12**, 795 (2000)
- [68] L.N. KANTOROVICH, A.S. FOSTER, A.L. SHLUGER, A.M. STONEHAM: Role of image forces in non-contact scanning force microscope images of ionic surfaces. *Surf. Sci.* **445**, 283 (2000)
- [69] T. HYNINEN, A. S. FOSTER, C. BARTH: Polarized Tips or Surfaces: Consequences in Kelvin Probe Force Microscopy. *e-Journal Surf. Sci. Nanotechnol.* **9**, 6 (2011)
- [70] R. BECHSTEIN: Pristine and Doped Titanium Dioxide

- Studied by NC-AFM. Osnabrück, Universität, PhD thesis, 2009
- [71] J. SCHÜTTE: Abbildung organischer Moleküle auf dielektrischen Oberflächen. Osnabrück, Universität, PhD thesis, 2009
- [72] L. TRÖGER, J. SCHÜTTE, F. OSTENDORF, A. KÜHNLE, M. REICHLING: Concept for support and cleavage of brittle crystals.
Rev. Sci. Instrum. **80**, 063703 (2009)
- [73] SCIFINDER: Chemical Abstract Service: Calculated using ACD/Labs software V11.02 (© 1994-2014 ACD/Labs). Columbus OH,
- [74] D. NEČAS, P. KLAPETEK: Gwyddion: an open-source software for SPM data analysis.
Cent. Eur. J. Phys. **10**, 181 (2012)
- [75] P. RAHE, R. BECHSTEIN, A. KÜHNLE: Vertical and lateral drift corrections of scanning probe microscopy images.
J. Vac. Sci. Technol., B **28**, C4E31 (2010)
- [76] J. D. HALLEY, D. A. WINKLER: Consistent concepts of self-organization and self-assembly.
Complexity **14**, 10 (2008)
- [77] A. KÜHNLE: Self-assembly of organic molecules at metal surfaces.
Curr. Opin. Colloid In. **14**, 157 (2009)
- [78] J. V. BARTH, G. COSTANTINI, K. KERN: Engineering atomic and molecular nanostructures at surfaces.
Nature **437**, 671 (2005)
- [79] T. KUNSTMANN, A. SCHLARB, M. FENDRICH, T. WAGNER, R. MÖLLER, R. HOFFMANN: Dynamic force microscopy study of 3,4,9,10-perylenetetracarboxylic dianhy-

- dride on KBr(001).
Phys. Rev. B **71**, 121403(R) (2005)
- [80] S. A. BURKE, J. M. TOPPLE, P. GRÜTTER: Molecular dewetting on insulators.
J. Phys.: Condens. Matter **21**, 423101 (2009)
- [81] A. AMASSIAN, V. A. POZDIN, T. V. DESAI, S. HONG, A. R. WOLL, J. D. FERGUSON, J. D. BROCK, G. G. MALLIARAS, J. R. ENGSTROM: Post-deposition reorganization of pentacene films deposited on low-energy surfaces.
J. Mater. Chem. **19**, 5580 (2009)
- [82] D. KÄFER, C. WÖLL, G. WITTE: Thermally activated dewetting of organic thin films: the case of pentacene on SiO₂ and gold.
Appl. Phys. A **95**, 273 (2009)
- [83] C. D. DIMITRAKOPOULOS, P. R. L. MALENFANT: Organic Thin Film Transistors for Large Area Electronics.
Adv. Mater. **14**, 99 (2002)
- [84] J. L. NEFF, P. MILDE, C. PĂLREZ LEĂȘN, M. D. KUNDRAT, L. M. ENG, C. R. JACOB, R. HOFFMANN-VOGEL: Epitaxial Growth of Pentacene on Alkali Halide Surfaces Studied by Kelvin Probe Force Microscopy.
ACS Nano **8**, 3294 (2014)
- [85] P. RAHE, R. LINDNER, M. KITTELMANN, M. NIMMICH, A. KUHNLE: From dewetting to wetting molecular layers: C₆₀ on CaCO₃(10-14) as a case study.
Phys. Chem. Chem. Phys. **14**, 6544 (2012)
- [86] O. PAKARINEN, J. MATIVETSKY, A. GULANS, M. PUSKA, A. FOSTER, P. GRUTTER: Role of van der Waals forces in the adsorption and diffusion of organic molecules on an insulating surface.
Phys. Rev. B **80**, 085401 (2009)
- [87] S. MAIER, L.-A. FENDT, L. ZIMMERLI, T. GLATZEL, O. PFEIFFER, F. DIEDERICH, E. MEYER: Nanoscale En-

- gineering of Molecular Porphyrin Wires on Insulating Surfaces.
Small **4**, 1115 (2008)
- [88] L. NONY, F. BOCQUET, F. PARA, F. CHÉRIOUX, E. DUVERGER, F. PALMINO, V. LUZET, C. LOPPACHER: Dipole-driven self-organization of zwitterionic molecules on alkali halide surfaces.
Beilstein J. Nanotechnol. **3**, 285 (2012)
- [89] M. FENDRICH, M. LANGE, C. WEISS, T. KUNSTMANN, R. MÖLLER: N,N'-dimethylperylene-3,4,9,10-bis(dicarboximide) on alkali halide (001) surfaces.
J. Appl. Phys. **105**, 094311 (2009)
- [90] A. HINAUT, K. LEKHAL, G. AIVAZIAN, S. BATAILLÉ, A. GOURDON, D. MARTROU, S. GAUTHIER: NC-AFM Study of the Adsorption of Hexamethoxytriphenylene on KBr(001).
J. Phys. Chem. C **115**, 13338 (2011)
- [91] M. KITTELMANN, P. RAHE, M. NIMMRICH, C. M. HAUKE, A. GOURDON, A. KÜHNLE: On-Surface Covalent Linking of Organic Building Blocks on a Bulk Insulator.
ACS Nano **5**, 8420 (2011)
- [92] M. KITTELMANN, M. NIMMRICH, J. L. NEFF, P. RAHE, W. GREŃ, X. BOJU, A. GOURDON, A. KÜHNLE: Controlled Activation of Substrate Templating in Molecular Self-Assembly by Deprotonation.
J. Phys. Chem. C **117**, 23868 (2013)
- [93] C. M. HAUKE, R. BECHSTEIN, M. KITTELMANN, C. STORZ, A. F. M. KILBINGER, P. RAHE, A. KÜHNLE: Controlling Molecular Self-Assembly on an Insulating Surface by Rationally Designing an Efficient Anchor Functionality That Maintains Structural Flexibility.
ACS Nano **7**, 5491 (2013)
- [94] S. GRONERT: Theoretical studies of proton transfers. 1. The potential energy surfaces of the identity reactions of

- the first- and second-row non-metal hydrides with their conjugate bases.
J. Am. Chem. Soc. **115**, 10258 (1993)
- [95] DEL BENE, J. E., M. J. FRISCH, J. A. POPLE: Molecular orbital study of the complexes $(\text{AHn})_2\text{H}^+$ formed from ammonia, water, hydrogen fluoride, phosphine, hydrogen sulfide, and hydrogen chloride.
J. Phys. Chem. **89**, 3669 (1985)
- [96] T. NEUHEUSER, B. A. HESS, C. REUTEL, E. WEBER: Ab Initio Calculations of Supramolecular Recognition Modes. Cyclic versus Noncyclic Hydrogen Bonding in the Formic Acid/Formamide System.
J. Phys. Chem. **98**, 6459 (1994)
- [97] S. TSUZUKI, K. HONDA, T. UCHIMARU, M. MIKAMI, K. TANABE: Origin of the Attraction and Directionality of the NH/π Interaction: Comparison with OH/π and CH/π Interactions.
J. Am. Chem. Soc. **122**, 11450 (2000)
- [98] J. J. NOVOA, F. MOTA: The $\text{C}-\text{H}\cdots\pi$ bonds: strength, identification, and hydrogen-bonded nature: a theoretical study.
Chem. Phys. Lett. **318**, 345 (2000)
- [99] T. STEINER: The Hydrogen Bond in the Solid State.
Angew. Chem. Int. Ed. **41**, 48 (2002)
- [100] E. ARUNAN, G. R. DESIRAJU, R. A. KLEIN, J. SADLEJ, S. SCHEINER, I. ALKORTA, D. C. CLARY, R. H. CRABTREE, J. J. DANNENBERG, P. HOBZA, H. G. KJAERGAARD, A. C. LEGON, B. MENNUCCI, D. J. NESBITT: Definition of the hydrogen bond (IUPAC Recommendations 2011).
Pure Appl. Chem. **83**, 1637 (2011)
- [101] E. ARUNAN, G. R. DESIRAJU, R. A. KLEIN, J. SADLEJ, S. SCHEINER, I. ALKORTA, D. C. CLARY, R. H. CRABTREE, J. J. DANNENBERG, P. HOBZA, H. G. KJAER-

- GAARD, A. C. LEGON, B. MENNUCCI, D. J. NESBITT: Defining the hydrogen bond: An account (IUPAC Technical Report).
Pure Appl. Chem. **83**, 1619 (2011)
- [102] G. R. DESIRAJU: A Bond by Any Other Name.
Angew. Chem. Int. Ed. **50**, 52 (2011)
- [103] J. KROON, J. A. KANTERS, VAN DUIJNEVELDT-VAN DE RIJDT, J.G.C.M., F. B. VAN DUIJNEVELDT, J. A. Vliegenthart: O-H·O Hydrogen bonds in molecular crystals a statistical and quantum-chemical analysis.
J. Mol. Struct. **24**, 109 (1975)
- [104] T. STEINER, R. DESIRAJU, GAUTAM: Distinction between the weak hydrogen bond and the van der Waals interaction.
Chem. Commun. **8**, 891 (1998)
- [105] D. M. DUFFY, J. H. HARDING: Modelling the interfaces between calcite crystals and Langmuir monolayers.
J. Mater. Chem. **12**, 3419 (2002)
- [106] M. WATKINS, T. TREVETHAN, M. L. SUSHKO, A. L. SHLUGER: Designing Molecular Architecture to Control Diffusion and Adsorption on Insulating Surfaces.
J. Phys. Chem. C **112**, 4226 (2008)
- [107] M. KITTELMANN, P. RAHE, A. KÜHNLE: Molecular self-assembly on an insulating surface: interplay between substrate templating and intermolecular interactions.
J. Phys.: Condens. Matter **24**, 354007 (2012)
- [108] REEDER, R. J. (Hrsg.): *Reviews in mineralogy*. Bd. 11: *Carbonates: Mineralogy and chemistry*. Washington, D.C : Mineralogical Society of America, 1983
- [109] W. A. DEER, R. A. HOWIE, J. ZUSSMAN: An introduction to the rock forming minerals. 2. ed. Harlow : Longman Scientific & Technical, 1992

- [110] P. A. RAHE: The calcite(10-14) surface: a versatile substrate for molecular self-assembly. Mainz, Johannes Gutenberg-Universität, PhD thesis, 2011
- [111] D. R. BAER, D. L. BLANCHARD: Studies of the calcite cleavage surface for comparison with calculation. *Appl. Surf. Sci.* **72**, 295 (1993)
- [112] L. ADDADI, S. WEINER: Kontroll- und Designprinzipien bei der Biomineralisation. *Angew. Chem.* **104**, 159 (1992)
- [113] H. CÖLFEN: Biomineralization: A crystal-clear view. *Nat. Mater.* **9**, 960 (2010)
- [114] C. A. ORME, A. NOY, A. WIERZBICKI, MCBRIDE, M. T., M. GRANTHAM, H. H. TENG, P. M. DOVE, J. J. DEY-OREO: Formation of chiral morphologies through selective binding of amino acids to calcite surface steps. *Nature* **411**, 775 (2001)
- [115] S. KERISIT, S. C. PARKER, J. H. HARDING: Atomistic Simulation of the Dissociative Adsorption of Water on Calcite Surfaces. *J. Phys. Chem. B* **107**, 7676 (2003)
- [116] R. KRISTENSEN, STIPP, S. L. S., K. REFSON: Modeling steps and kinks on the surface of calcite. *J. Chem. Phys.* **121**, 8511 (2004)
- [117] S. L. STIPP, M. F. HOCELLA: Structure and bonding environments at the calcite surface as observed with X-ray photoelectron spectroscopy (XPS) and low energy electron diffraction (LEED). *Geochim. Cosmochim. Ac.* **55**, 1723 (1991)
- [118] S. STIPP, C. M. EGGLESTON, B. S. NIELSEN: Calcite surface structure observed at microtopographic and molecular scales with atomic force microscopy (AFM). *Geochim. Cosmochim. Ac.* **58**, 3023 (1994)

- [119] J. SCHÜTTE, P. RAHE, L. TRÖGER, S. RODE, R. BECHSTEIN, M. REICHLING, A. KÜHNLE: Clear Signature of the (2×1) Reconstruction of Calcite (10-14). *Langmuir* **26**, 8295 (2010)
- [120] P. RAHE, J. SCHÜTTE, A. KÜHNLE: NC-AFM contrast formation on the calcite (10-14) surface. *J. Phys.: Condens. Matter* **24**, 084006 (2012)
- [121] A. L. RACHLIN, G. S. HENDERSON, M. C. GOH: An atomic force microscope (AFM) study of the calcite cleavage plane: Image averaging in Fourier spac. *Am. Mineral.* **77**, 904 (1992)
- [122] S. RODE, N. OYABU, K. KOBAYASHI, H. YAMADA, A. KÜHNLE: True Atomic-Resolution Imaging of (10-14) Calcite in Aqueous Solution by Frequency Modulation Atomic Force Microscopy. *Langmuir* **25**, 2850 (2009)
- [123] P. RAHE, S. KUHN, A. KÜHNLE: Is Calcite (104) a Chiral Surface? *JUnQ* **3**, 21 (2013)
- [124] L. ADDADI, S. WEINER: Biomineralization: Crystals, asymmetry and life. *Nature* **411**, 753 (2001)
- [125] J. L. NEFF, M. KITTELMANN, R. BECHSTEIN, A. KUHNLE: Decisive influence of substitution positions in molecular self-assembly. *Phys. Chem. Chem. Phys.* **16**, 15437 (2014)
- [126] LECHNER, M. D. (Hrsg.) , ANS, J. d. (Hrsg.) , LAX, E, (Hrsg.): Taschenbuch für Chemiker und Physiker. 4., Neubearb. und rev. Aufl. Berlin : Springer, 1992
- [127] L. LEISEROWITZ: Molecular Packing Modes. Carboxylic Acids. *Acta Crystallogr.* **B32**, 775 (1976)

- [128] D. TZELI, I. D. PETSALAKIS, G. THEODORAKOPOULOS, D. AJAMI, J. REBEK: Theoretical study of free and encapsulated carboxylic acid and amide dimers. *Int. J. Quantum Chem.* **113**, 734 (2013)
- [129] M. S. ADAM, M. J. GUTMANN, C. K. LEECH, D. S. MIDDLEMISS, A. PARKIN, L. H. THOMAS, C. C. WILSON: Stability and cooperativity of hydrogen bonds in dihydroxybenzoic acids. *New J. Chem.* **34**, 85 (2010)
- [130] G. GIACOMELLO, A. M. LIQUORI, A. RIPAMONTI: Isosterism and Molecular Fourier Transform: Crystal Structure Determination of 2-4-Dihydroxybenzoic Acid as related to that of 2-Hydroxy-4-aminobenzoic Acid. *Nature* **177**, 944 (1956)
- [131] L. MACGILLIVRAY, M. ZAWOROTKO: Crystal and molecular structure of 2,6-dihydroxybenzoic acid. *J. Chem. Crystallogr.* **24**, 703 (1994)
- [132] A. PARKIN, M. ADAM, R. I. COOPER, D. S. MIDDLEMISS, C. C. WILSON: Structure and hydrogen bonding in 2,4-dihydroxybenzoic acid at 90, 100, 110 and 150 K; a theoretical and single-crystal X-ray diffraction study. *Acta Crystallogr. B Struct. Sci.* **63**, 303 (2007)
- [133] B. SARMA, P. SANPHUI, A. NANGIA: Polymorphism in Isomeric Dihydroxybenzoic Acids. *Cryst. Growth Des.* **10**, 2388 (2010)
- [134] LIDE, D. R. (Hrsg.): *CRC Handbook of Chemistry and Physics*, 89th Edition (Internet Version 2009). Boca Raton FL : CRC Press/Taylor and Francis, 2009
- [135] S. LUKAS, G. WITTE, C. WÖLL: Novel Mechanism for Molecular Self-Assembly on Metal Substrates: Unidirectional Rows of Pentacene on Cu(110) Produced by a Substrate-Mediated Repulsion. *Phys. Rev. Lett.* **88**, 028301 (2001)

- [136] A. SCHIFFRIN, A. RIEMANN, W. AUWÄRTER, Y. PENNEC, A. WEBER-BARGIONI, D. CVETKO, A. COSSARO, A. MORGANTE, J. V. BARTH: Zwitterionic self-assembly of l-methionine nanogratings on the Ag(111) surface. *P. Natl. Acad. Sci. USA* **104**, 5279 (2007)
- [137] J. V. BARTH, J. WECKESSER, C. CAI, P. GÜNTER, L. BÜRGI, O. JEANDUPEUX, K. KERN: Building Supramolecular Nanostructures at Surfaces by Hydrogen Bonding. *Angew. Chem. Int. Ed.* **39**, 1230 (2000)
- [138] A. RIEMANN, B. NELSON: Molecular Wires Self-Assembled on a Graphite Surface. *Langmuir* **25**, 4522 (2009)
- [139] P. JENSEN: Growth of nanostructures by cluster deposition: Experiments and simple models. *Rev. Mod. Phys.* **71**, 1695 (1999)
- [140] M. EINAX, W. DIETERICH, P. MAASS: Colloquium: Cluster growth on surfaces: Densities, size distributions, and morphologies. *Rev. Mod. Phys.* **85**, 921 (2013)
- [141] A. YURTSEVER, Y. SUGIMOTO, M. FUKUMOTO, M. ABE, S. MORITA: Effect of tip polarity on Kelvin probe force microscopy images of thin insulator CaF₂ films on Si(111). *Appl. Phys. Lett.* **101**, 083119 (2012)
- [142] C. M. HAUKE: Systematic functionalization of molecules for molecular self-assembly. Mainz, Johannes Gutenberg-Universität, PhD thesis, 2013
- [143] F. H. ALLEN, MOTHERWELL, W. D. S., P. R. RAITHBY, G. P. SHIELDS, R. TAYLOR: Systematic analysis of the probabilities of formation of bimolecular hydrogen-bonded ring motifs in organic crystal structures. *New J. Chem.* **23**, 25 (1999)
- [144] L. K. HANSEN, G. L. PERLOVICH, A. BAUER-BRANDL:

- Redetermination of 3-hydroxybenzamide.
Acta Crystallogr. E Struct. Rep. Online **63**, 2359 (2007)
- [145] M. O. SINNOKROT, E. F. VALEEV, C. D. SHERRILL: Estimates of the Ab Initio Limit for π - π Interactions: The Benzene Dimer.
J. Am. Chem. Soc. **124**, 10887 (2002)
- [146] B. SCHULER, S.-X. LIU, Y. GENG, S. DECURTINS, G. MEYER, L. GROSS: Contrast Formation in Kelvin Probe Force Microscopy of Single π -Conjugated Molecules.
Nano Lett. **14**, 3342 (2014)
- [147] H. O. JACOBS, P. LEUCHTMANN, O. J. HOMAN, A. STEMMER: Resolution and contrast in Kelvin probe force microscopy.
J. Appl. Phys. **84**, 1168 (1998)
- [148] R. BAIER, C. LEENDERTZ, M. C. LUX-STEINER, S. SADEWASSER: Toward quantitative Kelvin probe force microscopy of nanoscale potential distributions.
Phys. Rev. B **85**, 165436 (2012)
- [149] G. COHEN, E. HALPERN, S. U. NANAYAKKARA, J. M. LUTHER, C. HELD, R. BENNEWITZ, A. BOAG, Y. ROSENWAKS: Reconstruction of surface potential from Kelvin probe force microscopy images.
Nanotechnology **24**, 295702 (2013)
- [150] L. NONY, A. FOSTER, F. BOCQUET, C. LOPPACHER: Understanding the Atomic-Scale Contrast in Kelvin Probe Force Microscopy.
Phys. Rev. Lett. **103**, 036802 (2009)
- [151] S. SADEWASSER, P. JELINEK, C.-K. FANG, O. CUSTANCE, Y. YAMADA, Y. SUGIMOTO, M. ABE, S. MORITA: New Insights on Atomic-Resolution Frequency-Modulation Kelvin-Probe Force-Microscopy Imaging of Semiconductors.
Phys. Rev. Lett. **103**, 266103 (2009)

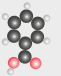
- [152] T. GLATZEL, L. ZIMMERLI, S. KAWAI, E. MEYER, L.-A. FENDT, F. DIEDERICH: Oriented growth of porphyrin-based molecular wires on ionic crystals analysed by nc-AFM.
Beilstein J. Nanotechnol. **2**, 34 (2011)
- [153] A. LABUDA, Y. MIYAHARA, L. COCKINS, P. H. GRÜTTER: Decoupling conservative and dissipative forces in frequency modulation atomic force microscopy.
Phys. Rev. B **84**, 125433 (2011)
- [154] G. TEOBALDI, K. LÄMMLE, T. TREVETHAN, M. WATKINS, A. SCHWARZ, R. WIESENDANGER, A. L. SHLUGER: Chemical Resolution at Ionic Crystal Surfaces Using Dynamic Atomic Force Microscopy with Metallic Tips.
Phys. Rev. Lett. **106**, 216102 (2011)
- [155] A. LISCIO, V. PALERMO, K. MÜLLEN, P. SAMORÌ: Tip-Sample Interactions in Kelvin Probe Force Microscopy: Quantitative Measurement of the Local Surface Potential.
J. Phys. Chem. C **112**, 17368 (2008)
- [156] A. LISCIO, V. PALERMO, D. GENTILINI, F. NOLDE, K. MÜLLEN, P. SAMORÌ: Quantitative Measurement of the Local Surface Potential of π -Conjugated Nanostructures: A Kelvin Probe Force Microscopy Study.
Adv. Funct. Mater. **16**, 1407 (2006)

Appendix A

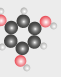
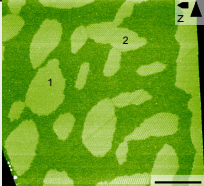
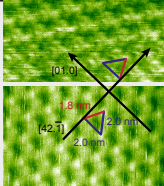
Overview of Self-Assembled Structures

A Overview of Self-Assembled Structures

Benzoic acid


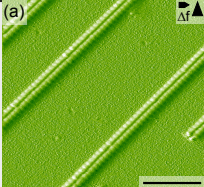
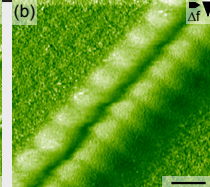
 <p>$pK_A = 4.20$</p>	 <p>20 nm</p>	<ul style="list-style-type: none"> • unordered ML
---	--	--

Hydroxybenzenes

 <p>$pK_A = 9.06$</p>	 <p>200 nm</p>		<ul style="list-style-type: none"> • islands • two patterns with quasi-hexagonal order mirrored at [-4-2.1] • islands attach to steps from left side
---	---	---	---

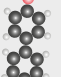
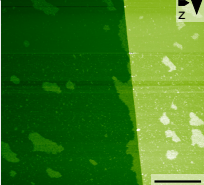
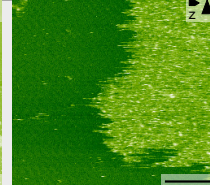
Hydroxybenzoic acids

 <p>2-HBA $pK_A = 3.01$</p>	 <p>5 nm</p>	<ul style="list-style-type: none"> • mobile below one ML • (2x1) superstructure at 1 ML • (1x1) superstructure for multilayers • KPFM: 2nd ML more positive than 1st ($\Delta V \approx 1.5V$) • 1st ML possibly deprotonated
---	---	---

 <p>3-HBA $pK_A = 4.08$</p>	 <p>(a) 10 nm</p>	 <p>(b) 1 nm</p>	<ul style="list-style-type: none"> • long, equidistantly distributed stripes • stripes composed of molecular double rows in zigzag arrangement • (4x1) superstructure at 1 ML • no strong KPFM signal
---	--	---	---


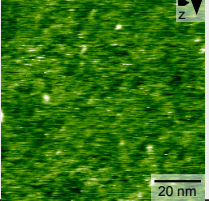

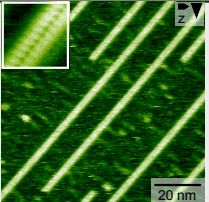

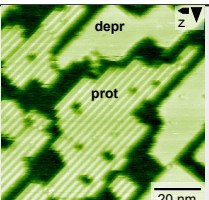

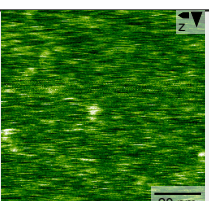
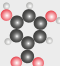
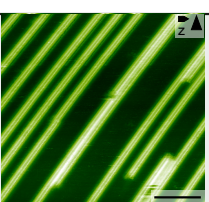
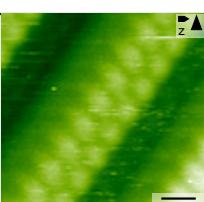
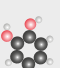
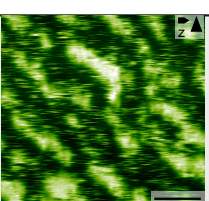
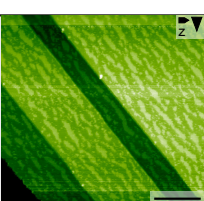
 <p>4-HBA $pK_A = 4.57$</p>	 <p>20 nm</p>	<ul style="list-style-type: none"> • submonolayer: small, diffusive islands • higher coverage: competition of several structures
---	--	--

4'-Hydroxy-4-biphenylcarboxylic acid


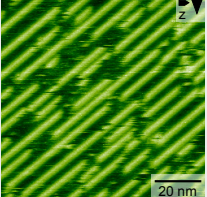
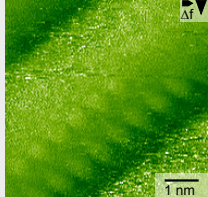
 <p>$pK_A = 4.29$</p>	 <p>200 nm</p>	 <p>20 nm</p>	<ul style="list-style-type: none"> • fuzzy islands • no internal resolution achieved • islands attach to steps from left side • positive KPFM contrast
---	---	--	--


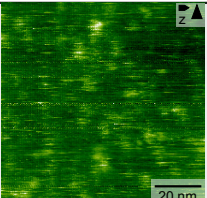
Dihydroxybenzoic acids

(published in: J. L. Neff Phys. Chem. Chem. Phys. **16**, 15437 (2014))

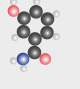
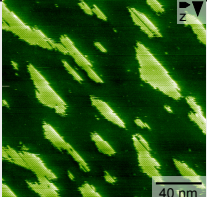
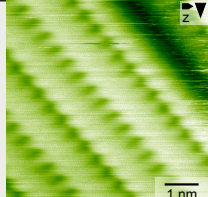
 <p>2,6-DHBA pK_A = 1.30</p>		<ul style="list-style-type: none"> • submonolayer: mobile molecules • no phase transition even upon annealing • higher coverage: competition of several structures
 <p>2,3-DHBA pK_A = 2.93</p>		<p>stable structure</p> <ul style="list-style-type: none"> • phase transition from stripes to unordered clusters occurs at RT • transition attributed to deprotonation • stripes: molecular double rows • clusters: stable but unordered
 <p>2,5-DHBA pK_A = 3.01</p>		<p>stable structure: depr</p> <p>(1x5)</p> <ul style="list-style-type: none"> • phase transition from striped phase to dense phase occurs at RT • transition attributed to deprotonation • prot islands: (6x1) superstructure • depr islands: (1x5) superstructure • negative KPFM signal • published in: M. Kittelmann et. al ACS Nano 6, 7406 (2012)
 <p>2,4-DHBA pK_A = 3.31</p>		<ul style="list-style-type: none"> • submonolayer: mobile molecules • no phase transition even upon annealing • higher coverage: competition of several structures
 <p>3,5-DHBA pK_A = 3.96</p>		 <ul style="list-style-type: none"> • long, randomly distributed stripes • stripes composed of molecular double rows in zigzag arrangement • (4x1) superstructure at one ML • no strong KPFM signal
 <p>3,4-DHBA pK_A = 4.45</p>		 <ul style="list-style-type: none"> • fuzzy islands elongated along [01.0] • no internal resolution achieved • no phase transition even upon annealing

Aminobenzoic acids

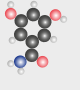
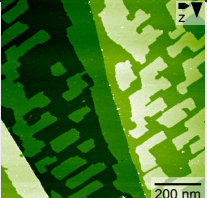
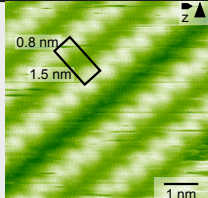
 <p>3-ABA pK_A = 4.75</p>	 <p>20 nm</p>	 <p>1 nm</p>	<ul style="list-style-type: none"> • equidistantly distributed stripes • stripes composed of double rows in commensurate zig-zag arrangement • no strong KPFM signal
---	--	---	---

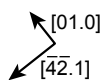
 <p>4-ABA pK_A = 4.86</p>	 <p>20 nm</p>	<ul style="list-style-type: none"> • mobile molecules and diffusive clusters at submonolayer coverage
---	--	--

Hydroxybenzamides

 <p>3-HBamide pK_A = 9.26</p>	 <p>40 nm</p>	 <p>1 nm</p>	<ul style="list-style-type: none"> • striped islands of tilted molecules • (1x3) superstructure • island edges differ • positive KPFM signal
--	---	--	--

Dihydroxybenzamides

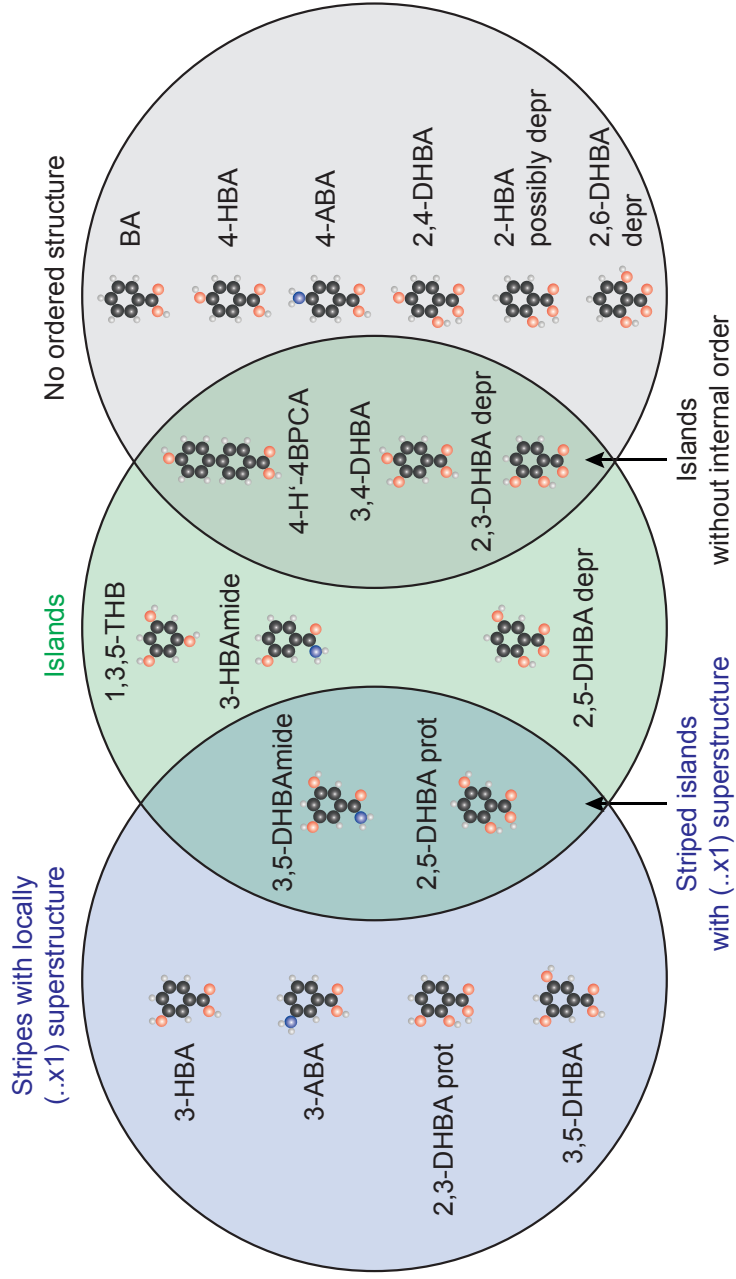
 <p>3,5-DHBAamide pK_A = 8.75</p>	 <p>200 nm</p>	 <p>0.8 nm 1.5 nm 1 nm</p>	<ul style="list-style-type: none"> • striped islands of flat-lying molecules • (3x1) superstructure • island shape but not internal structure change over time • positive KPFM signal
---	---	---	---



Directions apply to all figures.

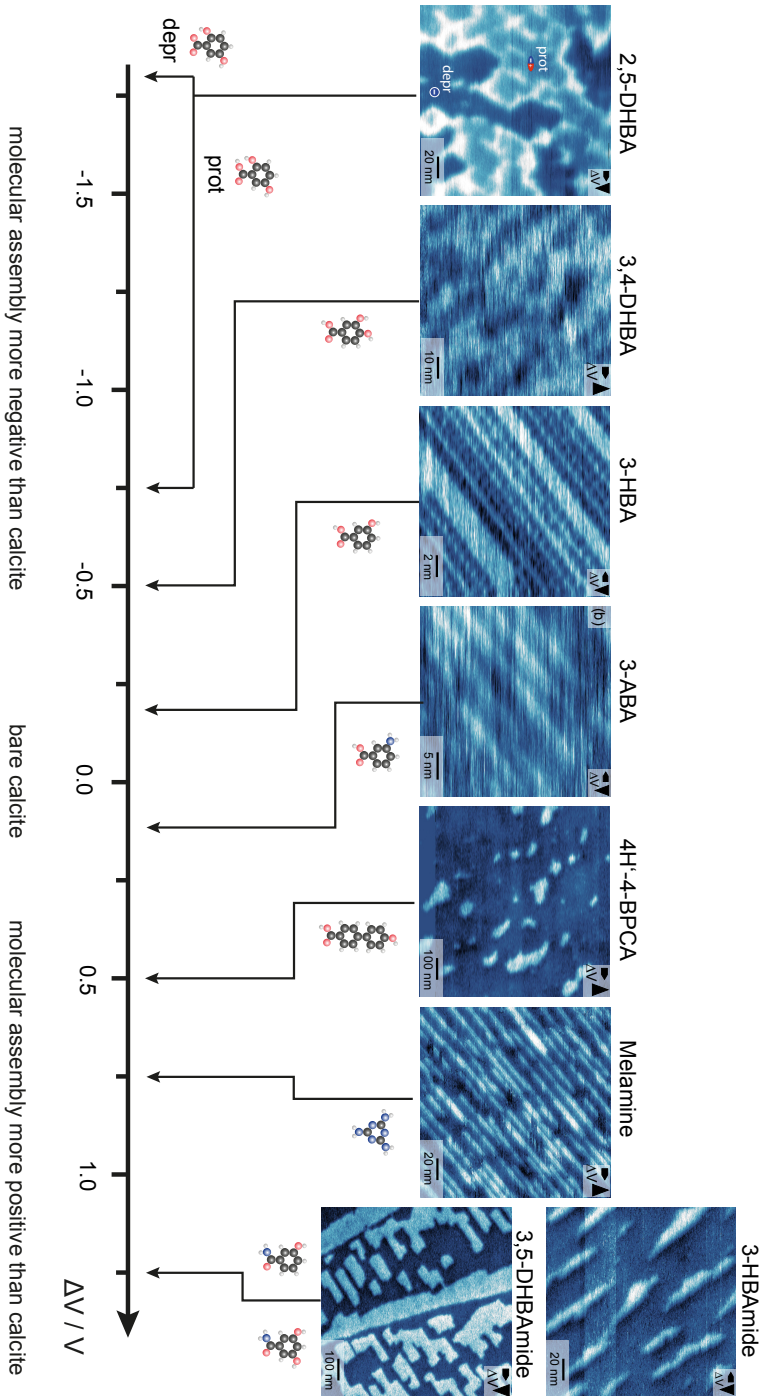
pK_A values for most acidic position as listed in Scifinder, calculated in aqueous solution using Advanced Chemistry Development (ACD/Labs) Software V11.02 (© 1994-2014 ACD/Labs).

Overview of molecular structures formed at submonolayer coverage on calcite held at room temperature



Appendix B

Trends of KPFM contrasts



Acknowledgements

Zum Schluss möchte ich mich bei all denen herzlich bedanken, deren Unterstützung diese Arbeit erst ermöglicht hat.

[Personal data removed]

Publications and Presentations

Publications in peer-reviewed journals

- **Decisive Influence of Substitution Positions in Molecular Self-Assembly**
J. L. Neff, M. Kittelmann, R. Bechstein, A. Kühnle
Phys. Chem. Chem. Phys. **16**, 15437 (2014)
- **Epitaxial Growth of Pentacene on Alkali Halide Surfaces Studied by Kelvin Probe Force Microscopy**
J. L. Neff, P. Milde, C. Pérez León, M. D. Kundrat, L. M. Eng, C. R. Jacob, R. Hoffmann-Vogel
ACS Nano **8**, 3294 (2014)
- **Controlled Activation of Substrate Templating in Molecular Self-Assembly by Deprotonation**
M. Kittelmann, M. Nimmrich, J. L. Neff, P. Rahe, W. Greñ, X. Bouju, A. Gourdon, A. Kühnle
J. Phys. Chem. C **117**, 23868 (2013)
- **Tuning Molecular Self-Assembly on Bulk Insulator Surfaces by Anchoring of the Organic Building Blocks**
P. Rahe, M. Kittelmann, J. L. Neff, M. Nimmrich, M. Reichling, P. Maass, A. Kühnle,
Adv. Mater. **25**, 3948 (2013)
- **Molecular-resolution imaging of pentacene on KCl(001)**
J. L. Neff, J. Götzen, E. Li, M. Marz, R. Hoffmann-Vogel
Beilstein J. Nanotechnol. **3**, 186 (2012)

Talks

(presenting author underlined)

- **Decisive Influence of Substitution Positions in Molecular Self-Assembly**
J. L. Neff, M. Kittelmann, W. Greń, X. Bouju, A. Gourdon, R. Bechstein, A. Kühnle
(ASXMT 2014, Karlsruhe, Germany)
- **Fine-tuning of molecular self-assembly on a bulk insulator**
J. L. Neff, M. Kittelmann, R. Bechstein, A. Kühnle
(NC-AFM 2013, Maryland, USA)
- **Direct Visualization and Controlled Activation: Substrate emplanting in Molecular Self-Assembly by Deprotonation**
M. Kittelmann, M. Nimmrich, J. L. Neff, P. Rahe, W. Greń, X. Bouju, A. Gourdon, A. Kühnle
(NC-AFM 2013, Maryland, USA)
- **Molecular Ordering and Local Work Function of Pentacene on Ionic Crystalline Surfaces**
J. L. Neff, P. Milde, J. Götzen, R. Hoffmann-Vogel
(ICN+T 2012, Paris, Germany and
DPG Spring Conference 2012, Berlin, Germany)

Poster Presentations

(presenting author underlined)

- **Dewetting of pentacene on rocksalt (001) surfaces: a KPFM study**
J. L. Neff, P. Milde, C. Pérez León, L. M. Eng, R. Hoffmann-Vogel
(AAFMT 2013, Karlsruhe, Germany)
- **NC-AFM and KPFM study of the dewetting of pentacene on rocksalt surfaces**
J. L. Neff, P. Milde, C. Pérez León, M. Marz, L. M. Eng, R. Hoffmann-Vogel
(AAFMT 2013, Karlsruhe, Germany and Trends in Nanoscience 2013, Irsee, Germany)
- **Molecular ordering and local work function of pentacene on ionic crystalline surfaces**
J. L. Neff, J. Götzen, P. Milde, R. Hoffmann-Vogel
(AAFMT 2012, Karlsruhe, Germany)
- **Epitaxial Growth of Pentacene Thin Films on KCl(001) and KBr(001)**
J. L. Neff, J. Götzen, E. Li, M. Marz, P. Milde, R. Hoffmann-Vogel
(NC-AFM 2011, Lindau, Germany and CFN Summer School Molecular Nanostructures 2011, Bad Herrenalb, Germany)